Strong light-matter coupling in microcavity-embedded semiconductor quantum wells and quantum dots

Kanchana Sivalertporn

A Thesis submitted to

Cardiff University

for the degree of

Doctor of Philosophy

July 2013

Declaration: This work has not been submitted in substance for any other degree or award at this or any other university or place of learning, nor is being submitted concurrently in candidature for any degree or other award.

Signed: $\overline{\hspace{3cm}\text{Candidate}\hspace{3cm}}$

Date: $\overline{\hspace{7cm}}$

Statement 1: This thesis is being submitted in partial fulfillment of the requirements for the degree of Doctor of Philosophy.

Signed: $\overline{\hspace{3cm}\text{Candidate}\hspace{3cm}}$

Date: $\overline{\hspace{7cm}}$

Statement 2: This thesis is the result of my own independent work/ investigation, except where otherwise stated. Other sources are acknowledged by explicit references. The views expressed are my own.

Signed: $\overline{\hspace{3cm}\text{Candidate}\hspace{3cm}}$

Date: $\overline{\hspace{7cm}}$

Statement 3: I hereby give consent for my thesis, if accepted, to be available for photocopying and for inter-library loan, and for the title and summary to be made available to outside organisations.

Signed: $\overline{\hspace{3cm}\text{Candidate}\hspace{3cm}}$

Date: $\overline{\hspace{7cm}}$

Statement 4: I hereby give consent for my thesis, if accepted, to be available for photocopying and for inter-library loans after expiry of a bar on access previously approved by the Academic Standards & Quality Committee.

Signed: $\overline{\hspace{3cm}\text{Candidate}\hspace{3cm}}$

Date: $\overline{\hspace{7cm}}$

In memory of Prof Alexei Ivanov.

Acknowledgments

Abstract

This thesis presents a theoretical investigation of exciton polaritons in strongly-coupled exciton-photon microcavity systems. Two different systems, a coupled quantum well (CQW) embedded in a planar microcavity and a quantum dot (QD) inside a micropillar cavity, are studied using suitable theoretical models. The exciton-polariton states are calculated and their optical properties are investigated in detail, showing a good agreement with experimental observations.

For a CQW structure, the excitonic states in the presence of the electric field applied in the growth direction are calculated by solving the Schrödinger equation in real space. The field dependence of exciton transition energy, binding energy, oscillator strength, lifetime and absorption are studied. The exciton ground state experiences a crossover from direct to indirect state at low electric field. A single state-basis calculation in which only the electron and hole ground states are taken into account is also made and compared with the full accurate calculation model.

The polariton effect in a microcavity-embedded CQW is investigated based on a microscopic theory. The light-matter interaction is treated by solving coupled material and Maxwell's equations. The reflectivity and absorption spectra are calculated for different detunings using the scattering matrix method. When a cavity mode is tuned to an exciton mode (zero detuning), an anticrossing of two polariton modes is observed, showing that the system is in the strong coupling regime. In addition, the fractions of direct exciton, indirect exciton and cavity mode contributed to the polariton states are calculated using the microscopic theory. The resulting polariton state with comparable contribution of all three components called dipolariton is observed.

Finally, the dynamics of the strongly-coupled exciton-cavity system in the QD-micropillar system is studied using the four wave mixing (FWM) theory applied to the Jaynes-Cummings model. Spectrally resolved and time-resolved FWM signals are calculated for different temperatures. The temperature plays the role of the parameter controlling the detuning. The beat periods of the first and second rungs of the JC ladder are also investigated, showing that the second rung has a $\sqrt{2}$ shorter period compared to the beat period of the first rung. To reveal the coherent coupling between two distant QDs, the FWM signals are Fourier-transformed into a two-dimensional frequency domain. It is found that the off-diagonal components in these 2D spectra are nonzero, demonstrating the coherent coupling between isolated QDs. In addition, the phase correction method is developed. This procedure is neccessary for a comparison with the experiment which has random phases for different detunings. A quantitative agreement between the prediction and measurement is achieved and demonstrated.

Publications

K. Sivalertporn, L. Mouchliadis, A. L. Ivanov, R. Philp and E. A. Muljarov. Direct and indirect excitons in semiconductor coupled quantum wells in an applied electric field. Phys. Rev. B **85**, 045207 (2012).

F. Albert, K. Sivalertporn, J. Kasprzak, M Strauß, C. Schneider, S. Höfling, M. Kamp, A. Forchel, S. Reitzenstein, E. A. Muljarov and W. Langbein. Coherence dynamics and quantum-to-classical crossover in an exciton-cavity system in the quantum strong coupling regime. New J. Phys. **15**, 045013 (2013).

F. Albert, K. Sivalertporn, J. Kasprzak, M Strauß, C. Schneider, S. Höfling, M. Kamp, A. Forchel, S. Reitzenstein, E. A. Muljarov and W. Langbein. Microcavity controlled coupling of excitonic qubits. Nat. Commun. **4**, 1 (2013).

K. Sivalertporn and E. A. Muljarov. Strong and weak light-matter coupling in microcavity-embedded double quantum wells. ArXiv: 1305.5883

K. Sivalertporn and E. A. Muljarov. Direct and indirect excitons and polaritons in coupled quantum well microcavities. AIP Conf. Proc. (in press).

E. A. Muljarov, K. Sivalertporn, F. Albert, J. Kasprzak, M. Strauß, C. Schneider, S. Höfling, M. Kamp, A. Forchel, S. Reitzenstein, and W. Langbein. Microcavitycontrolled coherent coupling of quantum dots. Proceedings of 20th International Symposium "Nanostructures: Physics and Technology", Nizhny Novgorod, Russia (June 2012), p.63.

E. A. Muljarov and K. Sivalertporn. Indirect and direct excitons and microcavity polaritons in AlGaAs and InGaAs coupled quantum wells. Proceedings of 20th International Symposium "Nanostructures: Physics and Technology", Nizhny Novgorod, Russia (June 2012), p.181.

Presentations

K. Sivalertporn, E. A. Muljarov and A. L. Ivanov. Direct and indirect excitons in GaAs/AlGaAs coupled quantum wells. *11th International Conference on Physics of Light-Matter Coupling in Nanostructures (PLMCN11)*, Germany (April 2011).

K. Sivalertporn, A. L. Ivanov and E. A. Muljarov. Optical properties of excitons in GaAs/AlGaAs coupled quantum wells in electric field. *International Conference on Cold Atoms, Semiconductor Polaritons and Nanoscience (POLATOM)*, Greece (May 2011).

E. A. Muljarovn, K. Sivalertporn, J. Kasprzak and W. Langbein. Four-wave mixing coherent dynamics of a strongly coupled quantum dot-microcavity system. *International Conference on Cold Atoms, Semiconductor Polaritons and Nanoscience (POLATOM)*, Greece (May 2011).

K. Sivalertporn, E. A. Muljarov, J. Kasprzak and W. Langbein. Theory of the nonlinear optical response of a strongly coupled quantum dot-microcavity system. *12th International Conference on Optics of Excitons in Confined Systems (OECS12)*, France (September 2011).

F. Albert, K. Sivalertporn, J. Kasprzak, M. Strauß, C. Schneider, S. Höfling, M. Kamp, A. Forchel, S. Reitzenstein, E. A. Muljarov, and W. Langbein. Coherent coupling of quantum dots in a micropillar cavity. *DPG Spring Meeting 2012*, Germany (2012).

F. Albert, K. Sivalertporn, *J. Kasprzak*, M. Strauß, C. Schneider, S. Höfling, M. Kamp, A. Forchel, S. Reitzenstein, E. A. Muljarov, and W. Langbein. Cavity-photon controlled coherent coupling of quantum dots. *7th International Conference on Quantum Dots (QD2012)*, USA (May 2012).

E. A. Muljarov, K. Sivalertporn, F. Albert, J. Kasprzak, M. Strauß, C. Schneider, S. Höfling, M. Kamp, A. Forchel, S. Reitzenstein, and W. Langbein. Microcavity-controlled coherent coupling of quantum dots. *20th International Symposium Nanostructures: Physics and Technology.*, Russia (June 2012).

E. A. Muljarov and K. Sivalertporn. Indirect and direct excitons and microcavity polaritons in AlGaAs and InGaAs coupled quantum wells. *20th International Symposium Nanostructures: Physics and Technology.* Russia (June 2012).

K. Sivalertporn and E. A. Muljarov. Direct and indirect excitons and polaritons in coupled quantum well microcavities. *31st International Conference on the Physcis of Semiconductors (ICPS31)*, Switzerland (July 2012).

F. Albert, K. Sivalertporn, J. Kasprzak, M. Strauß, C. Schneider, S. Höfling, M. Kamp, A. Forchel, S. Reitzenstein, E. A. Muljarov, and *W. Langbein*. Cavity-photon

controlled coherent coupling of quantum dots. *Photon 12* United Kingdom (September 2012).

E. A. Muljarov, K. Sivalertporn, F. Albert, J. Kasprzak, M. Strauß, C. Schneider, S. Höfling, M. Kamp, A. Forchel, S. Reitzenstein, and *W. Langbein*. Coherent coupling of remote excitons i microcavity-embedded quantum dots. *14th International Conference on Physics of Light-Matter Coupling in Nanostructures (PLMCN 14)* Greece (May 2013).

Contents

List of Figures

3

4

6

7

Chapter 1

Introduction

An exciton is a combined state of electron in the conduction band and hole in the valence band bound via the Coulomb interaction. Excitons in bulk semiconductors can move freely in all directions, while excitons in nanostructures are confined in one direction (quantum well), two directions (quantum wire) or three directions (quantum dot), due to the discontinuity of the band structure. Excitons in a quantum well (QW) are an attractive system for investigation due to their potential applications in electro-optic and optoelectronic devices. Their electronic and optical properties have been studied both experimentally and theoretically in the past decade. In particular, an indirect exciton - a bound state of the electron and hole residing in different QW layers - exists in couple quantum well (CQW) structures in the presence of the electric field perpendicular to the QW layer. A large spatial separation between electron and hole gives rise to a long radiative lifetime of the indirect exciton [1–5].

When a confined structure is embedded into a microcavity, the coupling between an exciton in the confined structure and the electromagnetic field in a cavity leads to a formation of a quasiparticle called a microcavity polariton. This research field is known as cavity quantum electrodynamics (cQED). A photon in a cavity is absorbed by an exciton and the exciton then re-emits a photon into a cavity. The energy exchange between exciton and photon takes place until the photon leaks out from the cavity or the exciton decays through other nonradiative channels. Theoretically, the resulting polariton eigenenergies and eigenstates are obtained by diagonalizing

the Hamiltonian. The eigenenergies are different from those of the bare exciton and photon modes and are split into upper and lower polariton branches. In the strong coupling regime, the anticrossing between the resulting polariton states is observed at the resonance. This energy splitting is called the vacuum Rabi splitting. The strong coupling phenomenon was initially predicted in bulk semiconductors by J. Hopfield [6–8] and is also observed later in atomic systems by Y. Kaluzny [9]. The progress in fabrication and theoretical study of microcavity polaritons is extremely rapid since that first observation [10–14]. The first evidence of the strong coupling in a semiconductor microcavity was reported by C. Weisbuch et al [15].

The strong coupling regime is also achieved in QD-microcavity systems. These structures have been widely investigated because of their potential applications in quantum information devices such as a quantum computer in which quantum bits (qubits) with the quantum states ($|0\rangle$ or $|1\rangle$) can be used to store the information. Experiments were performed in QED circuits in which microwave photons are coupled to the superconducting qubits [16, 17]. To achieve the strong coupling in QD microcavities, a cavity with high quality factor (Q-factor) and small photon mode volume is required [18–21]. There are many designs used in experiments in order to study the light-matter strong-coupling such as semiconductor micropillars [22, 23], microdisks [18] or photonic crystals [19, 20]. Different structures are suitable for different applications.

This thesis presents a theoretical investigation of exciton polaritons in semiconductor microcavities. We concentrate on two different structures: a CQW embedded in planar microcavity and QD-micropillar system. For the CQW-microcavity system, the excitonic states and their optical properties are calculated by solving the Schrödinger equation for an exciton. The polariton effect is included within the framework of the microscopic theory. The reflectivity and absorption spectra of polariton states are studied using the scattering matrix method. The contributions of exciton and photon components to the polariton states are also investigated. In addition, the calculated result is compared to the experimental observation. In the case of QD-microcavity system, the exciton-photon interaction is studied applying the four wave mixing (FWM) theory to the Jaynes-Cummings (JC) and Tavis-Cummings (TC)

models. The spectrally and time-resolved FWM signals are calculated for different temperatures. In addition, the two-dimensional (2D) frequency domain representation is considered in order to study the coherent coupling of isolated QDs. The phase correction is developed in order to compare the prediction with the experiment.

1.1 OVERVIEW

In the first chapter, the background information for the work presented in the remainder of the thesis is provided. A brief discussion about an exciton in bulk semiconductors and nanostructures is presented. The exciton-photon interaction in semiconductor microcavities is introduced.

Chapter two entitled "Quantum well excitons" is a theoretical study of excitonic states in CQW structures in the presence of an electric field. The optical properties of excitons are calculated as function of the electric field, demonstrating the direct-indirect transition of the exciton ground state. The calculated results show a quantitative agreement with the PL measurement [24].

Chapter three entitled "Quantum well polaritons" presents the calculation of polariton states in the same CQWs now embedded in a semiconductor microcavity. The exciton-photon interaction is treated by solving coupled material and Maxwell's equations. The complex dielectric constant, reflectivity and absorption spectra are calculated for different incident angles of light. The exciton and photon contribution to the polariton is also studied.

Chapter four entitled "Polariton in a quantum dot-microcavity system" is devoted to the interaction of a QD exciton with a photon in a micropillar cavity. The dynamics is described by using the JC model for a single-QD system and Tavis-Cummings model for a multiple-QD system. The optical nonlinearities are investigated in such systems. The basic concept of the FWM theory used is also explained. The coherent coupling of isolated QDs is demonstrated using the two-dimensional Fourier transforming. Theoretical results are compared to the experimental data by performing the phase correction to the two-dimensional FWM signal. The main conclusions and future prospects are outlined in Chapter five.
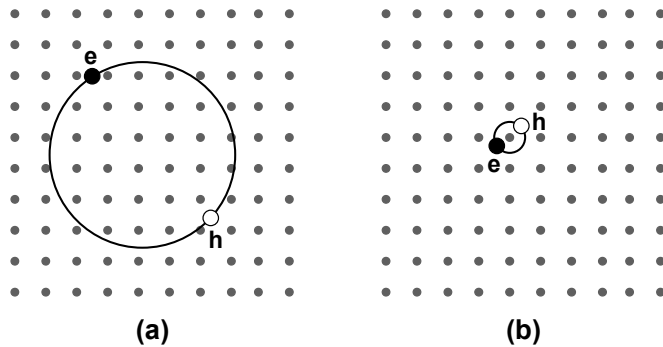
Figure 1.1: Schematic diagram of (a) Wannier-Mott and (b) Frenkel excitons.

1.2 EXCITONS IN BULK SEMICONDUCTORS

In a semiconductor, an absorbed photon can promote an electron from the valence band into the conduction band leaving a positively charged hole in the valence band. The electron in the conduction band and a hole in the valence band are then bound together due to the Coulomb interaction. This bound e-h pair is called an exciton. An exciton is electrically neutral and unstable, as electron and hole can eventually recombine. There are two different types of exciton: (i) Wannier-Mott and (ii) Frenkel excitons as shown in Fig. 1.1. The Wannier-Mott excitons are weakly bound and usually observed in semiconductors. The attraction between electrons and holes is weak, so that the e-h separation is much larger than the inter atomic spacing. By contrast, the Frenkel excitons have a much smaller radius in comparison with the size of the unit cell. The e-h pair is tightly bound and it is associated with a few atoms. The Frenkel excitons are typically found in molecular crystals.

In this study, we consider Wannier-Mott excitons in semiconductor structures only. Therefore, it is sufficient to treat the electron and hole in the effective mass approximation. The Hamiltonian for the e-h pair is then given by

$$\hat{H} = -\frac{\hbar^2 \nabla_e^2}{2m_e} - \frac{\hbar^2 \nabla_h^2}{2m_h} - \frac{e^2}{\epsilon_b \left| \mathbf{r}_e - \mathbf{r}_h \right|} + E_g \,, \tag{1.1}$$

where $\hbar$ is the reduced Plank constant, e is the electric charge, $m_{e(h)}$ is the electron (hole) effective mass, $\mathbf{r}_{e(h)}$ is the spatial coordinate for electron (hole), ϵ_b is the dielectric constant of the material and E_g is the band gap of the material. The first two

14

terms represent the kinetic energy of electron and hole respectively, while the third term is the Coulomb attraction between electron and hole. To simplify Eq.(1.1), we make a coordinate transformation, going to the centre of mass coordinate,

$$\mathbf{R} = \frac{m_e \mathbf{r}_e + m_h \mathbf{r}_h}{m_e + m_h}\,, \tag{1.2}$$

and the relative coordinate,

$$\mathbf{r} = \mathbf{r}_e - \mathbf{r}_h\,. \tag{1.3}$$

The Hamiltonian in Eq.(1.1) can then be rewritten as

$$\hat{H} = -\frac{\hbar^2 \nabla_R^2}{2M_X} - \frac{\hbar^2 \nabla_r^2}{2\mu} - \frac{e^2}{\epsilon_b r} + E_g\,, \tag{1.4}$$

where $M_X = m_e + m_h$ is the total mass, $\mu = \left(\frac{1}{m_e} + \frac{1}{m_h}\right)^{-1}$ is the reduced mass and $r = |\mathbf{r}|$. Due to the form of Eq. (1.4), we can separate the variables as: (i) the free motion of the centre of mass and (ii) the relative motion. As a result, the exciton wave function is factorised as

$$\Theta(\mathbf{r}, \mathbf{R}) = e^{i\mathbf{K} \cdot \mathbf{R}} \Psi(\mathbf{r})\,, \tag{1.5}$$

where $\Psi(\mathbf{r})$ is a hydrogen-like wave function and $\mathbf{K}$ is the exciton wave vector of the center of mass motion.

1.3 EXCITONS IN NANOSTRUCTURES

1.3.1 QUANTUM WELLS

A single quantum well (SQW) semiconductor structure typically consists of a thin semiconductor layer sandwiched between much thicker layers of a wider energy gap semiconductor. The band diagram is demonstrated in Fig. 1.2. Due to the discontinuity of the conduction and valence bands, the electrons and holes are confined in the QW layer. The thickness of the QW layer must be comparable to or smaller than the exciton Bohr radius, in order to observe the quantum confinement effects.
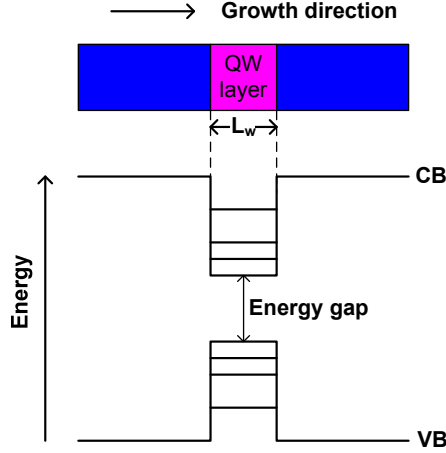
Figure 1.2: Energy band diagram of a single quantum well structure consisting of a QW layer surrounded by two thick barriers.

This is called a one-dimensional (1D) confinement because the electron and hole are confined in one direction (growth direction: z axis) and free to move in two other directions (x-y plane). As a result, only the in-plane wavevector $\mathbf{k}_{||}$ is conserved due to the breaking of translational symmetry along z direction and the electron and hole energies are quantized along the growth direction. These discrete energy levels also shown in Fig. 1.2 give rise to continuous bands due to the electron and hole motion in the x-y plane, often called subbands. The exciton wave function in a SQW then takes the form

$$\Theta(\mathbf{r}_e, \mathbf{r}_h) = e^{i\mathbf{k}_{||} \cdot \mathbf{R}_{||}} \Psi(z_e, z_h, \rho) \,, \tag{1.6}$$

where ρ is the in-plane coordinate. The exciton wave function can be factorised as $\Psi(z_e, z_h, \rho) = \varphi_e(z_e)\varphi_h(z_h)\phi(\rho)$, which is an approximation in which the higher states are neglected due to a large energy separation between the levels. The z-components $\varphi_e(z_e), \varphi_h(z_h)$ are determined by solving the Schrödinger equation with a 1D square-well confining potential $V(z)$ for the electron (hole)

$$-\frac{\hbar^2}{2m_{e(h)}}\frac{d^2\varphi_{e(h)}}{dz^2} + V_{e(h)}(z) = E^{e(h)}\varphi_{e(h)}(z) \,, \tag{1.7}$$

where $m_{e(h)}$ is the electron (heavy hole) effective mass and $E^{e(h)}$ is the electron (hole) eigenenergy. The hole effective mass is an anisotropic and can be approximated using

16

Kohn-Luttinger parameters. Below is the example of the wave function in square-well potentials: infinite and finite potential wells, in the absence of electric field.

Infinite potential wells

Consider a QW in which the potential is zero inside the well and infinite elsewhere, so that there is no probability for carriers to tunnel out of the well. The wave function of the n-th state for electron or hole then has the form

$$\varphi_n(z) = \begin{cases} A\sin\left[k_n\left(z - L_w/2\right)\right] & |z| \leq L_w/2 \;\; \text{inside the wells} \\ 0 & |z| > L_w/2 \;\; \text{outside} \end{cases} \tag{1.8}$$

where $z=0$ corresponds to the center of the well. The wave function must vanish everywhere outside the well and also at the edges of well due to the continuity of the wave function and its derivative. From this boundary condition (BC) at the well edges, the wave number k_n is given by

$$k_n = \frac{n\pi}{L_w}, \tag{1.9}$$

corresponding to the energy

$$E_n = \frac{\hbar^2 k_n^2}{2m_w^*} = \frac{\hbar^2}{2m_w^*}\left(\frac{n\pi}{L_w}\right)^2, \tag{1.10}$$

where L_w is the well width, m_w^* is the electron (hole) effective mass of the well material.

Finite potential wells

In the case of a finite potential well, the potential is zero in the well but the barrier potential is finite: $V(z) = V_0$ outside the well. Therefore, there is a finite number of bound states with the energy $E < V_0$. The wave function inside the well (i.e. for $|z| \leq L_w/2$) is given by

$$\varphi_n(z) = \begin{cases} B\sin(k_n z) & n \text{ even,} \\ B\cos(k_n z) & n \text{ odd,} \end{cases} \tag{1.11}$$

with $E_n = \frac{\hbar^2 k_n^2}{2m_w^*}$. Due to a finite potential, the carriers can tunnel into the barrier with a constant exponential decay

$$\varphi_n(z) = \mathrm{C}e^{\pm \kappa_n z} \qquad |z| > L_w/2\,, \tag{1.12}$$

with $V_0 - E_n = \frac{\hbar^2 \kappa_n^2}{2m_b^*}$, where m_b^* is the effective mass in the barrier material. The eigenenergy E_n can be found from secular equation obtained from BCs.

1.3.2 COUPLED QUANTUM WELLS AND STARK EFFECT

The coupled quantum well (CQW) structure consists of two QWs separated by a barrier layer as shown in Fig. 1.3(a). For a sufficiently thin barrier, the tunneling of carriers through the barrier makes the two QWs electronically coupled to each other. As a result, an electron and a hole can either reside in one of the two QWs or their wave functions are distributed between both QWs. In the case of the Coulomb bound electron and hole residing in the same QW, they form a direct exciton. If they are located in different QWs, an indirect exciton is created. A small overlap integral of indirect exciton leads to a longer exciton lifetime compared to that in SQWs. The binding energy also reduces due to the large separation of carriers.

CQW exciton in the presence of electric field

In a symmetric CQW structure with no electric field applied, the tunneling through the middle barrier causes the splitting of the degenerate single-particle states into doublets with symmetric and antisymmetric states in each. Only the transitions between states having the same parity are optically allowed because the integral of the wave function overlap is nonzero. The Coulomb-coupled e-h pairs form the excitonic states that are optically either bright or dark. When electric field is applied in the growth direction [Fig. 1.3(b)], it breaks down the symmetry of the system making all these excitons bright. The transition from states with well-defined parity to the ones with the electron (hole) located in one of the two QWs can form combinations of direct and indirect uncorrelated e-h pair states. These different pair states are

18
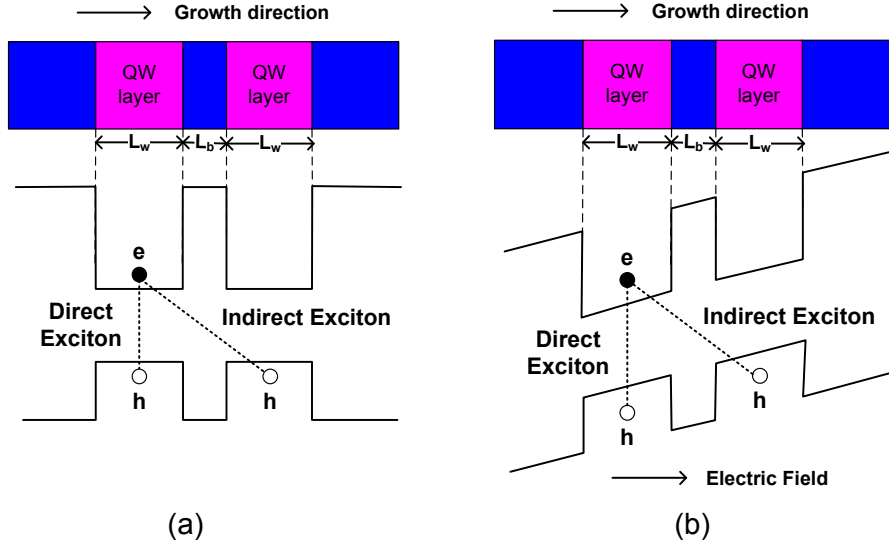
Figure 1.3: Energy band diagram of a coupled quantum well structure consisting of two QW layers separated by a thin barrier in (a) no field and (b) the presence of electric field.

Coulomb coupled with each other and form an exciton in which the direct or indirect pair can dominate.

Quantum-confined Stark effect

In the presence of an electric field in the z direction, the electron and hole in the QW layer are pushed in the opposite direction and their energies are lowered. This red shift of the energy level is called the quantum-confined Stark effect and is given by

$$\Delta E = -p_z F \,, \tag{1.13}$$

where $p_z = \mp ez$ is the electric dipole moment for electron and hole respectively and F is the electric field in the growth direction (z-axis). The shift of the exciton transition energy is determined by the sum of the electron and hole energy shifts,

$$|\Delta E_X| = |z_e - z_h| \, eF \,, \tag{1.14}$$

19

At very small electric fields, the dipole moment is proportional to the field $p_z \propto F$, giving rise to a quadratic Stark shift. However, the e-h separation is limited by the QW width. Therefore, at higher fields the e-h dipole saturates at a value of ed, where d is the width of the QW. As a result, the Stark shift increases linearly with the electric field. The Stark effect is more prominent in CQW as compared to SQW structures due to the possibility for electron and hole to confine in different QWs [25–29]. At zero electric field, the symmetric and antisymmetric states are formed in CQW structures. As the electric field increases, these coupled states move in opposite direction. The symmetric state experiences the red shift to lower energy levels, while the antisymmetric state is a blue-shifted to higher energy levels. The Stark shifts of exciton transitions associated with these two electron and two hole coupled states is the sums of individual shifts of each electron-hole pair. As a result, there are two exciton transitions having large Stark shifts and two exciton transitions with small Stark shifts. These properties of CQW structures have attracted a great deal of interest for potential applications in optoelectronics.

1.4 Quantum dot excitons

In a quantum dot (QD), the electron and hole are confined in all three dimensions. This means that the wave function can be fully localized in the QD and the energy level is purely discrete level like in atoms. Therefore, the QDs are considered as artificial atoms. The confinement energy is proportional to $1/d^2$ where d is the size of the dot. For example, the energy levels in a rectangular box dot with infinite potential wells are given by

$$E_{e(h)}(n_x, n_y, n_z) = \frac{\pi^2 \hbar^2}{2m^*_{e(h)}} \left(\frac{n_x^2}{d_x^2} + \frac{n_y^2}{d_y^2} + \frac{n_z^2}{d_z^2} \right), \qquad (1.15)$$

where n_x, n_y, n_z denote the quantized levels in each direction. The e-h pair or exciton in a QD can be treated as a boson or fermion, depending on the size of the dot. If the QD has a radius smaller than the exciton Bohr radius, the exciton is treated as a fermion satisfying the Pauli exclusion principle and is said to be in the strong
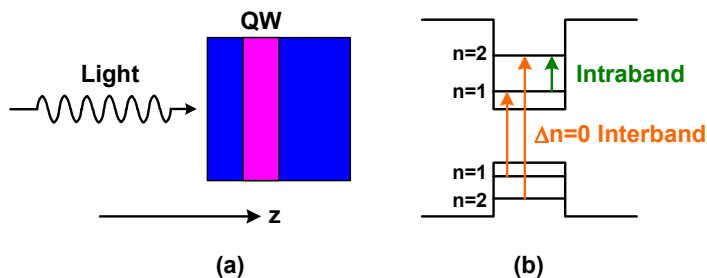
Figure 1.4: Schematic of QW absorption (a) a light of angular frequency propagating in the z direction irradiates on a QW structure and (b) the band diagram of SQW showing the interband (orange) and intraband (green) transitions.

confinement regime. If the size of the QD is larger than the exciton Bohr radius, the exciton can be treated as a boson. In this case, the exciton is in the weak confinement regime. In this work, we consider only the fermionic case and the light-matter coupling is modeled by a JC Hamiltonian model.

1.5 Light absorption

We consider a QW irradiated by light of angular frequency ω propagating in the z direction Fig.1.4(a). An electron in the valence band with an initial energy E_i is excited to a final state of energy E_f in the conduction band by absorbing of a photon and leaving a hole in the valence band. According to the Pauli exclusion principle, the final state must be empty. This transition between the valence and conduction subbands is called the interband transition as shown in Fig.1.4(b). The transition rate is given by Fermi's golden rule

$$W_{i \to f} = \frac{2\pi}{\hbar} \left| \mathbf{M} \right|^2 g(\hbar\omega) \tag{1.16}$$

$$= \frac{2\pi}{\hbar} \left| \langle f | - e\mathbf{r} \cdot \mathbf{E} | i \rangle \right|^2 g(\hbar\omega) \tag{1.17}$$

where $\mathbf{M}$ is the matrix element of the electron-photon coupling, $\mathbf{r}$ is the position vector of the electron, $\mathbf{E}$ is the electric field amplitude of the light wave and $g(\hbar\omega)$ is the electron density of states in the conduction band.

Selection rule

The light is incident on a QW structure in the z direction, so that the polarization of light is in the x-y plane. The matrix element has the form

$$M = |\mathbf{M}| = \langle f\,|x|\,i \rangle = \int \Psi_f^*(\mathbf{r}) x \Psi_i(\mathbf{r}) d\mathbf{r}\,, \qquad (1.18)$$

We consider the interband transition from the n-th hole state to the n'-th electron state. The initial and final wave functions are described by the Bloch function [30].

$$\Psi_i \equiv |i\rangle = \frac{1}{\sqrt{A}} u_v(\mathbf{r}) \varphi_{hn}(z) e^{i\mathbf{k}_{xy}\cdot\mathbf{r}_{xy}} \qquad (1.19)$$

$$\Psi_f \equiv |f\rangle = \frac{1}{\sqrt{A}} u_c(\mathbf{r}) \varphi_{en'}(z) e^{i\mathbf{k}'_{xy}\cdot\mathbf{r}_{xy}}\,. \qquad (1.20)$$

Here, $\mathbf{r}_{xy}$ is the coordinate in $x-y$ plane. The condition $\mathbf{k}_{xy} = \mathbf{k}'_{xy}$ is required due to the conservation of momentum. Substituting Eq.(1.19) and Eq.(1.20) into Eq.(1.18), the matrix element is written as

$$M = d_{cv} M_{nn'}\,, \qquad (1.21)$$

with

$$d_{cv} = \langle u_c\,|x|\,u_v \rangle = \int u_c^*(\mathbf{r}) x u_v(\mathbf{r}) d^3 r \qquad (1.22)$$

$$M_{nn'} = \langle e, n'|h, n \rangle = \int \varphi_{en'}^*(z) \varphi_{hn}(z) dz\,, \qquad (1.23)$$

where d_{cv} is the valence-conduction band dipole moment and $M_{nn'}$ is the e-h overlap integral. In the case of an infinite QW, the overlap is given by

$$M_{nn'} = \frac{2}{L_w} \int_{-L_w/2}^{L_w/2} \sin\left(k_n z + \frac{n\pi}{2}\right) \sin\left(k'_n z + \frac{n'\pi}{2}\right) dz\,, \qquad (1.24)$$

The integral is unity if $n = n'$ and zero otherwise, giving rise to the selection rule $\Delta n = 0$ for the infinite QW. This means that the transition is allowed only if electron and hole states have the same parity. This condition is only approximately true

for a finite QW since the different effective masses and potential profiles of electon and hole gives rise to the different penetration into the barrier and non-orthogonal wave functions. However, the e-h overlap for $\Delta n \neq 0$ transitions is still close to zero and the transition is forbidden if Δn is an odd number because of the opposite parity. Transitions of the electron (hole) between different subbands in the conduction (valence) band, called intraband transitions (or intersubband transitions) are also shown in Fig.1.4(b).

1.6 MICROCAVITY POLARITONS: WEAK AND STRONG COUPLING REGIMES

A typical semiconductor microcavity consists of a cavity layer sandwiched between two distributed Bragg reflectors (DBRs) as shown in Fig. 1.5(a). A DBR is usually made of alternating $\lambda/4$ layers of different semiconductor materials, with high and low refractive indices. The incident light is reflected at the DBR interface and only a single wavelength, namely that as a cavity mode, is transmitted (indicated as a sharp peak in the reflectivity spectra). This creates also a stop-band in the transmission spectrum. Hence, the DBR behaves as a high reflective mirror for wavelengths within the stop-band. When the quantum confined structure is embedded in the cavity, an exciton in such a structure can interact with a photon inside the cavity and forms an exciton-photon quasiparticle called a polariton. An exciton mode coupled to one photon gives rise to two polariton modes (double peaks are seen in the reflectivity spectra). The lower energy mode is called lower polariton (LP) branch, while the upper polariton (UP) branch refers to the mode with higher energy. In the strong coupling regime, the photon is bounced back and forth between the two DBR mirrors and is absorbed by an exciton. The excited exciton then emits a photon into the cavity by the radiative emission. The whole sequence of absorption and emission takes place until the photon leaks out from the cavity with decay rate of γ_C or the exciton decays through the non-radiative channel by the rate γ_X [Fig. 1.5(b)]. The energy exchange between the exciton and photon is a reversible process, known as
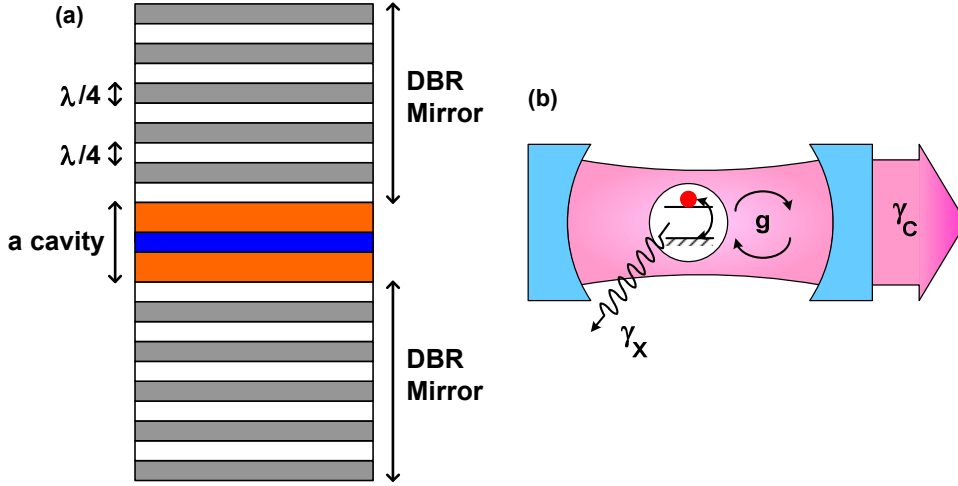
Figure 1.5: (a) Sketch of a semiconductor microcavity structure consisting of a cavity layer between two DBR mirrors. The quantum confined structure is embedded inside the cavity. (b) Schematic of a single two-level atom with the decay rate γ_X (including non-radiative dephasing rate and radiative decay rate of exciton outside the cavity) coupled to a single photon in a cavity with a photon loss rate γ_C by the coupling strength g.

the Rabi oscillation. The two polariton energies are given by [12]

$$
E_{1,2} = \frac{\omega_C + \omega_X}{2} - i\frac{\gamma_C + \gamma_X}{2} \pm \sqrt{\left(\frac{\omega_C + i\gamma_C - \omega_X - i\gamma_X}{2}\right)^2 + g^2}, \quad (1.25)
$$

$$
\delta = \omega_C - \omega_X, \quad (1.26)
$$

where ω_C, ω_X are the uncoupled cavity and exciton mode energies [dotted lines in Fig. 1.6(a)]. The three parameter g, γ_C, γ_X in Eq.(1.25) can be used to define the different regimes of exciton-light coupling. In the weak coupling regime ($g < \gamma_C, \gamma_X$), the real part of the energies $E_{1,2}$ are degenerate at zero detuning when the exciton mode is tuned to the cavity mode, corresponding to the crossing of the exciton and photon modes. In this case, the exciton decays well before any re-absorption/re-emission. The decay rate of irreversible emission can be enhanced by the Purcell effect [31]. In contrast, if the rate of absorption or emission of a photon by the exciton is faster than the photon decay rate from the cavity and the exciton decay rate ($g > \gamma_C, \gamma_X$), the system is in the strong coupling regime. The polariton dispersions are demonstrated
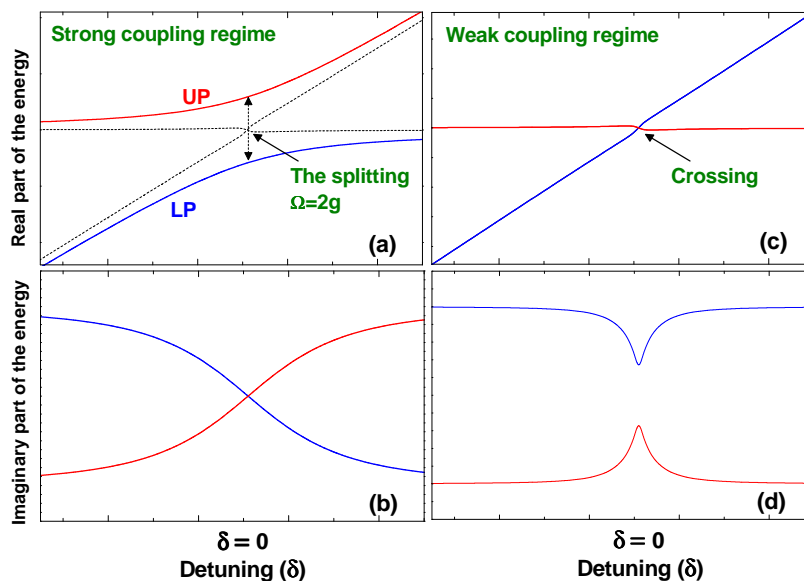
Figure 1.6: Real part and imaginary part of two eigenstates of polariton in the strong and weak coupling regimes: (a),(c) show the anticrossing and crossing of lower polariton (LP) and upper polariton (UP) energies at resonance, indicating that the system is in the strong and weak coupling regimes respectively. The vacuum Rabi splitting in the strong coupling regime is $\Omega = 2g$. (b),(d) the linewidth of polariton states, the exchange of the linewidth is observed in the case of the strong coupling regime.

in Fig. 1.6(a) and 1.6(c) for the strong and weak coupling regimes respectively, showing the anticrossing and crossing of the two polariton states at the resonance [13]. In the strong coupling regime, the energy splitting is characterized by the vacuum Rabi splitting ($\Omega = 2g$). The exchange of linewidths between two polariton states are clearly observed at the anticrossing, see Fig. 1.6(b). At resonance, the two polariton states have the same linewidth which is the average of two linewidths, $(\gamma_X + \gamma_C)/2$, because the states are the mixed of half-exciton and half-photon [18, 23, 32]. By contrast to the strong coupling regime, the linewidths of two polariton states in the weak coupling regime do not exchange their linewidths as shown in Fig. 1.6(d).

The average lifetime of photon inside the cavity before it escapes is proportional to the Q-factor of the cavity mode which is defined as the ratio of a resonant cavity frequency (ω_C) to the full width at half maximum (FWHM) of the cavity mode ($\delta\omega_C$), $Q = \omega_C/\delta\omega_C$. For an ideal cavity, the Q-factor is infinite. This means that a photon never goes away from the ideal cavity. In reality, the Q-factor and lifetime of

photon are finite. The photon can escape from the cavity due to the scattering by defects, interaction with the crystal lattice, etc.

1.7 SUMMARY

In this chapter, the basic concepts necessary for this thesis are explained. The chapter begins with the physics of excitons in bulk semiconductors and semiconductor nanostructures, in particular, QW (1D confinement) and QD (3D confinement) semiconductors. The energy levels of electron and hole are quantized due to the quantum confinement in a nanostructure. In QWs, the energy is quantized along z axis and particles can move freely in the x-y plane. For QDs, the particles are confined in all directions, so that their energy spectrum contains discrete levels. The effect of the applied electric field on excitons is also discussed, including formation of direct and indirect excitons and their quantum confined Stark effect.

The interaction between excitons in different systems and photons in a microcavity is in the focus of this research study. In a microcavity embedded nanostructure, a photon is re-absorbed and re-emitted by an exciton until the photon and exciton leak out of the cavity or decay via other nonradiative channels. In the strong coupling regime, the anticrossing of two polariton branches occurs and the energy splitting called the vacuum Rabi splitting is observed. Details of the theory and specific models used in this work are explained in more detail in the following chapters.

Chapter 2

Quantum Well Excitons

In this chapter, we present an efficient numerical approach which is used to calculate the optical properties of excitons in CQWs in the presence of an electric field. We are interested in optically allowed transitions in such systems and thus consider excitonic states with zero in-plane and angular momenta only. The optical properties including the exciton transition and binding energies, oscillator strength, lifetime and absorption are calculated as function of the electric field. The calculated results are compared to different experimental observations.

In CQW structures, the two QW layers are separated by a thin barrier. The electrons and holes reside in a QW layer due to the discontinuity in the band structure between the QW layer and the barrier. An electron and a hole localised in the same well form a direct exciton, while an indirect exciton is formed by an electron and a hole from different wells. As a result of a spatial separation between electron and hole, the indirect excitons in CQW have a long radiative lifetime and large dipole moment as compared to direct excitons. Due to these properties, indirect excitons have attracted much attention in the literature. When the electric field is applied perpendicular to the QW layer, the energies of electron and hole ground states are shifted to lower energy due to the quantum-confined Stark effect (QCSE), resulting in the decrease of the exciton transition and binding energies and the increase of its radiative lifetime [33–39].

Different theoretical approaches have been used to calculate the excitonic states in QW structures, ranging from variation methods [39–51] to direct diagonalizations in which the exciton wave function is expanded into a large basis [28] or the Schrödinger equation is discretized in the momentum space [2]. In this chapter, we present a straightforward way of solving the Schrödinger equation for an exciton in real space [52]. The single-particle states for electron and hole are written as a linear combination of Airy functions [35, 38, 53, 54] and the exciton wave function is expanded into a basis of uncorrelated electron-hole (e-h) pair states. In the following sections in this chapter, we explain the analytical and numerical method we used in our model and present results of calculation of the optical properties of excitons in CQWs.

2.1 EXCITONIC HAMILTONIAN

In the effective mass approximation, the excitonic Hamiltonian can be divided into three parts: the first two, $\hat{H}_e$ and $\hat{H}_h$, take into account the electron and hole quantization in heterostructure potentials V_e and V_h and the third one, $\hat{H}_X$, is responsible for the e-h in-plane relative motion and Coulomb binding:

$$\hat{H}(z_e, z_h, \rho) = \hat{H}_e(z_e) + \hat{H}_h(z_h) + \hat{H}_X(z_e, z_h, \rho) + E_g \,, \qquad (2.1)$$

with

$$\hat{H}_{e,h}(z) = -\frac{\hbar^2}{2}\frac{\partial}{\partial z}\frac{1}{m_{e,h}(z)}\frac{\partial}{\partial z} + V_{e,h}(z) \pm eFz \,, \qquad (2.2)$$

$$\hat{H}_X = -\frac{\hbar^2}{2\mu}\left(\frac{\partial^2}{\partial \rho^2} + \frac{1}{\rho}\frac{\partial}{\partial \rho}\right) - \frac{e^2}{\varepsilon_b\sqrt{(z_e - z_h)^2 + \rho^2}} \,, \qquad (2.3)$$

where $\hbar$ is reduced Planck constant, e is the electric charge, $z_e(z_h)$ is the electon (hole) coordinate in the QW growth direction (z axis), ρ is the in-plane coordinate, ε_b is the background dielectric constant that we assume to be z-independent, $m_{e(h)}$ the electron (hole) effective mass, and E_g is the bandgap of the well material. Due to the strong QW confinement, the heavy-hole subband is split off considerably and can be

approximated by an anisotropic effective mass using the Kohn-Luttinger parameters γ_1 and γ_2 [55]; leading to

$$\frac{1}{m_h} = \frac{1}{m_0}(\gamma_1 - 2\gamma_2)\,, \tag{2.4}$$

$$\frac{1}{\mu} = \frac{1}{m_e} + \frac{1}{m_0}(\gamma_1 + \gamma_2)\,, \tag{2.5}$$

where μ is the exciton in-plane reduced mass, and m_0 is the free electron mass. We assume a rectangular form of the heterostructure confinement potentials,

$$V_{e,h}(z) = \begin{cases} 0 & \text{inside the wells,} \\ \mathcal{V}_{e,h} > 0 & \text{outside,} \end{cases} \tag{2.6}$$

and similar step-like profiles for the electron and hole effective masses in the growth direction. The exciton wave function is expanded into a complete set of e-h pair states,

$$\Psi(z_e, z_h, \rho) = \sum_n \Phi_n(z_e, z_h)\phi_n(\rho)\,, \tag{2.7}$$

and

$$\Phi_n(z_e, z_h) = \tilde{\psi}_i^e(z_e)\tilde{\psi}_j^h(z_h)\,, \quad n = (i, j)\,, \tag{2.8}$$

where n is the unified pair index for the basis state which corresponds to the different electron and hole subbands (i, j). In this work, we truncate the infinite series by taking into account a few lowest e-h pair state $n = 1, 2, \ldots, N$. We use N up to 8 (2 electron and 4 hole states) in the case of large electric fields ($F > 70\,\text{kV/cm}$). A larger N used in the calculation provides a better accuracy. In a single quantum well (SQW) structure, the energy separation between subbands for both electron and hole is very large compared to the exciton binding energy, so that only the wave function of the single-particle ground state is sufficient for the expansion of exciton basis and the higher subbands are less important. The situation is different in the case of CQW structures in which the two QWs are electronically coupled to each other. The energy separation between ground state and excited state is much smaller compared to SQW. Therefore, the electron and hole excited states need to be taken

into account in order to obtain qualitatively correct results [44, 49, 56, 57]. The electron and hole single-particle wave functions $[\tilde{\psi}_i^e(z), \tilde{\psi}_j^h(z)]$ can be calculated by solving Schrödinger's equation with the Hamiltonian in Eq.(2.2) and the in-plane wave function $[\phi_n(\rho)]$ is then obtained from the full Hamiltonian Eq.(2.1). The numerical method will be explained in more details in Sections 2.3 and 2.5. In addition, the code for this calculation is available online [58].

2.2 STRUCTURES AND PARAMETERS

Our model provides a general method of excitonic state calculation in arbitrary CQW structures. However, we study in this work only two specific structures used in experiments: symmetric 8-4-8-nm GaAs/Al$_{0.33}$Ga$_{0.67}$As CQW [24, 59, 60] and asymmetric 10-4-10-nm In$_{0.08}$Ga$_{0.92}$As/GaAs/In$_{0.1}$Ga$_{0.9}$As CQW [61–64]. These two structures consist of two QW layers separated by a thin barrier and surrounded on both sides by thick barriers of the same kind. The electric field is applied in the growth direction. The band diagrams are demonstrated in Fig. 2.1. The background dielectric constant (ϵ_b) and reduced mass (μ) are assumed to be z-independent. The Al$_x$Ga$_{1-x}$As (In$_x$Ga$_{1-x}$As) alloy parameters are linearly interpolated between those of GaAs and AlAs (InAs) as shown in Table 2.1.
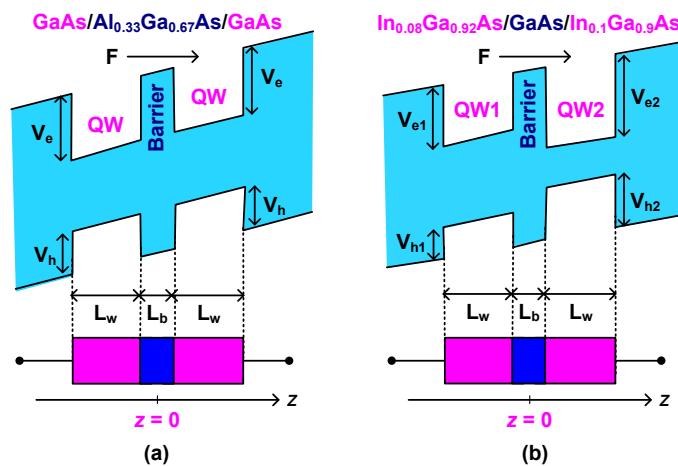
Figure 2.1: Band diagram of a symmetric 8-4-8-nm GaAs/Al$_{0.33}$Ga$_{0.67}$As (a) and asymmetric 10-4-10-nm In$_{0.08}$Ga$_{0.92}$ (b) CQW structures.

Parameter	GaAs/Al$_x$Ga$_{1-x}$As	GaAs/In$_x$Ga$_{1-x}$As
Well width (L_w)	8 nm	10 nm
Barrier width (L_b)	4 nm	4 nm
Energy band offset (ΔE_g)	1.247x [44]	1.5837x - 0.475x^2 [65]
Potential $V_e : V_h$ ratio	65:35 [2]	65:35
Background dielectric constant (ϵ_b)	12.5 [44]	11 [66]
Electron mass (m_e)	0.0665 + 0.0835x [67]	0.0665 - 0.0435x [68]
Hole mass (m_h)	0.34 + 0.41x [67]	0.34 - 0.02x [68]
Reduced mass (μ)	0.0421	0.0396
Dipole matrix element (d_{cv})	0.6 [69, 70]	0.6 [69, 70]

Table 2.1: Parameters for a symmetric 8-4-8-nm GaAs/Al$_{0.33}$Ga$_{0.67}$As and asymmetric 10-4-10-nm In$_{0.08}$Ga$_{0.92}$As/GaAs/In$_{0.1}$Ga$_{0.9}$As CQW structures used in the calculation

2.3 SINGLE-PARTICLE EIGENSTATES

We first consider the single-particle states in the z direction. The wave functions satisfy the following one-dimensional equations:

$$\hat{H}_{e,h}(z)\psi^{e,h}(z) = E^{e,h}\psi^{e,h}(z) \,, \qquad (2.9)$$

where $E^{e,h}$ are the electron and hole energies. For an electron in the rectangular confinement potential $V_e(z)$ [Eq.(2.6)] and uniform electric field F, the Schrödinger equation for the electron takes the form

$$\frac{\partial}{\partial z}\frac{1}{m_e(z)}\frac{\partial}{\partial z}\psi^e(z) - \frac{2}{\hbar^2}\left(eFz + V_e(z) - E^e\right)\psi^e(z) = 0 \,. \qquad (2.10)$$

By introducing

$$\xi(z) = \left(\frac{2m_e eF}{\hbar^2}\right)^{1/3}\left[z - \frac{E^e - V_e(z)}{eF}\right]. \qquad (2.11)$$

The electron wave function in each layer of the structure is given by a superposition of two Airy functions [71, 72]

$$\psi^e(z) = a_k \text{Ai}(\xi) + b_k \text{Bi}(\xi) \,, \qquad (2.12)$$

31

where the index k labels the heterostructure layers (from left to right) taking integer values from 1 to 5. The electron eigenenergy E^e and five pairs of coefficients (a_k, b_k) in Eq.(2.12) are found from four pairs of BCs on heterostructure interfaces and two BCs at $z \to \pm\infty$.

The interface BCs are the continuity of wave function $\psi^e(z)$ and its derivative $m_e^{-1}(z)\partial\psi^e(z)/\partial z$. The other two BCs take into account the possibility for the electron to tunnel through the barrier and escape from the system to the side of the CQW structure where the applied electric field gradually lowers the potential. In that area, the solution is given by a wave propagating away from the system. For the electron wave function and $F>0$, this outgoing wave BC at $z \to -\infty$ yields $b_1 = -ia_1$ which follows from the specific combination of the Airy functions $\mathrm{Ai}(\xi) - i\mathrm{Bi}(\xi)$ producing an outgoing wave [38, 71]. At the same time, the electron cannot escape to the other side of the structure where the potential gradually increases, and thus the other BC, typical for bound/localized states, is $\psi^e(z \to +\infty) = 0$, giving $b_5 = 0$ due to the asymptotics of the Airy function [71]. Finally, the electron wave functions in each layer of CQW structure are given by

$$\psi_e(z) = \begin{cases} a_1[Ai[\xi(z)] - iBi[\xi(z)]] & \text{if } z < -(L_w + L_b/2) \\ a_2 Ai[\xi(z)] + b_2 Bi[\xi(z)] & \text{if } -(L_w + L_b/2) \leq z < -L_b/2 \\ a_3 Ai[\xi(z)] + b_3 Bi[\xi(z)] & \text{if } -L_b/2 \leq z < L_b/2 \\ a_4 Ai[\xi(z)] + b_4 Bi[\xi(z)] & \text{if } L_b/2 \leq z < (L_w + L_b/2) \\ a_5 Ai[\xi(z)] & \text{if } z > (L_w + L_b/2) \end{cases} \quad (2.13)$$

where $z=0$ is at the centre of the structure as indicated in Fig.2.1.

The form of the wave function and the BCs for the hole are found in a similar way, taking into account that the potential grows in the opposite direction. The Schrödinger equation for the hole has the form

$$\frac{\partial}{\partial z}\frac{1}{m_h(z)}\frac{\partial}{\partial z}\psi^h(z) - \frac{2}{\hbar^2}\left(-eFz + V_h(z) - E^h\right)\psi^h(z) = 0. \quad (2.14)$$

32

The hole wave functions are written as

$$\psi_h(z) = \begin{cases} c_1 Ai[\vartheta(z)] & \text{if } z < -(L_w + L_b/2) \\ c_2 Ai[\vartheta(z)] + d_2 Bi[\vartheta(z)] & \text{if } -(L_w + L_b/2) \le z < -L_b/2 \\ c_3 Ai[\vartheta(z)] + d_3 Bi[\vartheta(z)] & \text{if } -L_b/2 \le z < L_b/2 \\ c_4 Ai[\vartheta(z)] + d_4 Bi[\vartheta(z)] & \text{if } L_b/2 \le z < (L_w + L_b/2) \\ c_5 [Ai[\vartheta(z)] - iBi[\vartheta(z)]] & \text{if } z > (L_w + L_b/2) \end{cases} \tag{2.15}$$

with

$$\vartheta(z) = \left(\frac{2m_h eF}{\hbar^2}\right)^{1/3} \left[-z - \frac{E^h - V_h(z)}{eF}\right]. \tag{2.16}$$

The secular equation following from all ten BCs determines discrete eigenvalues of Eq.(2.9),

$$E_j^{e,h} = \tilde{E}_j^{e,h} - i\Gamma_j^{e,h}, \tag{2.17}$$

which are the complex energies of electron/hole resonant states, also known in the literature as Siegert states [73]. The real part of the eigenvalue $[\tilde{E}_j^{e(h)}]$ is the energy position of the electron (hole) j-th resonant level, while the imaginary part $[\Gamma_j^{e(h)}]$ gives its tunneling linewidth.

The wave function of any resonant state having a finite linewidth is essentially complex, i.e. it cannot be made real by any uniform phase shift. Also, its amplitude grows exponentially to the outside area to which the particle can escape and thus has to be normalized to its flux [73, 74]. This normalization includes a divergent volume integral and a compensating surface term. For the values of the electric field considered in this paper, the calculated linewidths of the electron and hole states of interest are always small compared to their energies of quantization. Similarly, the imaginary parts of the wave functions are small compared to the real ones and can be dropped. The normalization condition is then taken in a form

$$\int_{z_{\min}}^{z_{\max}} \left[\tilde{\psi}_j^{e,h}(z)\right]^2 dz = 1, \tag{2.18}$$

where $\tilde{\psi}_j^{e,h} = \text{Re}(\psi_j^{e,h})$. The limits of integration in Eq.(2.18) $[z_{\min}, z_{\max}]$ taken to be the same for electron and hole, are two distant points on both sides of the CQW. In

this region, the wave functions decay considerably before they start to grow exponentially owing to the carrier tunneling. Therefore, the surface terms are minimized and can be dropped leaving in the normalization only finite-volume integrals.

2.4 ENERGY SUBBANDS AND WAVE FUNCTIONS

The calculated electron (E_i^e for i=1,2) and hole (E_j^h for j=1-4) subbands in the presence of the electric field are shown in Fig. 2.2. The energy levels of electron and hole experience the Stark shifts $\tilde{E}_{1,2}^{e(h)}(F) \approx \tilde{E}_{1,2}^{e(h)}(0) \mp dF/2$, where $d = L_w + L_b$ is the center-to-center distance between the QWs. As the electric field grows, the ground state (GS) is red-shifted, while the energy of the first excited state (ES) is shifted to higher energies. The GS-ES splittings increase almost linearly with the electric field.
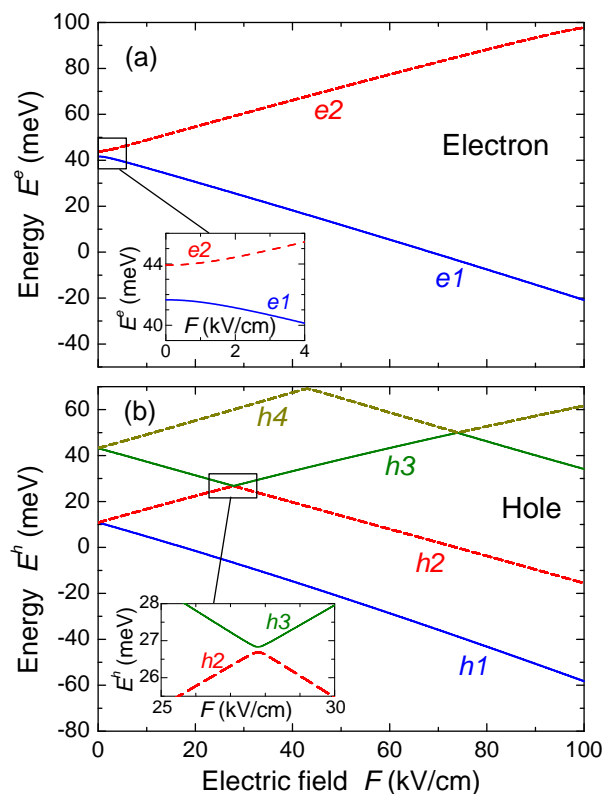
Figure 2.2: Energies of two electron states (a) and four hole states (b) in a symmetric 8-4-8-nm GaAs/Al$_{0.33}$Ga$_{0.67}$As CQW as functions of an applied electric field. Insets show spectral regions with anticrossing.
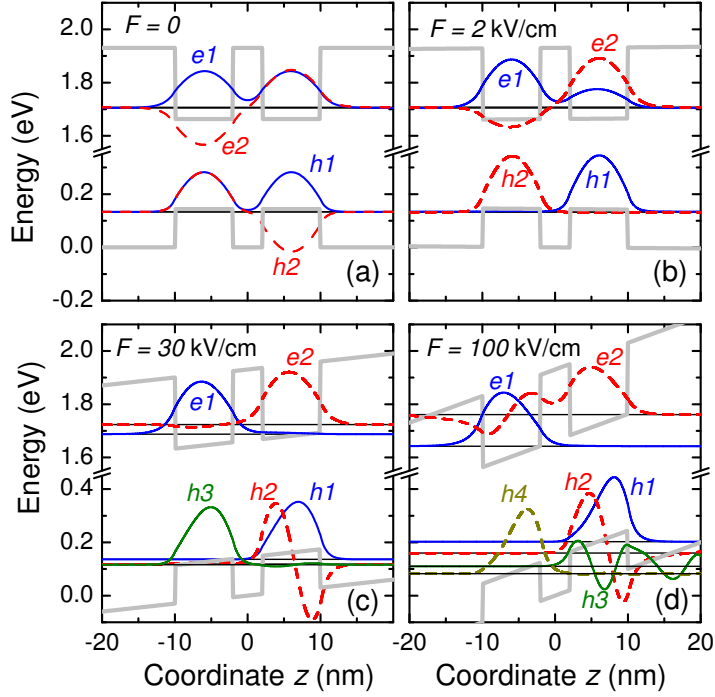
Figure 2.3: Wave functions and energy levels of electron and hole ground and excited states in a symmetric 8-4-8-nm $GaAs/Al_{0.33}Ga_{0.67}As$ CQW for different values of the electric field $F = 0, 2, 30, 100\,kV/cm$. Gray lines show CQW heterostructure potentials.

The corresponding wave function for electron ($\tilde{\psi}_i^e$) and hole ($\tilde{\psi}_j^h$) are demonstrated in Fig. 2.3 for a few different values of the electric field. At zero field, the GS and the first ES have symmetric and antisymmetric wave functions respectively. With increasing electric field, the wave functions become asymmetric. The wave function maxima for electron and hole GSs move in the opposite directions, for the electron it moves to the left QW and for the hole it moves to the right QW. It is also found that the GS and the first ES for the same carrier are confined in different QWs. This happens to both carriers already at very low electric field (F=2 kV/cm); see Fig. 2.3(b). At F=30 kV/cm [Fig. 2.3(c)], the first hole ES jumps from the left to the right QWs. This corresponds to an anticrossing of hole ES subband that takes place at F=27.8 kV/cm; see in the inset in Fig. 2.2(b). Therefore, the second ES (h3) must be taken into account in the calculation for $F \geq 25$ kV/cm. Such an anticrossing behavior was also found in the previous calculation [2, 42]. The same happens also to the electron ES subband at a much higher electric field. Figure 2.3(d) shows the wave

35
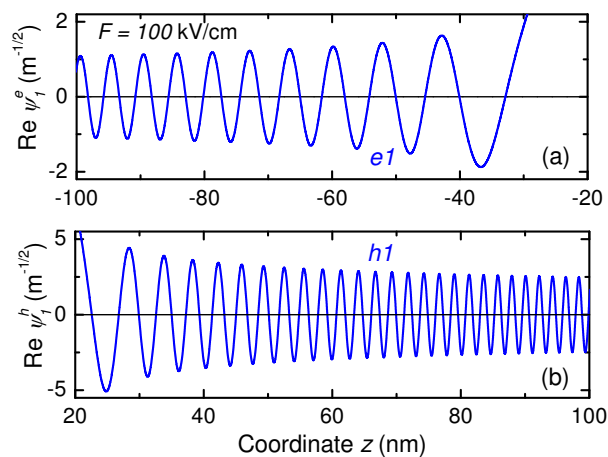
Figure 2.4: Oscillating tails in the wave function for (a) electron and (b) hole ground states at $F=100\,\text{kV/cm}$.

functions at $F=100\,\text{kV/cm}$, it is clearly seen that the system requires the higher hole subbands (h3 and h4) to be taken into account due to the h3-h4 anticrossing in the hole subband energy. For the electron wave function, the first ES maxima starts to move from the right to the left QW.

Figure 2.4 demonstrates the oscillations in the wave function of the electron and hole GSs in the region far from the CQW structure. The amplitudes of about $2\,\text{m}^{-1/2}$ and $5\,\text{m}^{-1/2}$ for electron and hole, respectively, in Fig.2.4 are very small in reality: they are about four orders of magnitude smaller than the wave function maximum in Fig.2.3(d). This tiny oscillatory behavior with increasing frequency occurs due to the lowering of the potential by the electric field. The frequency of the oscillations for the hole is larger than that for the electron because $V_h < V_e$.

2.5   EXCITONIC STATES

The main purpose of this section is to study the optical properties of excitons in CQWs in the presence of electric field. We calculate excitonic states by solving the Schrödinger equation for the exciton which is given by

$$\left[\hat{H}_e(z_e) + \hat{H}_h(z_h) + \hat{H}_X(z_e, z_h, \rho) + E_g\right]\Psi(z_e, z_h, \rho) = E_X\Psi(z_e, z_h, \rho). \qquad (2.19)$$

The first two terms of the Hamiltonian are treated by using solution of Eq.(2.9). Due to the orthonormality of the single-particle wave function, multiplying Eq.(2.19) by $\Phi_n(z_e, z_h)$ and integrating over both z-coordinates brings it to the form

$$\left[\hat{K}(\rho) + E_n^{(0)} - E_X \right] \phi_n(\rho) + \sum_{m=1}^{N} V_{nm}(\rho)\phi_m(\rho) = 0 \,, \tag{2.20}$$

with

$$\hat{K}(\rho) = -\frac{\hbar^2}{2\mu} \left(\frac{\partial^2}{\partial \rho^2} + \frac{1}{\rho}\frac{\partial}{\partial \rho} \right) \,, \tag{2.21}$$

$$V_{nm}(\rho) = -\frac{e^2}{\varepsilon_b} \int \int_{z_{\min}}^{z_{\max}} \frac{\Phi_n(z_e, z_h)\Phi_m(z_e, z_h)}{\sqrt{(z_e - z_h)^2 + \rho^2}} \, dz_e dz_h \,, \tag{2.22}$$

$$E_n^{(0)} = \tilde{E}_i^e + \tilde{E}_j^h + E_g \,. \tag{2.23}$$

The exciton transition energy E_X and the in-plane components of the wave function, $\phi_n(\rho)$, are obtained by solving the matrix differential equation [Eq.(2.20)] numerically. To do so, we introduce a matrix generalization of the shooting method applying the latter to a system of coupled differential equations. The shooting method transforms a boundary-value problem like Schrödinger's equation with BCs to an initial-value problem in which one of the boundary values (in the present case the wave function at $\rho \to \infty$) is taken as a starting point. The boundary value on the other side (at $\rho = 0$) is then used to find the eigenenergies. The BCs follow straightforwardly from Eq.(2.20) and the asymptotics of the Coulomb matrix elements $V_{nm}(\rho)$. At large distances $V_{nm}(\rho) \to -\delta_{nm}e^2/(\varepsilon_b\rho)$, while at small distances the potentials $V_{nm}(\rho)$ have logarithmic dependence. Therefore, for bound states

$$\phi_n(\rho \to \infty) = A_n \rho^{s_n} e^{-\alpha_n \rho} \,, \tag{2.24}$$

where $\alpha_n = \sqrt{2\mu(E_n^{(0)} - E_X)}/\hbar$ and $s_n = \mu e^2/(\hbar^2 \varepsilon_b \alpha_n) - 1/2$, and

$$\phi_n'(0) = 0 \,. \tag{2.25}$$

37

The wave function amplitudes A_n are the unknowns which can be found along with the eigenvalue E_X.

Discretizing Eq.(2.20) on a finite grid, a numerical solution in the area $0 \leq \rho \leq R$ is generated iteratively using a finite difference scheme

$$\frac{\partial \phi_n(\rho)}{\partial \rho} \approx \frac{\phi_n(\rho + \Delta\rho) - \phi_n(\rho - \Delta\rho)}{2\Delta\rho} \tag{2.26}$$

$$\frac{\partial^2 \phi_n(\rho)}{\partial \rho^2} \approx \frac{\phi_n(\rho + \Delta\rho) - 2\phi_n(\rho) + \phi_n(\rho - \Delta\rho)}{(\Delta\rho)^2} \tag{2.27}$$

This brings Eq.(2.20) to the following discrete form

$$\phi_n(\rho - \Delta\rho) = -\phi_n(\rho + \Delta\rho)\frac{2\rho + \Delta\rho}{2\rho - \Delta\rho} + \sum_{m=1}^{N} F_{nm}(\rho)\phi_m(\rho) , \tag{2.28}$$

with

$$F_{nm} = \left[4\rho - \frac{2\mu}{\hbar^2}(2\rho\Delta\rho^2)(E_m^{(0)} - E_X) \right] \delta_{nm} - \frac{2\mu}{\hbar^2}(2\rho\Delta\rho^2)V_{nm}(\rho) , \tag{2.29}$$

where $\Delta\rho$ is the discretization step. Going to the very last point $\rho = 0$ and using the BC Eq.(2.25) produces a homogeneous matrix equation for the amplitudes A_m:

$$\sum_{m=1}^{N} M_{nm}(E_X)A_m = 0, \tag{2.30}$$

in which $M_{nm}(E_X)$ depends solely on the exciton energy E_X (and not on ρ any more), and thus the energy eigenvalues are determined by

$$\det |M_{nm}(E_X)| = 0 . \tag{2.31}$$

For small values of the electric field, the electron and hole GS-ES splittings are smaller than the exciton Coulomb energy and thus several bound states [having the asymptotics given by Eq.(2.24)] can always be found in the system. However, as

the electric field grows, the Coulomb energy of the exciton ESs is getting smaller than the e-h pair splitting energies and thus some of these exciton states become unbound. Since the unbound states have energies $E_X > E_1^{(0)}$, at least for some of their radial components the asymptotics Eq.(2.24) is no longer valid and a proper treatment of the excitonic continuum is required. This task is outside the scope of the present work which mainly concentrates on exciton bound states. Nevertheless, some effects of the continuum and in particular its influence on the excitonic absorption spectrum can be taken into account, in a first attempt, by restricting the exciton in-plane motion to a large circle of radius R and in this way discretizing the continuum. The asymptotic BCs Eq.(2.24) are now replaced by

$$\phi_n(R) = 0, \quad \phi_n(R - \Delta\rho) = A_n, \tag{2.32}$$

where the new amplitudes A_n satisfy the same Eq.(2.30) with matrix $M_{nm}(E)$ being redefined accordingly.

It is convenient to normalize the radial components of the wave functions introducing expansion coefficients C_n:

$$\phi_n(\rho) = C_n \tilde{\phi}_n(\rho), \tag{2.33}$$

where $\tilde{\phi}_n(\rho)$ is normalized to $2\pi \int_0^\infty |\tilde{\phi}_n|^2 \rho d\rho = 1$, and therefore

$$\sum_{n=1}^{N} |C_n|^2 = 1, \tag{2.34}$$

due to orthogonality of the e-h pair states $\Phi_n(z_e, z_h)$ and normalization of the total exciton wave function $\Psi(z_e, z_h, \rho)$.

Finally, for each excitonic state, the oscillator strength is calculated as [75, 76]

$$f = \frac{2m_0 E_X |d_{cv}|^2}{\hbar^2} \left| \int_{z_{\min}}^{z_{\max}} \Psi(z, z, \rho = 0) \, dz \right|^2, \tag{2.35}$$

where d_{cv} is the basic dipole matrix element between the valence and conduction bands, and the overlap integral in Eq.(2.35) accounts for the spatial distribution of the excitonic recombination. The exciton radiative linewidth is then given by

$$\Gamma_R = \frac{\pi e^2 \hbar}{\sqrt{\varepsilon_b} m_0 c} f \, , \tag{2.36}$$

where c is the speed of light.

2.6 EXCITON ENERGY

In calculation of the exciton states for small or moderate electric field, it is sufficient to consider the two lowest levels for the electron $(e1, e2)$ and two for the hole $(h1, h2)$. We are thus dealing with four e-h pair states. We label these four basis states as $e1h1$ ($n=1$), $e1h2$ ($n=2$), $e2h1$ ($n=3$), and $e2h2$ ($n=4$), where n is the unified pair index introduced in Eq.(2.8). The electric field dependence of the exciton energies in CQW is demonstrated in Fig. 2.5. The exciton oscillator strength is proportional to the circle area. In this calculation, the in-plane exciton confinement radius is restricted to be R=200 nm and 800 nm. In the latter case, the excitonic continuum has a much finer discretization. This makes more clear which states belong to the continuum and which are the true bound states having more or less isolated energy positions, weakly dependent on R. For example, the $2S$ and $3S$ states of the indirect exciton are clearly identified in Fig. 2.5(b). They lie just below the discretized continuum onset and are down-shifted with the electric field almost parallel to the exciton ground state (X-GS). It is also found that there is a direct state having the maximum oscillator strength in the excitonic spectrum which remains almost unaffected. This state is called the direct exciton excited state (X-ES). Higher excited states of the direct exciton are also well seen in Fig. 2.5(b). They are deep in the continuum (7-8 meV above the X-ES) and are weakly dependent on the electric field.
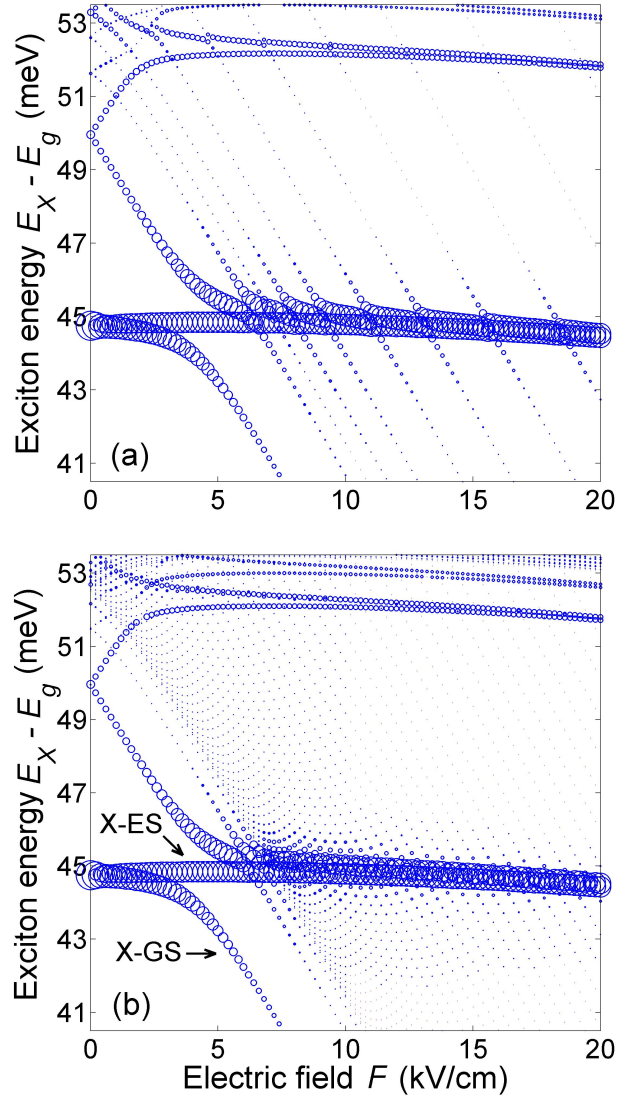
Figure 2.5: Electric field dependence of the optical transition energy E_X for different exciton states in a symmetric 8-4-8-nm GaAs/Al$_{0.33}$Ga$_{0.67}$As CQW structure, calculated using the exciton confinement radius $R = 200\,$nm (a) and $800\,$nm (b). The circle area is proportional to the exciton oscillator strength f. The energy gap $E_g = 1.519\,$eV for GaAs QW layers.

2.7 Direct-to-indirect crossover in an applied electric field

QW localization of the X-GS and X-ES is for different values of the electric field is illustrated in Fig. 2.6. At zero field, both states have two identical maxima on the main diagonal $z_e = z_h$ [Fig. 2.6(a) and 2.6(f)], due to the symmetry of the system. Increasing electric field causes one of the two peaks to become smaller and then to vanish, see Fig. 2.6(b)-2.6(c) for X-GS and Fig. 2.6(g)-2.6(h) for X-ES. These states become asymmetric direct-exciton states. The electron and hole reside in the right QW for X-GS and in the left QW for X-ES. Further increase of the electric field up to F=6 kV/cm leads to the X-GS switching from a direct to an indirect state. The peak moves away from the main diagonal toward the bottom right corner as clearly seen in Fig. 2.6(c)-2.6(e). This result is in a good agreement with the previous theoretical studies [2, 28] and experimental observations [24].

Figure 2.7 shows the radial components $\phi_n(\rho)$ of the X-GS and X-ES wave functions for different values of electric field. To explain this figure clearly, we need to consider the Coulomb matrix elements (V_{nm}) calculated from Eq.(2.23). Figure 2.8 shows an example of the Coulomb matrix elements at F=4 kV/cm, though this picture does not change much when the electric field increases or decreases. The pair states with electron and hole in the same QW (n=2 and n=3) are electrically neutral and can be called direct states, while the other states (n=1 and n=4) are indirect states and have nonzero dipole moment because the electron and hole are in different QWs. For the diagonal Coulomb matrix elements, the potentials for the direct pairs (V_{22}, V_{33}) are a few times stronger than that for the indirect pairs (V_{11}, V_{44}). The off-diagonal elements are much smaller because of the small overlap integrals of the wave functions. The Coulomb coupling matrix elements $V_{13} \approx V_{24}$ are responsible for the mixing of direct and indirect pair states.

At F=0.1 kV/cm, all four radial components of the wave function in Fig. 2.7(a) have comparable contributions to the X-GS and X-ES. At F=2 kV/cm[Fig. 2.7(b)], the direct e-h pair state (n=3) has the dominant contribution to the X-GS. This state is strongly coupled to the indirect pair state (n=1) via the Coulomb matrix element
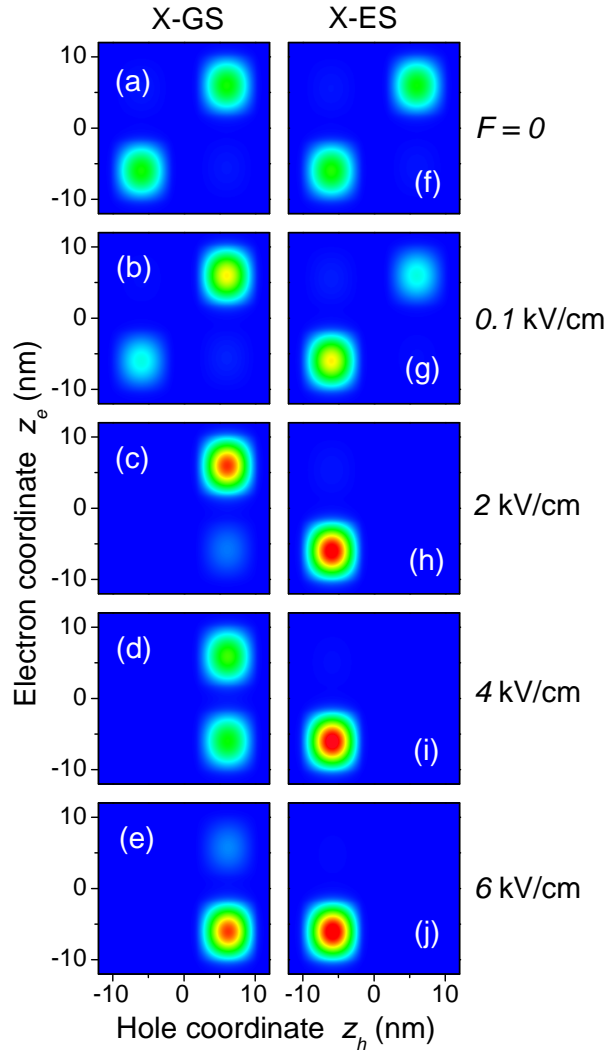
Figure 2.6: Probability distributions $\int_0^\infty |\Phi(z_e, z_h, \rho)|^2 \, 2\pi\rho d\rho$ calculated for the exciton ground state X-GS [(a)-(e)] and excited state X-ES [(f)-(j)], for different values of the electric field.
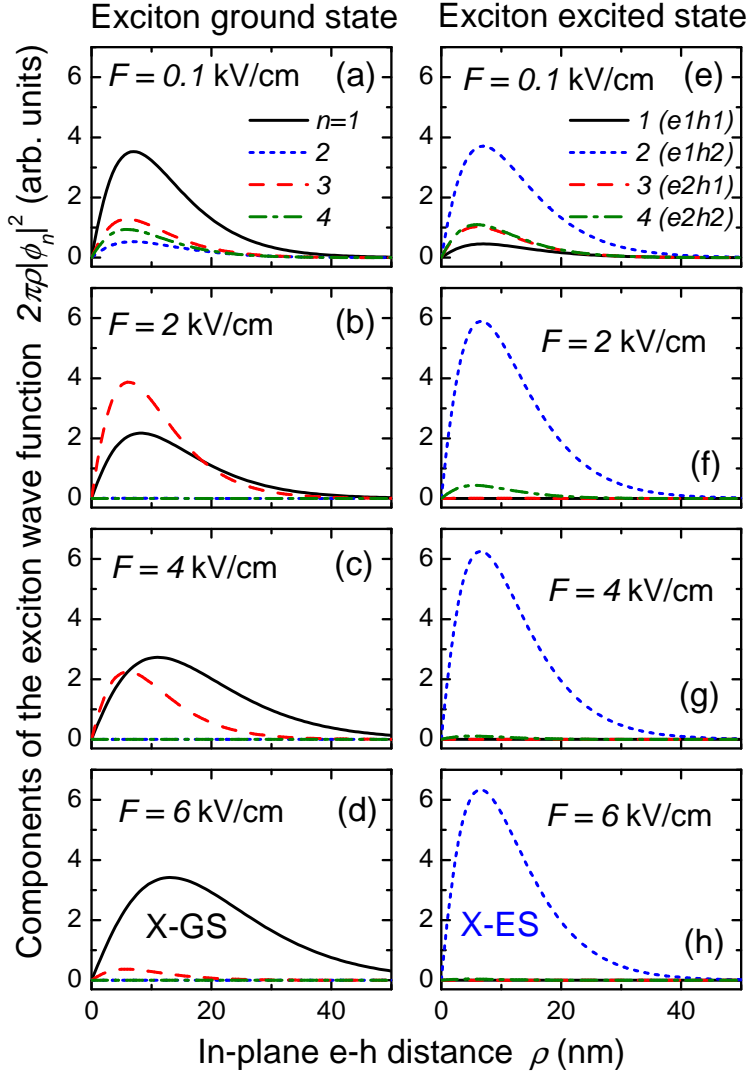
Figure 2.7: Radial components $2\pi\rho|\phi_n(\rho)|^2$ of the exciton wave function calculated for the ground state X-GS [(a)-(d)] and excited state X-ES [(e)-(h)] for different values of the electric field.
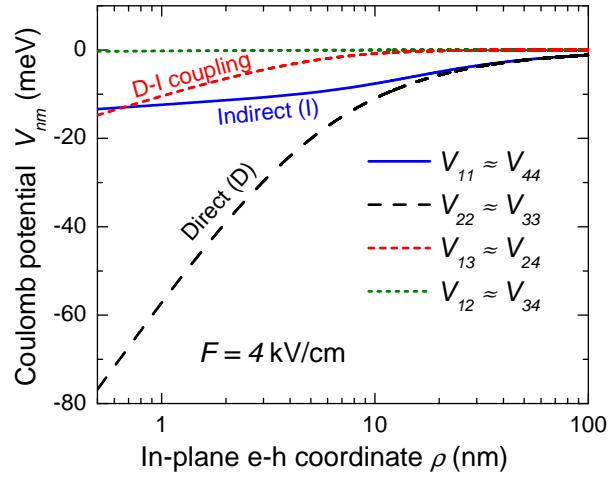
Figure 2.8: Matrix elements V_{nm} of Coulomb potential calculated from Eq.(2.23) for different e-h pair states at $F = 4\,\text{kV/cm}$.
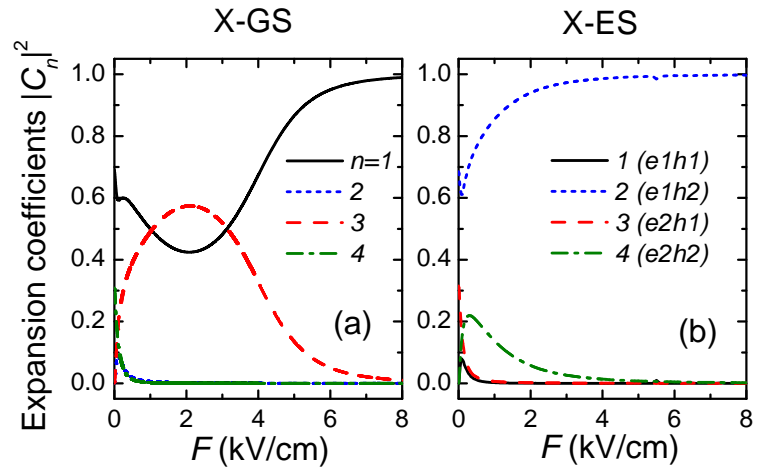
Figure 2.9: Coefficients C_n of the expansion of the exciton wave function into e-h pair states calculated for the ground state X-GS (a) and excited state X-ES (b) as functions of the electric field F.

V_{13}, shown in Fig. 2.8. As the electric field increases, the indirect component ϕ_1 grows and the direct component ϕ_3 reduces due to the direct-to-indirect (D-I) switching; see in Fig. 2.7(c)-2.7(d). Nothing similar happens to the X-ES. The X-ES wave function is dominated by the direct $n=2$ pair state. Although, this state is strongly coupled via V_{24} to the indirect state $e2h2$ ($n=4$), the $n=4$ pair state is Stark blue shifted and detuned from the $e1h2$ state. As a result, the energy position of this direct exciton excited state (X-ES) remains practically unchanged. Therefore, only a minor contribution of the ϕ_4 component to the X-ES can be seen in Fig. 2.7(f)-2.7(h).

Figure 2.9 summarizes our analysis showing the field dependence of e-h pair amplitudes C_n introduced in Eq.(2.33). It demonstrates the prominent D-I crossover in the X-GS, a much weaker D-I coupling in the X-ES, and a very quick transition from symmetric-antisymmetric coupling to D-I coupling, seen in the wave functions of both X-GS and X-ES.

2.8   Binding energies and comparison with a single state basis calculation

Figure 2.10 demonstrates the field dependence of the optical transition energy (E_X), the binding energy (E_b), the in-plane Bohr radius ($r_b=\sqrt{\langle\rho^2\rangle}$), and the radiative linewidth (Γ_R) for X-GS and X-ES. For $F>6\,\mathrm{kV/cm}$, the X-GS transition energy exhibits a considerable Stark shift due to a large e-h separation of indirect exciton [Fig. 2.10(a)]. The X-ES in turn has a very weak field dependence due to a much smaller dipole moment of direct exciton. However, the red shift of X-ES transition energy is also observed in a large range of the electric field. This is because the electric field causes a large e-h separation in the same QW. The binding energy of X-GS is determined as $E_b = E_1^{(0)} - E_X$. The X-GS binding energy drops rapidly from $8\,\mathrm{meV}$ to $4\,\mathrm{meV}$ [Fig. 2.10(b)] as a result of the transition from direct to indirect Coulomb coupling. For the X-ES, the dominant component is $e1h2$ ($n=2$), while the lowest-energy pair state ($e1h1$) has a negligible contribution to the X-ES (for $F>1\,\mathrm{kV/cm}$). Therefore, the X-ES binding energy can be defined as the energy distance from X-ES
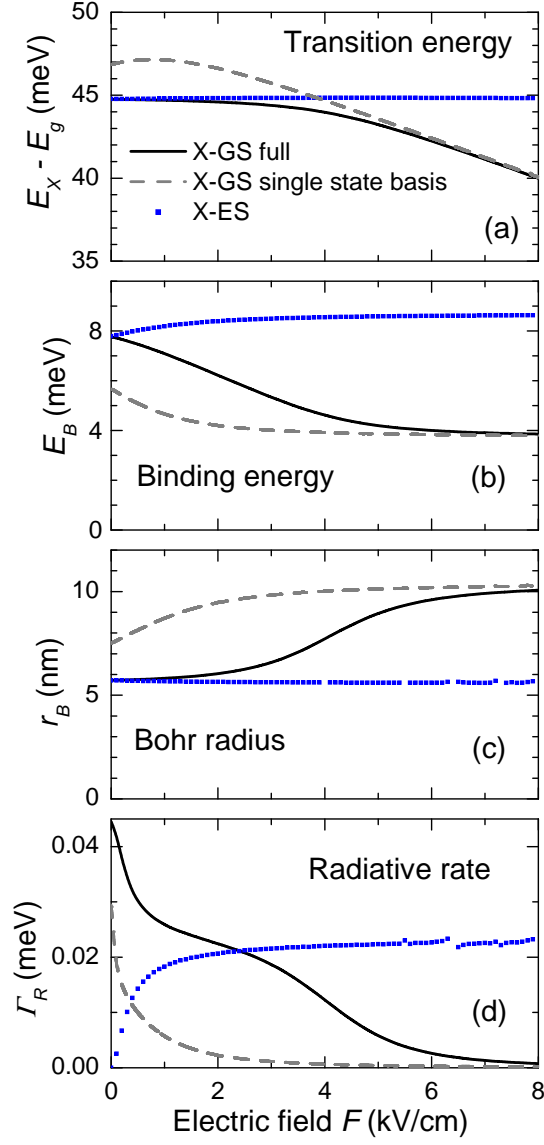
Figure 2.10: (a) Optical transition energy E_X, (b) binding energy E_b, (c) in-plane Bohr radius $r_B = \sqrt{\langle \rho^2 \rangle}$, and (d) radiative rate Γ_R of the exciton ground state X-GS (solid lines) and excited state X-ES (full squares) as functions of the electric field. Dashed lines are the single-state basis calculation of the X-GS. The energy gap $E_g = 1.519\,\text{eV}$ for GaAs QW layers.

to its own continuum onset: $E_b = E_2^{(0)} - E_X$. The Bohr radius in Fig. 2.10(c) is fully correlated with the binding energy, increasing with the electric field almost by a factor of two for the X-GS and showing no change for the X-GS.

The radiative linewidths calculated via Eq.(2.36) are shown in Fig. 2.10(d). Similar to the oscillator strength, the X-GS linewidth decreases dramatically when the X-GS experiences the D-I crossover. The X-ES, in turn, becomes bright in a finite electric field. The linewidth quickly increases with the electric field up to the half of the X-GS maximum linewidth. Further increase of the electric field does not change the X-ES radiative rate much. The fluctuations in the X-ES data seen in Fig. 2.10(d) for $F > 6 \, \text{kV/cm}$ occur due to the influence of the higher ESs which anticross and perturb the X-ES, see Fig. 2.5.

In Fig. 2.10, we present also the result of a single-state basis (SSB) calculation [56] in which only the electron and hole GSs are taken into account. In this case, the expansion in Eq.(2.7) for the exciton is reduced to a single term ($N=1$) due to e-h pair state $e1h1$. For small values of the electric field, the SSB calculation shows considerably different results compared to the full calculation in all four plots. The reason for such a difference is clearly seen in Fig. 2.9(a). Indeed, the direct pair state $e2h1$ ($n=3$) has to be taken into account for a proper description of the X-GS wave function. Omitting this state in the SSB calculation causes the blue shift of the exciton transition energy at small electric field [44, 56, 57] and underestimates the X-GS binding energy by a factor of 1.5 and the X-GS radiative linewidth by an order of magnitude. However, the SSB model adequately describes the properties of the X-GS at larger electric fields where the indirect exciton is strongly dominated by $e1h1$ ($n=1$) component.

2.9 EXCITONS IN SYMMETRIC AND ASYMMETRIC COUPLED QUANTUM WELL STRUCTURES

In this section, we consider an asymmetric $In_{0.08}Ga_{0.92}As/GaAs/In_{0.1}Ga_{0.9}As$ CQW structure used in Ref. [62] and compare the calculated results with those for
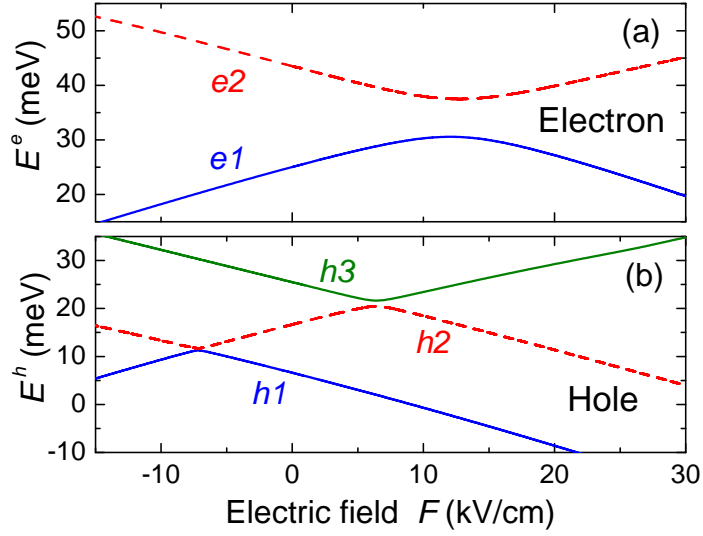
Figure 2.11: Energies of two electron states (a) and two hole states (b) in an asymmetric $In_{0.08}Ga_{0.92}As/GaAs/In_{0.1}Ga_{0.9}As$ (10-4-10-nm) CQW as functions of the electric field.

the symmetric GaAs/AlGaAs CQW structure. The asymmetric CQW consists of two 10 nm $In_xGa_{1-x}As$ layers with x=0.08 and 0.1 for a left and right wells respectively. A barrier layer is GaAs with a width of 4 nm. The different content of In in QW layers results in the different values of the confinement potential in the left and right QWs. The calculated electron and hole energies as functions of electric field are shown in Fig. 2.11. The anticrossings in the electron/hole subbands due to the wave function maxima moving from one QW to another QW are also seen in this asymmetric CQW. For example, the h2 anticrossing takes place at around F=6.4 kV/cm. The wave function for h2 subband at F=0 (before anticrossing) and F=12.5 (after it) are plotted in Fig. 2.12(b) and 2.12(c) respectively. It can be seen that the maxima move from the left to the right QW. Due to the asymmetry in the energy band structure, formation of symmetric and antisymmetric electronic states is not seen at F=0 [Fig. 2.12(b)] as it happens in the case of symmetric CQW. However, the asymmetry can be compensated by the electric field. As a result, the symmetric and antisymmetric states are observed at F=-7.2 kV/cm for the hole and F=12.5 kV/cm for the electron, see Fig. 2.12(a) and 2.12(c), respectively.
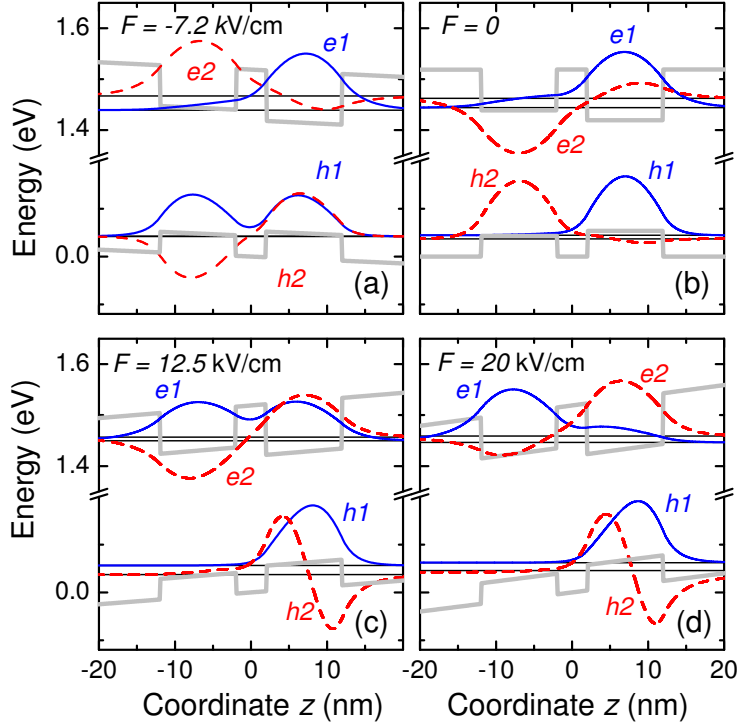
Figure 2.12: Wave functions and energy levels of electron and hole ground and excited states in an asymmetric $In_{0.08}Ga_{0.92}As/GaAs/In_{0.1}Ga_{0.9}As$ (10-4-10-nm) CQW for different values of the electric field. Gray lines show CQW heterostructure potentials.

The calculated exciton energies and oscillator strengths are demonstrated in Fig. 2.13. As expected, the exciton energy spectra are asymmetric with respect to the electric field direction [Fig. 2.13]. The Coulomb-induced anticrossing of the X-GS seen in the case of symmetric CQW is also observed here at approximately $F=16\,\text{kV/cm}$. The physical mechanism that causes this anticrossing is essentially the same as in the symmetric CQW, but the anticrossing takes place at much higher values of the electric field. This is because the electric field ($F=12.5\,\text{kV/cm}$) almost compensates the asymmetry in the conduction band structure as discussed above. As a result, at this value of field the properties of the asymmetric CQW can resemble those of the symmetric CQW at $F=0$. The same does not happen, however, at $F=-7.2\,\text{kV/cm}$ [Fig. 2.13(a)] when the asymmetry in the valence band is compensated. This is because the increasing electric field pushes the hole GS (h1) to the right well [Fig. 2.13(b)], while the GS electron (e1) resides all the time in the right well. Therefore, for $F<10\,\text{kV/cm}$ the X-GS is a direct exciton state which is dominated by the electron and hole GSs
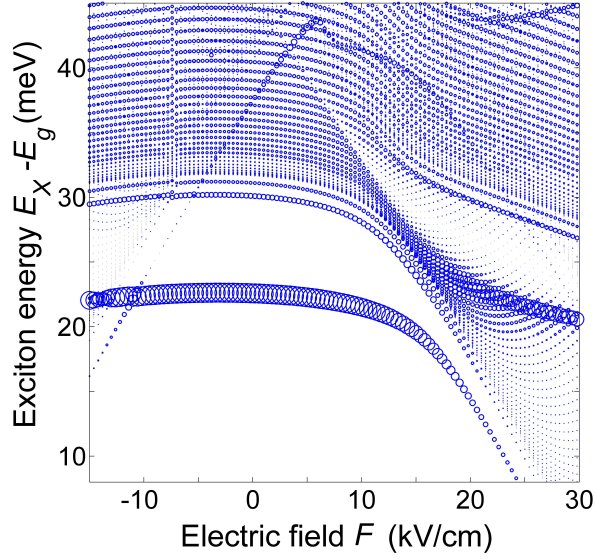
Figure 2.13: Exciton energies and oscillator strengths (circle area) in an asymmetric $In_{0.08}Ga_{0.92}As/GaAs/In_{0.1}Ga_{0.9}As$ (10-4-10-nm) CQW structure as functions of the applied electric field. The energy gap $E_g = 1.373\,eV$ for InGaAs QW layers.

sitting in the right well. This corresponds to the bright X-GS as seen in Fig. 2.13 and no D-I anticrossing is observed for $F<10\,kV/cm$. For the excited states in asymmetric CQW, there is no bright decoupled X-ES which is seen in symmetric CQW. This is a suitable condition for having tunable light-matter strong coupling because we can switch on/off the strong coupling by means of the electric field. If there is a decoupled X-ES, this state would always strongly couple to the cavity modes and mask all other effects of light-matter coupling. Therefore, such an asymmetric CQW is a good candidate for using in optoelectronics.

2.10   Exciton lifetime

A CQW exciton can escape from the system using the following two major channels. It can either recombine by emitting a photon or the electron and/or hole can tunnel through the external barrier with the help of the electric field. We concentrate here on the X-GS only and combining both channels together, the total exciton lifetime takes the form

$$\frac{1}{\tau} = \frac{1}{\tau_R} + \frac{1}{\tau_T}, \tag{2.37}$$
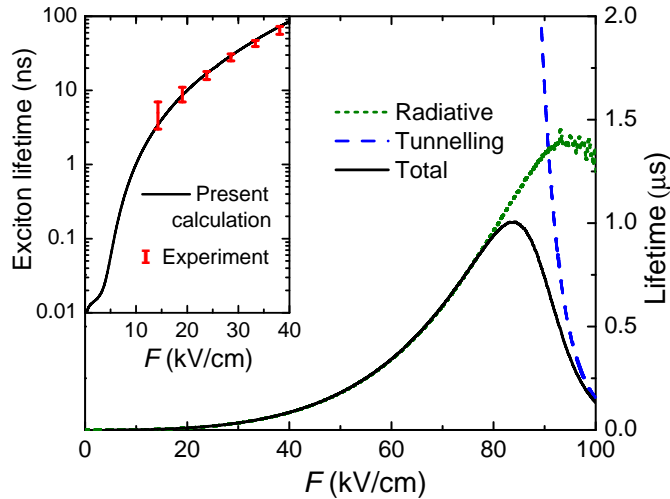
Figure 2.14: Radiative (dotted curve), tunneling (dashed curve), and total lifetimes (solid curve) of the exciton ground state X-GS as functions of the applied electric field. (Inset) Logarithmic plot of the X-GS total lifetime in comparison with measured photoluminescence decay times (error bars) extracted from Ref.[24].

where $\tau_R = \hbar/(2\Gamma_R)$ is the exciton radiative lifetime [77], τ_T is the tunneling lifetime. For the latter, we take into account the lowest pair state only, $\tau_T = \hbar/(\Gamma_1^e + \Gamma_1^h)$, where $\Gamma_1^{e(h)}$ is the imaginary part of the electron (hole) energy in Eq.(2.17). This approximation is valid because at large fields the X-GS is mainly dominated by $e1h1$ pair state. In the full range considered in Fig. 2.14, the exciton lifetime is strongly dominated by the radiative channel. The tunneling lifetime is much longer than the radiative one up to F=80 kV/cm. However, the probability of the electron and hole tunneling increases with the electric field. At some point the tunneling time becomes comparable to the radiative lifetime and then starts to dominate. The D-I crossover of the X-GS is accompanied by a monotonic growth of its radiative lifetime. Indeed, a direct exciton has a short lifetime because the carriers are in the same well, so that they can easily recombine. Increasing the e-h separation leads to a dramatic increase of the radiative lifetime. We have also compared the calculated radiative lifetime for the X-GS with the experimental results taken from Ref. [24]. The error bar were also taken from PL measurement. As demonstrated in the inset of Fig. 2.14, a quantitative agreement with the experimental results is achieved.

2.11 ABSORPTION SPECTRA

The exciton absorption coefficient in a 8–4–8 nm GaAs/Al$_{0.33}$Ga$_{0.67}$As CQW is calculated at different frequencies of the incoming light. Using the Lorentzian model of absorbing oscillators [75, 78] and leaving out a common prefactor, the absorption of the exciton with zero in-plane momentum takes the form

$$\alpha(\omega) = \sum_\nu \Gamma_{R,\nu} \frac{\Gamma_{R,\nu}}{(\hbar\omega - E_\nu)^2 + \Gamma_{R,\nu}^2} \,, \tag{2.38}$$

where ω is the frequency of the incoming light, the index ν labels all possible excitonic states calculated in the theory, and E_ν and $\Gamma_{R,\nu}$ stand for their energies and radiative linewidths.

The calculated absorption spectrum for the in-plane exciton confinement radius R=800 nm is demonstrated in Fig. 2.15. All lines in the absorption have very narrow radiative widths ($<$0.1 meV). Although the spectrum properly reproduces the linewidths, all lines have the same peak height, and the fact that not all of them are seen in Fig. 2.15(a) is only due to the resolution of the plot. To improve on this and also to take into account the effect of inhomogeneous line broadening which takes place in realistic CQW structures, we make a Gauss convolution of the spectrum [79]:

$$A(\omega) = \int_{-\infty}^{\infty} \alpha(\omega')g(\omega - \omega')d\omega' \,, \tag{2.39}$$

with a normalized Gauss function

$$g(\omega) = (\Delta\sqrt{\pi})^{-1}e^{-\omega^2/\Delta^2} \,, \tag{2.40}$$

where $2\sqrt{\ln 2}\Delta$ is the full width at half maximum (FWHM), in this calculation taken equal to 0.2 meV.

The convoluted spectra are shown in Fig. 2.15(b). All lines now have almost the same width but their peak maxima now reflect the optical strength of the corresponding exciton states. The two lowest excitonic states, X-GS and X-ES, are well resolved in the spectrum up to F=5 kV/cm. Then the X-GS becomes indirect and
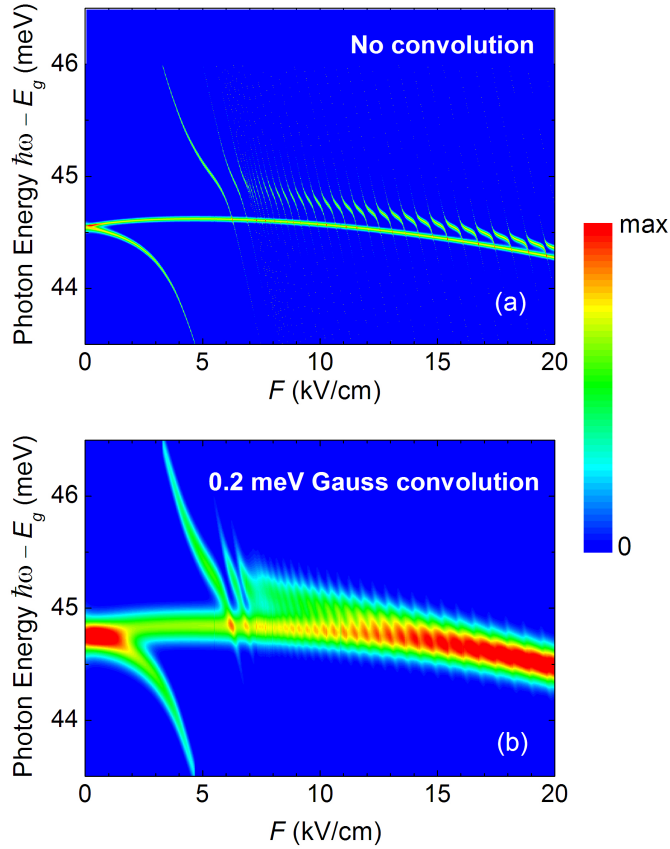
Figure 2.15: (a) Electric field dependence of the full excitonic absorption spectrum. (b) The same spectra convoluted with a Gaussian function with 0.2-meV full width at half maximum. The energy gap $E_g = 1.519\,\text{eV}$ for GaAs QW layers.

loses its optical activity. The bright direct X-ES line superimposes with higher ESs and discretized continuum of the indirect exciton, all lines merging up together at higher electric fields.

2.12 SUMMARY

In this chapter, an accurate calculation of the exciton ground and excited states in symmetric AlGaAs and asymmetric InGaAs CQWs in an applied electric field is presented. An efficient and straightforward algorithm of solving the Schrödinger equation in real space is developed. The energies and the wave functions of exciton in the presence of an electric field are calculated using the approach based on expanding the exciton wave function into uncorrelated e-h pair states. While we are able to calculate

a large number of exciton states, we have concentrated on two most important ones, the exciton ground state X-GS and the brightest excited state X-ES.

The oscillator strength, binding energy, Bohr radius, and linewidth of the X-GS and X-ES in symmetric CQW are studied. The Coulomb coupling between direct and indirect pair states leads to the direct-to-indirect crossover of the X-GS, while the properties of the X-ES remain almost unchanged. The results are also compared to a single-state basis calculation which takes into account the lowest $e1h1$ pair state only. The neglect of the higher e-h pair states in single-state basis calculation leads to results which are considerably different at low electric fields from the full calculation. This is, in particular, because the $e2h1$ ($n=3$) excited e-h pair state can have a significant contribution to the exciton state.

We have calculated the exciton lifetime which consists of two main components, radiative and tunneling times. It is shown that the excitonic lifetime is dominated by the radiative recombination at small values of the electric field. Tunneling processes dominate at larger fields. The total lifetime decreases with increasing the electric field. The field dependence of the absorption spectrum is also calculated. We make a Gauss convolution of the spectrum in order to include the inhomogeneous line broadening of realistic structures.

In asymmetric CQW, the electric field can compensate the asymmetry in the energy band structure. A formation of symmetric and antisymmetric states are seen at F=12.5 kV/cm for the electron and F=-7.2 kV/cm for the hole. As a result, the same physical mechanism as observed in symmetric CQW is responsible also for spectral properties of asymmetric CQW. The Coulomb-induced anticrossing of X-GS takes place there at approximately F=16 kV/cm which is around 4-5 kV/cm above the point (at F=12.5 kV/cm) where the CQW asymmetry is compensated by the applied electric field, similar to the results for symmetric CQWs. However, there is no decoupled bright X-ES in asymmetric CQW structures. This is a suitable condition for having a special type of voltage-tuned exciton polaritons, in the structures, which are considered in Chapter 3.

Chapter 3

Quantum well polaritons

In this chapter, we study the light-matter interaction in microcavity-embedded CQWs. The excitonic states calculated in the previous chapter are used here and the polariton effect is treated on the microscopic level. There is a certain difference in the fundamental concept of polaritons in confined systems as compared to that of bulk semiconductors. In bulk semiconductors, an exciton with a wavevector $\mathbf{k}$ can interact only with a photon with the same wavevector because of momentum conservation. In confined structures, the breaking of translational invariance along the growth direction results in the conservation of the in-plane wavevector $\mathbf{k}_{||}$ only. Therefore, an exciton can interact with photons with the same in-plane wavevector $\mathbf{k}_{||}$ but with all possible values of the wavevector in the z direction $\mathbf{k}_z$.

We concentrate on an asymmetric GaAs/InGaAs CQW structure embedded in a planar microcavity, which was described in Chapter 2. As discussed in the previous chapter, the asymmetry of the conduction band is compensated at a certain value of the electric field applied along z direction. When this happens, electrons tunneling through the barrier have symmetic and antisymmetric wave functions. This condition is called tunneling resonance. This electron is then bound together with a hole in the right well, producing the direct and indirect excitons. A direct exciton (DX) has a large oscillator strength, while an indirect exciton (IX) offers a large dipole moment. Embedding the asymmetric CQW in a microcavity, an exciton mode with both DX and IX components interacts with a cavity mode and produces a polariton state called

a dipolariton [61].

In this chapter, the polariton effect in the microcavity-embedded CQWs is treated based on the microscopic theory [75, 80] which was initially proposed and developed by K. Huang [81, 82]. In this theory, the material and Maxwell's equations are used to describe the microscopic excitonic polarization and the electromagnetic wave propagating in a microcavity [83]. The excitonic polarization and susceptibility are calculated for different values of the electric field. The electric field, reflectivity and absorption are calculated using the scattering matrix method [84, 85]. Finally, the contributions of DX, IX and cavity (C) modes to the polariton states are studied and the polariton states with large static dipole moment called dipolaritons [61, 62] are investigated in detail.

3.1 MAXWELL'S EQUATION IN A MEDIUM

In the framework of a semiclassical theory, the propagation of an electromagnetic wave in a medium is described by Maxwell's equations:

$$\nabla \times \mathbf{H} = \frac{1}{c}\frac{\partial \mathbf{D}}{\partial t} \tag{3.1}$$

$$\nabla \times \mathbf{E} = -\frac{1}{c}\frac{\partial \mathbf{B}}{\partial t} \tag{3.2}$$

$$\nabla \cdot \mathbf{B} = 0 \tag{3.3}$$

$$\nabla \cdot \mathbf{D} = 0\,, \tag{3.4}$$

with the magnetic field $\mathbf{B} = \mu\mathbf{H}$ and the electric displacement field $\mathbf{D} = \epsilon\mathbf{E}$, where μ is the permeability and ϵ is the permittivity of the medium. For the semiconductor material used in this calculation, we assume that there is no free charge density and μ=1. Taking the curl of Eq.(3.2) and substituting it to Eq.(3.1) gives

$$\nabla \times \nabla \times \mathbf{E} = -\frac{1}{c^2}\frac{\partial^2 \mathbf{D}}{\partial t^2}\,, \tag{3.5}$$

The equation can be simplified by noting that

$$\nabla \times \nabla \times \mathbf{E} = \nabla \cdot (\nabla \cdot \mathbf{E}) - \nabla^2 \mathbf{E}. \tag{3.6}$$

The displacement field is written as $\mathbf{D} = \mathbb{D}e^{-i\omega t}$ for a monochomatic wave and we have $\nabla \cdot \mathbf{D} = 0$. This brings Eq.(3.5) to the form

$$\nabla^2 \mathbf{E} = -\frac{\omega^2}{c^2} \mathbb{D}. \tag{3.7}$$

The polarization and displacement fields are related to the electric field by

$$\mathbf{P} = \chi \mathbf{E} \tag{3.8}$$

$$\mathbb{D} = \epsilon_b \mathbf{E} + 4\pi \mathbf{P}. \tag{3.9}$$

Then, Eq.(3.7) can be written as

$$\nabla^2 \mathbf{E} = -\frac{\omega^2}{c^2} \epsilon_b \mathbf{E} + 4\pi \mathbf{P} \tag{3.10}$$

$$= -\frac{\omega^2}{c^2} \epsilon_b \mathbf{E} + 4\pi \chi \mathbf{E}, \tag{3.11}$$

where ϵ_b is a background dielectric constant. In this chapter, we consider the planar layered structure with the s-polarized light only, so that the electric field has the form

$$\mathbf{E} = \hat{x}\, \mathcal{E}(z) e^{i\mathbf{K}\cdot\mathbf{R}_{xy}}, \tag{3.12}$$

where $\hat{x}$ is a unit vector in x direction, $\mathbf{K}$ is the in-plane wave vector and $\mathbf{R}_{xy}$ is the in-plane coordinate. To calculate the electric field $\mathcal{E}(z)$, we write it for each layer in the form

$$\mathcal{E}(z) = Ae^{ikz} + Be^{-ikz}, \tag{3.13}$$

where k is the wavevector in z direction and the coefficients A, B are calculated using the scattering matrix (Appendix A).

3.2 STRUCTURE AND PARAMETERS

We concentrate on an asymmetric microcavity-embedded CQW structure used in the experiment [61, 62]. It consists of four asymmetric InGaAs CQWs placed at the antinodes of the electromagnetic field inside a $5\lambda/2$ cavity sandwiched between 17 and 21 pairs of GaAs/AlAs distributed Bragg reflectors (Fig. 3.1). The asymmetric CQW inside the cavity contains two 10-nm $In_xGa_{1-x}As$ QW layers with the In content of 0.08 (left well) and 0.1 (right well) separated by a 4-nm GaAs barrier. The background dielectric constant for GaAs and AlAs are 12.5 and 9 respectively. Inside the microcavity, we have a special layer with CQW structure. We neglect the difference in ϵ_b in GaAs and InGaAs layers because these layers are thin. We used ϵ_b=12.5 for this CQW layer. The dielectric constant is then calculated from

$$\epsilon(\omega) = \epsilon_b + \Delta\epsilon_d(\omega)\,, \tag{3.14}$$

where $\Delta\epsilon_d(\omega)$ is the change of dielectric constant due to the effect of CQW calculated from the local susceptibility as explained in Appendix B. This dielectric function is used in the scattering matrix to calculate the reflectivity, absorption and electric field profiles. The result is shown in the following sections. The parameters for the InGaAs CQW used in the chapter are the same as used in Chapter 2. Also, the excitonic wavefunctions and their optical properties calculated in Chapter 2 are used here.
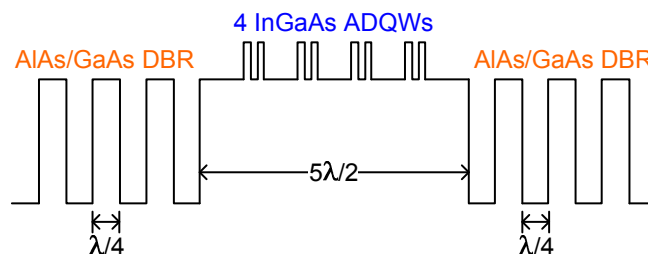
Figure 3.1: Schematic of a microcavity-embedded multiple-CQW structure consisting of a $5\lambda/2$ cavity sandwiched two distributed Bragg reflectors.

3.3 Reflectivity

From our excitonic calculation, we are able to compute a large number of exciton states as shown in Fig. 3.2. However, only three exciton states, namely the exciton ground state (X-GS) and two excited states DX(1s, 2s), which have considerable oscillator strength are shown in Fig. 3.3. These three exciton states show the strong coupling to the cavity mode. Figure 3.3 shows the reflectivity spectra for two different positions of the bare cavity mode (dashed vertical lines), creating different detunings to the bare exciton modes (red circles: the circle area is proportional to the oscillator strength of exciton). The polariton state are seen as dips in the reflectivity spectra. In Fig. 3.3(a), at low electric field (EF) the cavity mode locates at around 6 meV below X-GS. Due to a large oscillator strength of the X-GS, the exciton-light strong coupling can be achieved and the polariton states exhibit the anticrossing at approximately $F=19$ kV/cm. As the EF increases, the cavity mode turns out to be weakly coupled to the exciton modes because of a smaller oscillator strength. This on/off switching of the strong coupling regime is also observed in Fig. 3.3(b). In this case, the cavity mode is at approximately 1.3959 eV and can be tuned to the exciton
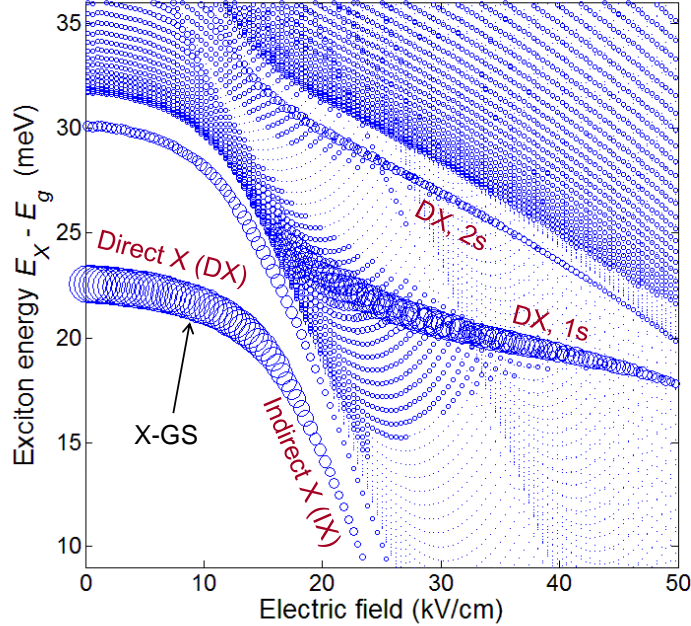
Figure 3.2: Exciton energies and oscillator strength (circle area) in the asymmetric 10-4-10-nm InGaAs CQW as function of the electric field.
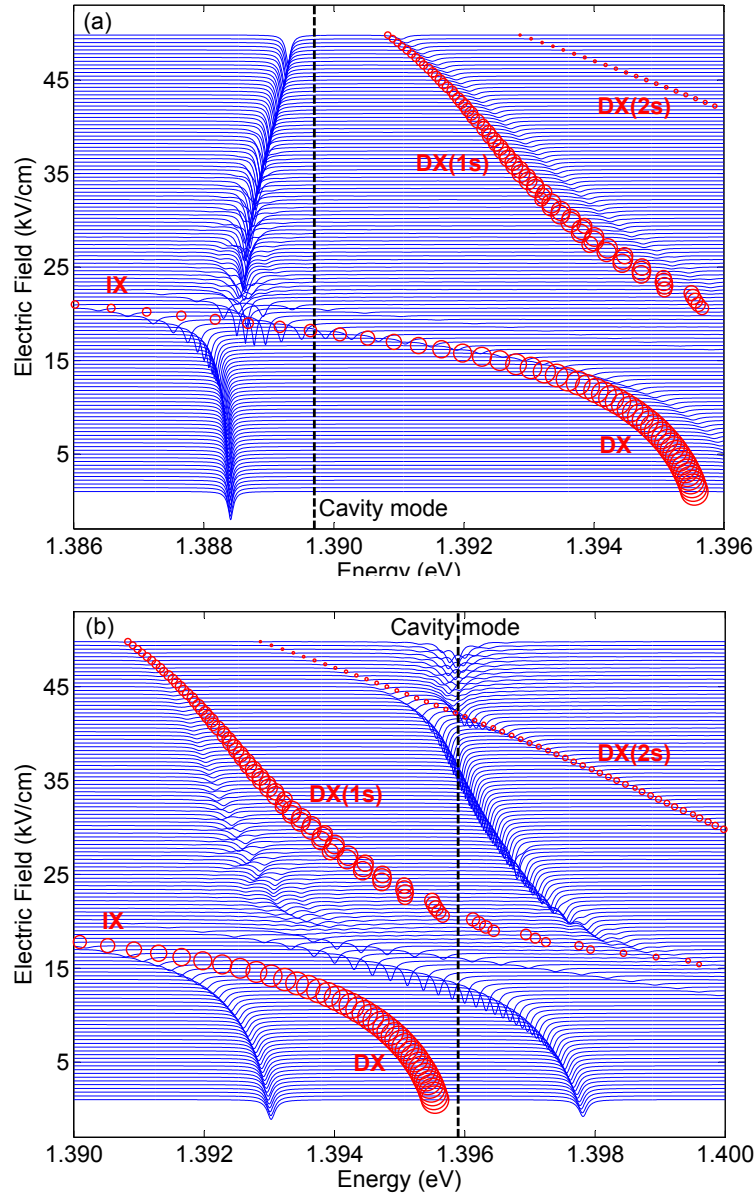
Figure 3.3: Field dependent reflectivity spectra of the asymmetric 10-4-10-nm InGaAs CQW structure, with the bare cavity mode at (a) 1.3897 eV and (b) 1.3959 eV (black dashed lines). Exciton ground state exhibiting DX-IX transition and two brightest direct exciton (DX) 1s and 2s states located far in the excitonic continuum are shown by open red circles.

modes by changing the EF. The small detuning enhances the exciton-light coupling as can be seen from the large energy separation of the two polariton states at low EFs. At higher EFs, the two clear anticrossings of the polariton states formed by the cavity mode and bright DX(1s, 2s) are observed.

3.4 Absorption and comparison with experimental data

We have also calculated the absorption spectra as demonstrated in Fig. 3.4. We make a 2-meV(FWHM) Gauss convolution of the excitonic induced susceptibility in order to include the effect of inhomogeneous broadening of the exciton lines [79],

$$\tilde{\chi}(\omega) = \int_{-\infty}^{\infty} \chi(\omega')g(\omega - \omega')d\omega' \,. \tag{3.15}$$

The model can be used to calculate the absorption for any incident angles of light. In this work, we have chosen two different cases: (i) normal incidence (θ=0) and (ii) non-normal incidence (θ=35° to the normal), in order to compare our theoretical results with the measurement of Ref. [61]. For normal incidence [Fig. 3.4(a)], the cavity mode manifests itself as a narrow peak in the absorption because it is weakly coupled to the X-GS. The polariton states at higher energies are strongly dominated by the DX excited states. At θ=35°, the cavity mode is blue-shifted to 1.402 eV and coupled to both the X-GS and the bright DX excited states, giving rise to the three distinct polariton states which are combinations of the cavity and exciton modes. Figure 3.4(c)-3.4(d) show the experimental photoluminescence spectra of a InGaAs CQWs microcavity taken from Ref. [61]. Note that the energy range shown in Fig. 3.4(a),(b) for the theory and Fig. 3.4(c),(d) for the experiment is the same but has a shift of 30 meV. This is because the energy gap used in the calculation is different from the experimental value. However, this difference does not affect at all the shape of the spectra, or varying the energy gap leads to a rigid energy shift of the whole spectrum only. It is found that the calculated results are in a quantitative agreement with the experiment.
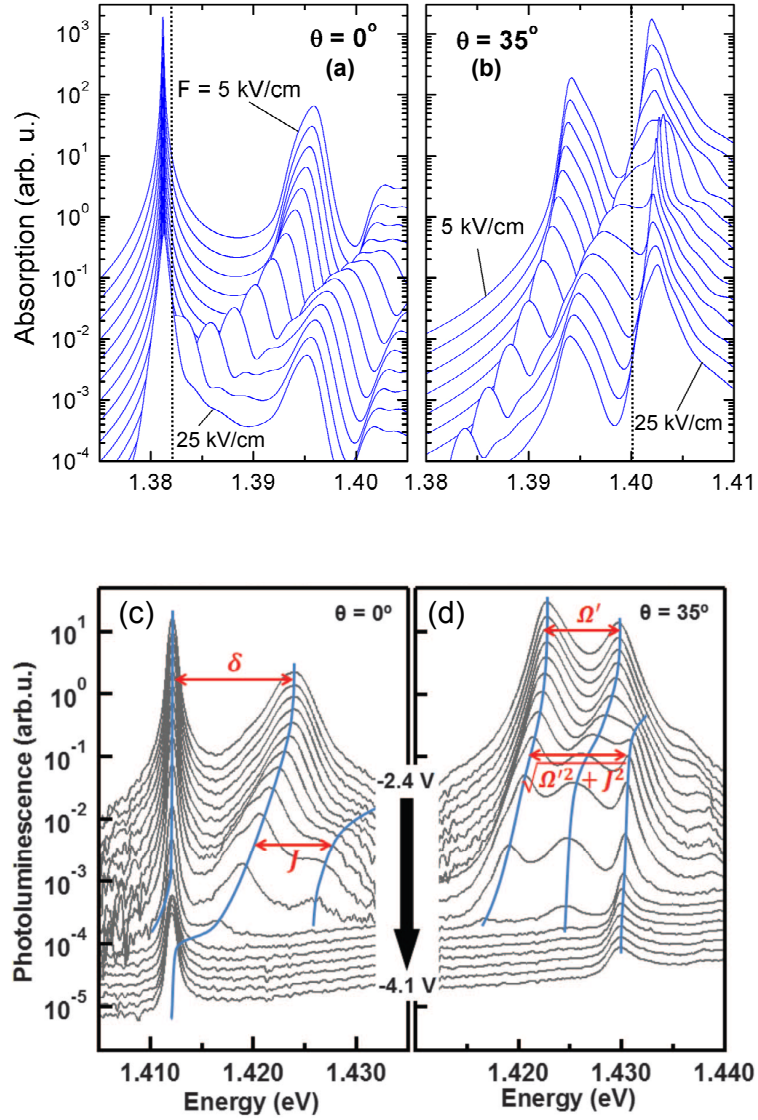
Figure 3.4: Field absorption spectra of the asymmetric 10-4-10-nm InGaAs CQW structure, (a) for normal incidence with bare cavity mode at $1.3820\,\mathrm{eV}$ (black dashed line) and (b) for incident angle of $\theta = 35°$ with the bare cavity mode at $1.4025\,\mathrm{eV}$. (c)-(d) show the photoluminescence spectra taken from Ref.[61] for $\theta = 0°$ and $\theta = 35°$ in the same range of the electric field.
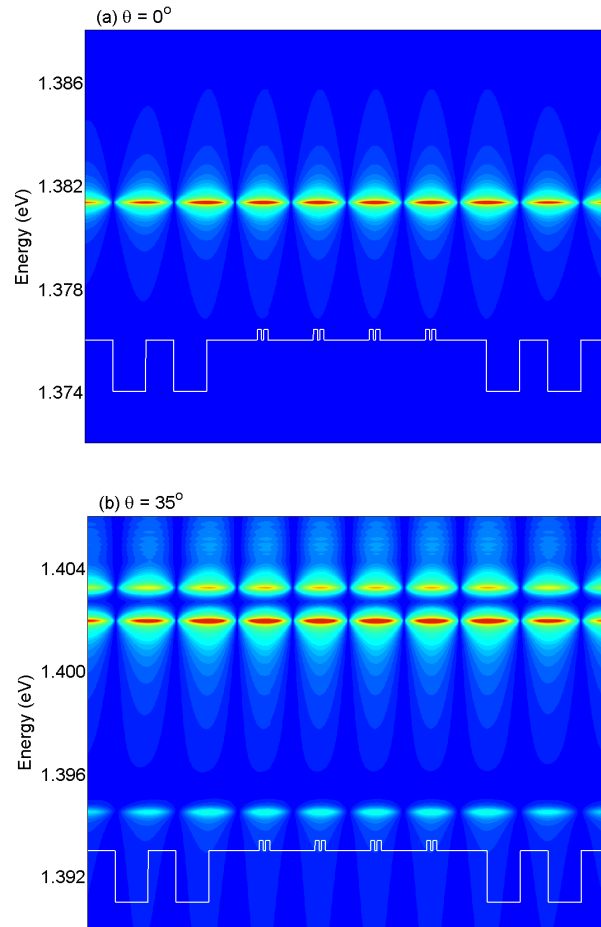
Figure 3.5: Electric field profile of the asymmetric 10-4-10-nm InGaAs CQW structure for (a) $\theta = 0°$ and (b) $\theta = 35°$ at $F=5\,\text{kV/cm}$, without Gauss convolution.

The electric field $\mathcal{E}(k, z)$ at $F{=}5\,\text{kV/cm}$ for $\theta{=}0$ and $\theta{=}35°$ calculated using the scattering matrix method are shown in Fig. 3.5. The electric field profile has a maximum at the energies of the polariton states. There is only one peak seen in the case of normal incidence which corresponds to the lowest polariton state as shown in Fig. 3.4(a), while the three polariton states for the incident angle of $\theta{=}35°$ are clearly demonstrated at approximately 1.394, 1.402 and 1.403 eV.

3.5 DIPOLARITONS

A dipolariton is a special type of polariton states which exhibits a large oscillator strength of DX and at the same time has a large dipole moment of IX since it is formed from a mixed DX-IX mode coupled to the cavity mode. The DX is strongly coupled to the cavity mode due to its large oscillator strength, while IX has a large static dipole moment but is weakly coupled to the cavity mode. However, it is electronically coupled to DX via the tunneling which is controlled by means of the electric field. The main purpose of this section is to study the properties of the dipolaritons on the microscopic level, by calculating the relative contribution of DX, IX and C modes to the polariton states.

3.5.1 MICROSCOPIC POLARIZATION

For CQW microcavities, the microscopic polarization $Y(\mathbf{r}, \mathbf{R})$ can be written as

$$Y(z_e, z_h, \rho; \mathbf{R}_{xy}) = e^{i\mathbf{K}\cdot\mathbf{R}_{xy}} e d_{cv} \sum_{\nu} \frac{\psi_\nu(z_e, z_h, \rho) X_\nu(k, \omega)}{E_\nu + \frac{\hbar^2 K^2}{2M} - \hbar\omega - i\gamma}, \qquad (3.16)$$

where the index ν denotes the ν-th exciton state, E_ν is the exciton transition energy, $K = |\mathbf{K}|$ is the in-plane wavevector, $\mathbf{R}_{xy}$ is the in-plane coordinate, ω is the light frequency, γ is the phenomenological parameter and

$$X_\nu(k, \omega) = \int \mathcal{E}(k, z)\psi_\nu(z, z, 0)dz\,. \qquad (3.17)$$

The calculation of $X_\nu(k, \omega)$ is shown in Appendix C. The electric field $\mathcal{E}(k, z)$ is the solution of the Maxwell's equation including the excitonic polarization. We then

introduce three functions of frequency related to the microscopic polarization,

$$\mathcal{F}(\omega) = \left| \int \mathcal{Y}(z, z, 0) dz \right|^2 \tag{3.18}$$

$$\mathcal{D}(\omega) = \int \int \int |\mathcal{Y}(z_e, z_h, \rho)|^2 (z_e - z_h) 2\pi \rho d\rho \, dz_e \, dz_h \tag{3.19}$$

$$\mathcal{N}(\omega) = \int \int \int |\mathcal{Y}(z_e, z_h, \rho)|^2 \, 2\pi \rho d\rho \, dz_e \, dz_h \,, \tag{3.20}$$

where

$$\mathcal{Y}(z_e, z_h, \rho) = ed_{cv} \sum_\nu \frac{\psi_\nu(z_e, z_h, \rho) X_\nu(k, \omega)}{E_\nu + \frac{\hbar^2 K^2}{2M} - \hbar\omega - i\gamma} \,. \tag{3.21}$$

Functions $\mathcal{F}, \mathcal{D}, \mathcal{N}$ are proportional to the polariton brightness, polariton static dipole moment and the normalization constant, respectively.

3.5.2 TWO-LEVEL MODEL AND CAVITY-MODE FRACTION

In the two-level model of the polariton, the exciton mode (X) with energy of ω_X is coupled to the cavity mode (C) with energy of ω_C via the coupling constant V. The set of two coupled equations has the form

$$(\omega_C - \omega)C - VX = 0 \tag{3.22}$$

$$(\omega_X - \omega)X - VC = 0 \,, \tag{3.23}$$

or in matrix form,

$$\begin{pmatrix} \omega_C & -V \\ -V & \omega_X \end{pmatrix} \begin{pmatrix} C \\ X \end{pmatrix} = \omega \begin{pmatrix} C \\ X. \end{pmatrix} \tag{3.24}$$

The secular equation for the polariton frequency then takes the form

$$V^2 = (\omega_C - \omega)(\omega_X - \omega) \,, \tag{3.25}$$

and the ratio X/C is given by

$$\frac{X}{C} = \frac{V}{\omega_X - \omega} \,, \tag{3.26}$$

with the normalization condition $X^2 + C^2 = 1$.

In our excitonic calculation, we have a large number of exciton states. To compare our microscopic approach with the two-level model, we consider that only a single state is coupled to a cavity. The electric field in a thin QW layer is assumed to be constant $\mathcal{E}(z) \approx \mathcal{E}(z_0)$. The excitonic polarization in Eq.(B.14) then has the form

$$P = \mathcal{E}(z_0)e^2 d_{cv}^2 \frac{\psi(z,z,0)A}{\omega_X - \omega}, \tag{3.27}$$

or

$$(\omega_X - \omega)P = \mathcal{E}(z_0)e^2 d_{cv}^2 \psi(z,z,0)A, \tag{3.28}$$

where z_0 is some point within the CQW structure and $A = \int \psi(z', z', 0)dz'$. The Maxwell's equation for $K{=}0$ has the form

$$-\frac{d^2\mathcal{E}(z)}{dz^2} = \frac{\omega^2}{c^2}\left[\epsilon_b(z)\mathcal{E}(z) + 4\pi P(z)\right]. \tag{3.29}$$

Neglecting any change of the electric field $\mathcal{E}(z)$ within the CQW and applying the cavity-mode approximation, we obtain:

$$\frac{d^2\mathcal{E}}{dz^2} = -\frac{\omega_C^2}{c^2}\epsilon_b\mathcal{E}, \quad \text{for } z \approx z_0, \tag{3.30}$$

Then, we get

$$(\omega_C^2 - \omega^2)\mathcal{E} = \omega^2 \frac{4\pi}{\epsilon_b}P. \tag{3.31}$$

Assuming that $|\omega - \omega_C| \ll \omega_C$, we obtain $\omega_C \approx \omega$ and $(\omega_C^2 - \omega^2) \approx 2\omega_C(\omega_C - \omega)$. Then Eq.(3.31) can be rewritten as

$$(\omega_C - \omega)\mathcal{E} = \omega_C \frac{2\pi}{\epsilon_b}P. \tag{3.32}$$

Introducing the length $a = \int P(z)dz/P_{max}$, we can rewrite Eq.(3.28) and Eq.(3.32) as a set of two coupled equations

$$(\omega_C - \omega)\mathcal{E} = \omega_C \frac{2\pi}{\epsilon_b}P_{max} \tag{3.33}$$

$$(\omega_X - \omega)P_{max}a = e^2 d_{cv}^2 f^2 \mathcal{E}. \tag{3.34}$$

By comparing with the two-level model, we get

$$V^2 = (\omega_C - \omega)(\omega_X - \omega) \quad = \quad \frac{2\pi\omega_C e^2 d_{cv}^2 f^2}{\epsilon_b a} \,, \tag{3.35}$$

and thus the ratio

$$\left(\frac{C_X}{C_C}\right)^2 = \frac{2\pi\omega_C a}{\epsilon_b e^2 d_{cv}^2 f^2} \left(\frac{P_{max}}{\mathcal{E}}\right)^2 \,. \tag{3.36}$$

When we replace aP_{max} by $\int P(z)dz$, this leads to very minor changes. Within the single-state approximation, the functions $\mathcal{F}$ in Eq.(3.18) and function $\mathcal{N}$ in Eq.(3.20) take the form

$$\mathcal{F}(\omega) \;=\; |\mathcal{E}(z_0)|^2 \frac{f^4}{(\omega_X - \omega)^2} \tag{3.37}$$

$$\mathcal{N}(\omega) \;=\; |\mathcal{E}(z_0)|^2 \frac{f^2}{(\omega_X - \omega)^2} \,, \tag{3.38}$$

Therefore, the ratio between $\mathcal{F}$ and $\mathcal{N}$ is related to the exciton oscillator strength. Replacing $\mathcal{F}/\mathcal{N} = f^2$ brings Eq.(3.36) to the form

$$\left(\frac{C_X}{C_C}\right)^2 = \frac{2\pi\omega_C}{\epsilon_b e^2 d_{cv}^2 \mathcal{E}^2} \frac{\mathcal{N}}{\mathcal{F}} \left| \int P(z)dz \right|^2 \,. \tag{3.39}$$

$\mathcal{F}, \mathcal{N}$ are calculated as function of energy, their values at the polariton energy are taken in order to compute the ratio (C_X/C_C) in the polariton state.

3.5.3 STATIC DIPOLE MOMENT AND INDIRECT EXCITON FRACTION

An exciton mode consists of the direct (DX) and indirect (IX) components, their coefficients satisfy the condition $C_X^2 = C_{DX}^2 + C_{IX}^2$. The C_{IX} is proportional to the polariton dipole moment. If the IX component is dominant, the polariton dipole moment is large due to a large e-h separation in the system. Therefore, we can determine the ratio between C_{IX} and C_X contributions from

$$\left(\frac{C_{IX}}{C_X}\right)^2 = \frac{1}{d}\frac{\mathcal{D}}{\mathcal{N}} \,, \tag{3.40}$$

where d is the exciton dipole moment length. Similar to Eq.(3.39), the values of $\mathcal{D}$ and $\mathcal{N}$ are taken at the polariton energy.

From the ratio $(C_\mathrm{X}/C_\mathrm{C})$ and $(C_\mathrm{IX}/C_\mathrm{X})$, we can calculate the DX, IX and C fractions by applying the two normalization conditions

$$C_{\mathrm{DX}_n}^2 + C_{\mathrm{IX}_n}^2 + C_{\mathrm{C}_n}^2 \;=\; 1 \tag{3.41}$$

$$\sum_n C_{\mathrm{C}_n}^2 \;=\; 1\,, \tag{3.42}$$

where n is used to label different polariton states. The second condition [Eq.(3.42)] is an extra condition to verify the results and also to introduce some corrections. To satisfy the second condition, meaning that the total contribution of the cavity mode to all polariton states must be 1, we need to introduce an extra parameter κ in Eq.(3.39) as

$$\left(\frac{C_{\mathrm{X}_n}}{C_{\mathrm{C}_n}}\right)^2 \;=\; \beta_n \kappa \tag{3.43}$$

$$\beta_n \;=\; \frac{2\pi\omega_C \left|\int P(z)dz\right|^2}{\epsilon_b e^2 d_{cv}^2 E^2}\frac{\mathcal{N}}{\mathcal{F}}\,. \tag{3.44}$$

Substituting Eq.(3.43) into Eq.(3.41), we obtain

$$C_{\mathrm{C}_n}^2 = \frac{1}{1+\beta_n\kappa}\,. \tag{3.45}$$

The value of κ is calculated using the second condition [Eq.(3.42)] as

$$\sum_n C_{\mathrm{C}_n}^2 = \sum_n \frac{1}{1+\beta_n\kappa} = 1\,. \tag{3.46}$$

For the studied structure, it is found that $\kappa \approx 1$ as it should be, telling us that our estimates are good enough. Depending on the electric field gamma can vary between 0.2 to 1.5, but taking the gamma into account leads in practice to an insignificant correction of the fraction calculation.

3.5.4 Analysis of polariton modes

Figure 3.6 shows the absorption spectra without the Gauss convolution in the case of non-normal incidence at $\theta=35°$. For the following results, we use the inplane exciton confinement radius of $200\,\text{nm}$ in order to reduce the number of states in the continuum. The polariton states (black lines in Fig. 3.6) are indicated by the peak positions in the absorption.

The fractions of DX, IX and C modes for the lowest *six* polariton states ($n=1$ to $n=6$) are shown in Fig. 3.7. For the state $n=1$, the DX component strongly dominates at low EFs and then decreases when the X-GS switches from DX to IX, corresponding to the increase of IX component. The cavity mode has a small contribution to this polariton state. The cavity mode has a major contribution to state $n=2$ at low electric field because the detuning is very small. Considering states $n=2$ and $n=3$, polaritons are formed from the coupling between the cavity mode and the second and third exciton excited states. The cavity mode is in resonance with the exciton mode at
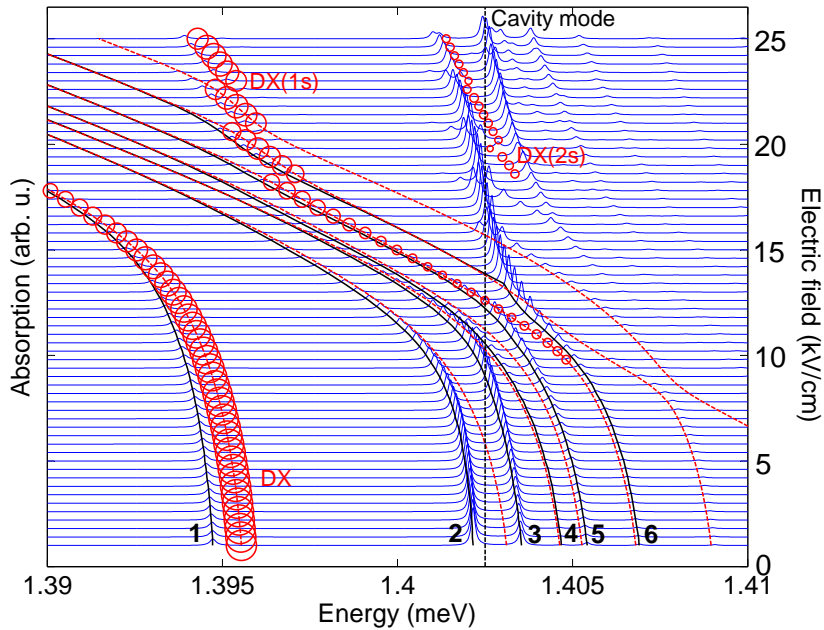
Figure 3.6: Field absorption spectra of the asymmetric 10-4-10-nm InGaAs CQW structure at $\theta = 35°$ with the bare cavity mode at $1.4025\,\text{eV}$ (black dashed line). The polariton states (blue lines with symbols) are indicated by the peak position of the absorption. The red dashed lines denote the bare exciton modes.
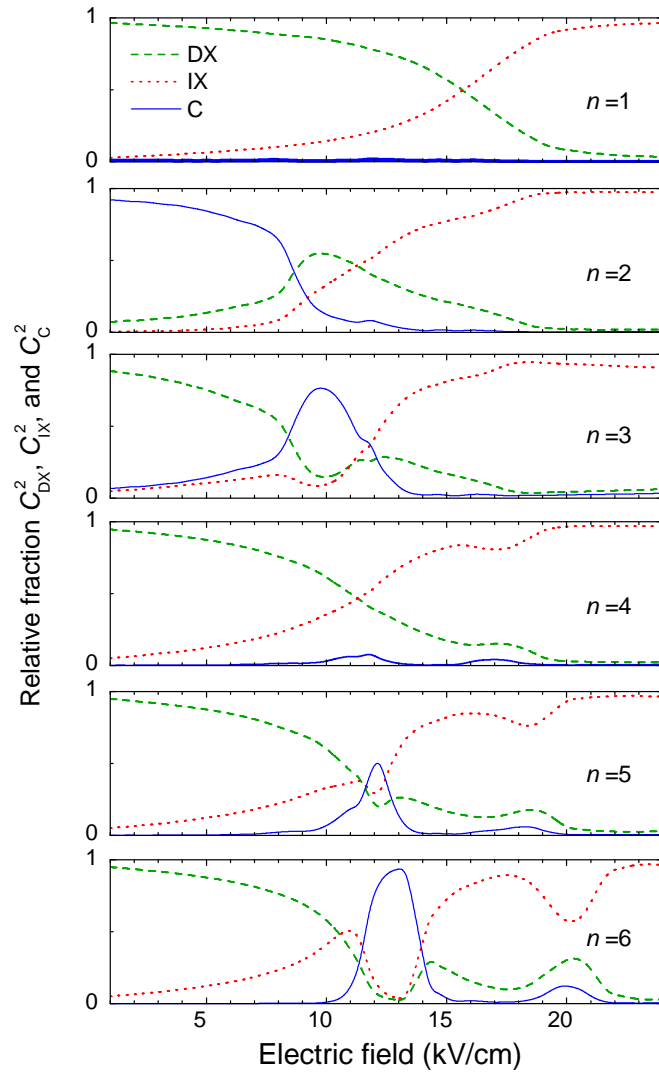
Figure 3.7: Fraction of DX, IX and C modes for the polariton states $n=1$ to $n=6$ as function of electric field.

around $F{=}9\,\text{kV/cm}$, leading to the considerable change in the exciton and photon fractions at around this value of the electric field. The C fraction decreases in the state $n{=}2$ and at the same time increases in the state $n{=}3$, and vice versa for the DX component. The behaviour found for the state $n{=}3$ is also seen in higher states, but the peak of C component is found at higher values of the electric filed where the cavity mode is met by the exciton. However, the exciton-light coupling is very weak in the state $n{=}4$ due to a small oscillator strength of exciton, resulting in the absence of the C component for all electric fields. For the state $n{=}5$ at around $F{=}12\,\text{kV/cm}$, the coupling increases because the cavity mode is in resonance with the DX(1s) which has considerable oscillator strength. As can be seen in Fig. 3.7, at this value of electric field all three components have comparable contribution. It seems that this is the maximum effect of dipolariton which can be observed in our calculation. Increasing IX further inevitably decreases C as DX decreases. For the state $n{=}6$ at $F{=}12.5\,\text{kV/cm}$, the major contribution is C with small DX and IX. A slight increse of DX fraction at around $F{=}20\,\text{kV/cm}$ comes from the influence of the DX(1s) state. At large electric fields, all polariton states are strongly dominated by IX component only (i.e. zero DX component). As seen from our calculation, there are no mixed states with C and IX components, namely a dark polariton, which was reported in Ref. [61]. This can be explained from the fact that the exciton-photon coupling is proportional to the exciton oscillator strength, so that a very small oscillator strength of IX exciton leads to a very weak coupling between IX and C modes. As can be seen in Fig. 3.7, the C fraction is almost zero if there is no DX contribution to the polariton state and only the IX component is dominant. Therefore, the polariton state with mixed IX-C component with no contribution from DX does not exist in this system.

3.6 SUMMARY

In this chapter, the interaction between exciton and photon in an asymmetric microcavity-embedded CQW is studied by solving coupled material and Maxwell's equations. All excitonic states and their properties calculated in Chapter 2 are taken into account in this polariton calculation. The structure consists of four asymmetric

CQW inside the cavity, similar to the structure used in the experiment [61]. The dielectric constant and local susceptibility of the CQW layers inside the cavity is determined and then used in a scattering matrix method in order to calculate the reflectivity and absorption spectra. In the strong coupling regime, the anticrossing of two polariton states is clearly seen. The strong coupling between exciton and cavity modes can be switched on/off by the means of the electric field. At the incident angle of light of $\theta = 35°$, the cavity mode is strongly coupled to the exciton states at different electric fields, showing three distinct polariton states. The calculated result is in a good agreement with the measurement [61].

In the three-level system (DX, IX and C), DX is strongly coupled to C because it has a large oscillator strength. IX has a weak coupling to C, but it is electronically coupled to DX via the tunneling through the barrier. The mixed polariton state of such a three-level system is called dipolariton. It shares a large oscillator strength of DX and a large electric dipole moment of IX. In this section, the contributions of DX, IX and C to the six lowest polariton states are calculated using the microscopic theory. To analyze the properties of dipolaritons, we have also calculated the DX, IX and C fractions of the polariton states using the microscopic theory. The three functions $\mathcal{F}$, $\mathcal{D}$, and $\mathcal{N}$ are determined from the excitonic microscopic polarization. The polariton state $n=5$ has a maximum effect of dipolariton at $F=12\,\mathrm{kV/cm}$. All three components have comparable contributions to the polariton state. It is also found that there is no mixed state having comparable C and IX components and negligible DX component, namely dark polariton as reported in Ref. [61]. This is because the cavity mode is weakly coupled to the indirect excitons due to their small oscillator strength.

Chapter 4

Polaritons in quantum dot-microcavity systems

The main purpose of this chapter is to study the light-matter interaction in a strongly-coupled QD-cavity system. An exciton mode is coupled to the cavity mode, producing two polariton modes with different eigenenergies. In the strong coupling regime, the anticrossing of two polariton modes is observed when the exciton mode is resonant to the cavity mode. The energy splitting (Ω) is proportional to the coupling strength g, $\Omega = 2g$. The model used in this chapter is different from the model explained in Chapter 3 because the excitonic part is treated as a two-level (fermionic) system. Here, the dynamics of exciton-polariton in the system is described by the Jaynes-Cummings (JC) ladder. The concept of four wave mixing (FWM) is also explained. The *spectrally* and *time - resolved* FWM signal is calculated for different temperatures. The coherent coupling is studied by Fourier-transforming the FWM signal into the two dimensional (2D) frequency domain. The phase correction of the 2D FWM is also calculated in order to compare the obtained results with the experiment.

4.1   JAYNES-CUMMINGS LADDER

In the system of a single fermionic two-level system strongly coupled to a single bosonic photon mode, the light - matter interaction is described within the JC model

[86]. The JC Hamiltonian is written as (we use $\hbar = 1$ for simplicity of notations)

$$H = \omega_C a^\dagger a + \omega_X |1\rangle \langle 1| + g \left(a^\dagger |0\rangle \langle 1| + a |1\rangle \langle 0| \right). \tag{4.1}$$

where ω_C (ω_X) is the cavity (exciton) transition frequency and g is the exciton-photon coupling strength. The detuning (δ) is defined as the energy difference between the exciton and cavity modes, $\delta = \omega_C - \omega_X$ The operator $a^\dagger$ and a are the cavity creation and annihilation operators, while $|0\rangle$ and $|1\rangle$ denote the ground (no exciton) and excited (one exciton) states of the excitonic subsystem. If we consider the first rung of the JC ladder (see $M_{1\pm}$ in Fig. 4.1), the two uncoupled states consist of a state with an exciton in the ground state and one photon $|0, 1\rangle$ and a state with an exciton in its excited state and no photon $|1, 0\rangle$. The system is considered as two-level system with the coupling strength g between the levels. When the cavity mode is tuned to the exciton mode ($\omega_C = \omega_X$), the symmetric $|M_{1+}\rangle$ and antisymmetric $|M_{1-}\rangle$ eigenstates are formed by the superpositon of the uncoupled states as

$$
\begin{aligned}
|M_{1+}\rangle &= \frac{1}{\sqrt{2}}(|0, 1\rangle + |1, 0\rangle); \\
|M_{1-}\rangle &= \frac{1}{\sqrt{2}}(|0, 1\rangle - |1, 0\rangle).
\end{aligned}
\tag{4.2}
$$

The Hamiltonian Eq.(4.1) can be rewritten in the matrix form

$$H = \begin{pmatrix} \omega_C & g \\ g & \omega_X \end{pmatrix} \tag{4.3}$$

with the eigenenergies ($\lambda_{1\pm}$)

$$\lambda_{1\pm} = \frac{\omega_C + \omega_X}{2} \pm \sqrt{\left(\frac{\omega_C - \omega_X}{2} \right)^2 + g^2}. \tag{4.4}$$

Therefore, the energy splitting of the two eigenstates at resonance ($\omega_C = \omega_X$) is given by $\lambda_{1+} - \lambda_{1-} = 2g$ which is equal to the Rabi splitting (Ω). The two possible transitions between the ground state (GS) and the first rung results in the Rabi
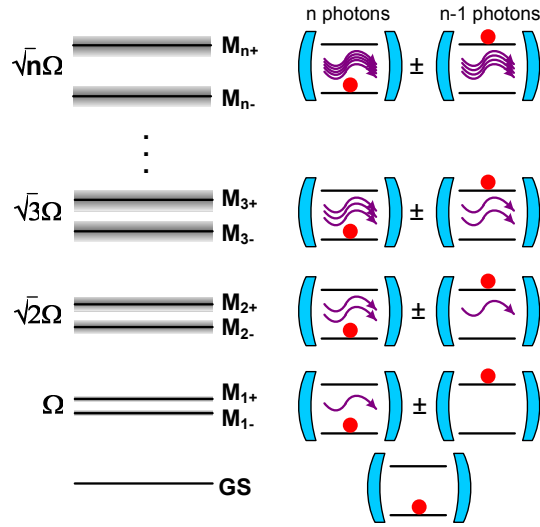
Figure 4.1: Level schematic of polariton states in the JC ladder.

doublet. Similar to the first rung, the eigenstates of the n-th rung are written as

$$
\begin{aligned}
|M_{n+}\rangle &= \frac{1}{\sqrt{2}}(|0, n\rangle + |1, n - 1\rangle); \\
|M_{n-}\rangle &= \frac{1}{\sqrt{2}}(|0, n\rangle - |1, n - 1\rangle),
\end{aligned}
\tag{4.5}
$$

with the eigenenergy

$$
\lambda_{n\pm} = \frac{(2n - 1)\omega_C + \omega_X}{2} \pm \sqrt{\left(\frac{\omega_C - \omega_X}{2}\right)^2 + ng^2}.
\tag{4.6}
$$

The $|0, n\rangle$ state denotes the state with unexcited exciton and n photons, while $|1, n - 1\rangle$ state has an exciton in the excited state and $n - 1$ photons. For higher rungs $(n > 1)$, the energy splitting between the two eigenstates increases as the square root of the number of photon, $\sqrt{n}\Omega$ for zero detuning. There are four possible transitions between the $(n\text{-}1)$-th rung and n-th rung which form a quadruplet. For high photon occupation number, the two middle transitions in the quadruplet are almost degenerate and form a single peak at the middle of the spectrum, surrounded by two other transitions, known in the literature as the Mollow triplet [87, 88].

76

4.2 FOUR-WAVE MIXING AND MEASUREMENT OF CO-HERENT DYNAMICS

The four wave mixing (FWM) is a nonlinear technique which uses two or more waves propagating together and interacting with a nonlinear medium [89, 90]. For the electromagnetic wave with amplitude $\mathcal{E}$, wavevector $\mathbf{k}$ and frequency ω propagating in free space, the electric field satisfying Maxwell's equations has the form

$$\mathbf{E}(\mathbf{r}, t) = \mathcal{E} e^{i(\mathbf{k}\cdot\mathbf{r}-\omega t)} \,. \tag{4.7}$$

The macroscopic polarization induced by such a field is given by

$$P(\mathbf{r}, t) = \int \chi(\mathbf{r} - \mathbf{r}', t)\mathbf{E}(\mathbf{r}', t)d\mathbf{r}' \,, \tag{4.8}$$

where $\chi(\mathbf{r} - \mathbf{r}', t)$ is a nonlocal susceptibility. The simplest version of the FWM spectroscopy used in experiments is the two-beam degenerate FWM consisting of two ultrashort laser pulse fields $(\mathcal{E}_1, \mathcal{E}_2)$ with a delay time τ between them. The field has the form

$$E(\mathbf{r}, t) = E_1(\mathbf{r}_1, t) + E_2(\mathbf{r}_2, t - \tau) \,. \tag{4.9}$$

The first pulse $\mathcal{E}_1$ with the wavevector k_1 induces the first-order polarization in the sample. The second pulse $\mathcal{E}_2$ with the wavevector k_2 arrives at the sample after the delay time τ. If the delay time τ is smaller than the dephasing time of the polarization, an interference grating along the phase direction $\mathbf{k}_2 - \mathbf{k}_1$ is produced. A fraction of $\mathcal{E}_2$ can be self-diffracted by the grating into the direction $\mathbf{k}_2 - \mathbf{k}_1 + \mathbf{k}_2 = 2\mathbf{k}_2 - \mathbf{k}_1$, giving rise to the third-order polarization $P^{(3)}$ called the FWM field which has the form.

$$P_{\text{FWM}}^{(3)}(\mathbf{r}, t) \propto \mathcal{E}_1^* \mathcal{E}_2^2 \exp\left\{i[(2k_2 - k_1)r + (2\omega_2 - \omega_1)t]\right\} \,. \tag{4.10}$$

In this work, the calculated FWM signal is compared with the experimental FWM response measured by the heterodyne spectral interferometry (HSI) technique [91]. In the studied HSI experiment, the two ultrashort pulses $\mathcal{E}_1$ and $\mathcal{E}_2$ of 1 ps duration are used to excite the fundamental cavity mode. In our model, the density

matrix can be calculated for all components. However, we consider in this work only the third-order component of the density matrix which produces the FWM signal at frequency $2\omega_2 - \omega_1$, the same as measured in HSI experiment at low intensities.

4.3   THE TAVIS-CUMMINGS MODEL AND FWM THEORY

The Hamiltonian which describes a photon mode coupled to N two-level systems has the form (setting $\hbar$=1 for simplicity of notations)

$$H = \omega_C a^\dagger a + \sum_{n=1}^{N} \left[\omega_{X_n} |n\rangle \langle n| + g_n \left(a^\dagger |0\rangle \langle n| + a |n\rangle \langle 0| \right) \right], \qquad (4.11)$$

and is known as the Tavis-Cummings (TC) model [92, 93]. Here, ω_{X_n} is the exciton transition energy of the n-th QD, $|n\rangle$ denotes the state with one exciton in the n-th QD and all other QDs empty, g_n is the coupling strength between the n-th QD exciton and the cavity mode. We assume that all QD excitons are close to resonance with the cavity mode, and neglect any excited or multi-excitonic states within the same QD, as they are in general significantly off-resonance. The master equation for the density matrix $\rho(t)$ has the form

$$i\frac{d\rho}{dt} = \hat{\mathcal{L}}(t)\rho \,. \qquad (4.12)$$

The full time dependent Lindblad super-operator $\hat{\mathcal{L}}(t)$ can be written as

$$
\begin{aligned}
\hat{\mathcal{L}}(t)\rho &= \hat{L}\rho + [\mathcal{E}(t), \rho] \,, & (4.13) \\
\hat{L}\rho &= [H, \rho] - i\gamma_C \left(a^\dagger a \rho + \rho a^\dagger a - 2a\rho a^\dagger \right) \\
&\quad - i\sum_{n=1}^{N} \gamma_{X_n} \left[|n\rangle \langle n| \rho + \rho |n\rangle \langle n| - 2 |0\rangle \langle n| \rho |n\rangle \langle 0| \right], & (4.14)
\end{aligned}
$$

where γ_C and γ_{X_n} are the cavity damping and the exciton dephasing rate, respectively. The dynamics in such a system is solved as discussed in Appendix D which considers a single QD system. With N QDs coupled to the cavity, there are $N_1=1 + N$ states in the first rung and $N_2=1 + N(N+1)/2$ states in the second rung. This corresponds

to the N_1 transitions of GS $\leftrightarrow$ $M_{1\pm}$ and $N_1 N_2$ transitions of $M_{1\pm} \leftrightarrow M_{2\pm}$, giving rise to the total $M = N_1(1 + N_2)$ possible transitions in the system. The expansion of the density matrix then takes the form

$$\rho(t) = \sum_{i,j=0}^{N_1+N_2} \rho_{ij}(t) \left| i \right\rangle \left\langle j \right| , \tag{4.15}$$

where the uncoupled exciton-photon states $\left| i \right\rangle \equiv \left| n_{X_1}, n_{X_2}, \ldots, n_{X_j}; n_C \right\rangle$ with $n_X = 0,1$ and $n_C = 0,1,2,\ldots$ are the exciton and photon occupation numbers. The FWM polarization is given by

$$P(t,\tau) = \sum_{j=1}^{M} e^{-i\tilde{\omega}_j t} \times \begin{cases} \displaystyle\sum_{k=1}^{N_1} a_{jk} e^{i\lambda_{1,k}^* \tau} & \tau > 0 \\ \displaystyle\sum_{k=1}^{N_2} b_{jk} e^{i\lambda_{2,k} \tau} & \tau < 0 \end{cases} \tag{4.16}$$

with the complex frequencies

$$\tilde{\omega}_j = \lambda_{1,k} , \tag{4.17}$$

for the GS $\leftrightarrow$ $M_{2\pm}$ transition with $k = 1, 2, \ldots, N_1$, and

$$\tilde{\omega}_j = \lambda_{2,k} - \lambda_{2,m}^* , \tag{4.18}$$

for the $M_{1\pm} \leftrightarrow M_{2\pm}$ transition with $m = 1, 2, \ldots, N_1$ and $k = 1, 2, \ldots, N_2$. The energy levels $\lambda_{1,k}$, $\lambda_{2,k}$ are calculated by diagonalizing the effective non-Hermitian Hamiltonian

$$\tilde{H} = \begin{pmatrix} \tilde{H}_1 & 0 & 0 & \ldots \\ 0 & \tilde{H}_2 & 0 & \ldots \\ 0 & 0 & \tilde{H}_3 & \ldots \\ \vdots & \vdots & \vdots & \ddots \end{pmatrix} . \tag{4.19}$$

where $\tilde{H}_n$ refers to the n-th rung of TC ladder. The effective Hamiltonians describing
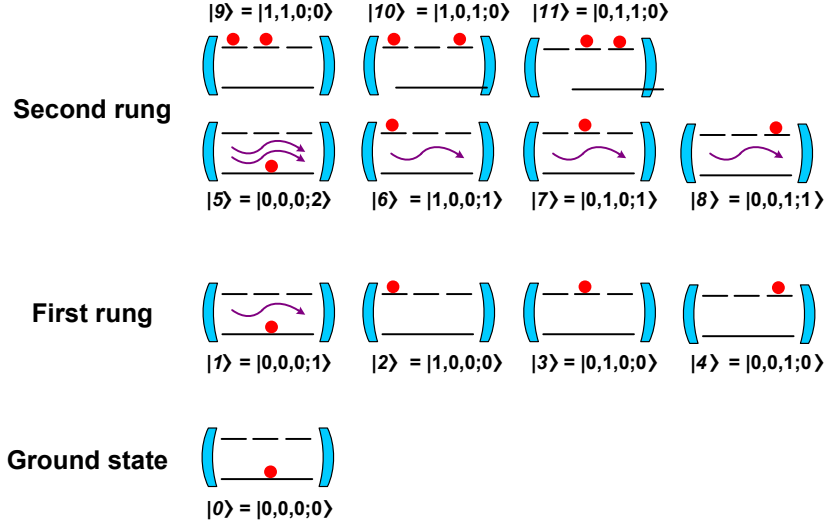
Figure 4.2: The basis of twelve states in TC ladder consists of GS, $N_1 = 4$ states of the first rung and $N_2 = 7$ state for the second rung.

the first and second rungs take the form

$$
\tilde{H}_1 =
\begin{pmatrix}
\tilde{\omega}_C & g_1 & g_2 & g_3 \\
g_1 & \tilde{\omega}_{X_1} & 0 & 0 \\
g_2 & 0 & \tilde{\omega}_{X_2} & 0 \\
g_3 & 0 & 0 & \tilde{\omega}_{X_3}
\end{pmatrix}
\tag{4.20}
$$

$$
\tilde{H}_2 =
\begin{pmatrix}
2\tilde{\omega}_C & \sqrt{2}g_1 & \sqrt{2}g_2 & \sqrt{2}g_3 & 0 & 0 & 0 \\
\sqrt{2}g_1 & \tilde{\omega}_C + \tilde{\omega}_{X_1} & 0 & 0 & g_2 & g_3 & 0 \\
\sqrt{2}g_2 & 0 & \tilde{\omega}_C + \tilde{\omega}_{X_2} & 0 & g_1 & 0 & g_3 \\
\sqrt{2}g_3 & 0 & 0 & \tilde{\omega}_C + \tilde{\omega}_{X_3} & 0 & g_1 & g_2 \\
0 & g_2 & g_1 & 0 & \tilde{\omega}_{X_1} + \tilde{\omega}_{X_2} & 0 & 0 \\
0 & g_3 & 0 & g_1 & 0 & \tilde{\omega}_{X_1} + \tilde{\omega}_{X_3} & 0 \\
0 & 0 & g_3 & g_2 & 0 & 0 & \tilde{\omega}_{X_2} + \tilde{\omega}_{X_3}
\end{pmatrix}
\tag{4.21}
$$

with $\tilde{\omega}_C = \omega_C - i\gamma_C$ and $\tilde{\omega}_{X_n} = \omega_{X_n} - i\gamma_{X_n}$.

In this work, we concentrate on a system of 3QDs ($N = 3$) coupled to the cavity. The basis is then reduced to twelve states, consisting of $N_1 = 4$ states of the
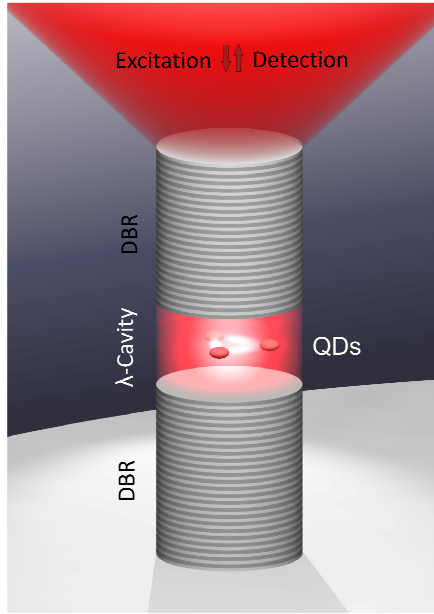
Figure 4.3: Sketch of the micropillar structure including the light coupling from the top facet.

first rung and $N_2 = 7$ state for the second rung (Fig. 4.2). Therefore, there are 32 possible transitions consisting of 4 transitions of GS $\leftrightarrow$ $M_{1\pm}$ and 28 transitions of $M_{1\pm} \leftrightarrow M_{2\pm}$.

4.4 STRUCTURES AND PARAMETERS

We concentrate on the QD-micropillar system consisting of a λ-GaAs spacer sandwiched between two DBRs made of $\lambda/4$ layer of GaAs and AlAs with 26 (30) mirror pairs in the top (bottom) DBR. The sketch of the micropillar structure is demonstrated in Fig. 4.3. A layer of self-assembled InGaAs QDs is embedded at the antinode of the confined photon field in the spacer. In this work, we have studied two cases: (i) 1QD-cavity system [93] and (ii) 3QDs-cavity system [94]. Actually, there are many QDs in the system, but only a few of them are strongly coupled and are in resonance with the cavity mode. To achieve the strong coupling regime, the oscillator strength of QD exciton needs to be large and the cavity mode should have a high Q-factor and a small volume. For the studied structure, the diameter of the micropillar is varied between 1.5 and 2.0 μm.

The input parameters are obtained from the micro-photoluminescence (μPL) spectra measured in the experiment. The PL spectrum at each temperature was fitted by a sum of Lorentzian lines. The resulting line positions as functions of temperature were fitted with the first rung transition energies $\lambda_{1,k}$ [given by Eq.(D.19) for 1QD-cavity and by the eigenvalues of Eq.(4.20) for 3QDs-cavity]. The temperature dependence of the uncoupled QD excitons and cavity energies can be fitted within an explicit model of the band gap shift of semiconductor [95]:

$$\omega_{X_n}(T) = \omega_{X_n}(0) + F(T), \tag{4.22}$$

$$\omega_C(T) = \omega_C(0) + \eta F(T), \tag{4.23}$$

$$F(T) = -\frac{\alpha\theta}{2}[\coth\left(\frac{\theta}{2T}\right) - 1], \tag{4.24}$$

where $\omega_{X_n}(0)$ and $\omega_C(0)$ are the exciton and cavity energies at T=0, η is the scaling factor for the cavity shift and α, θ are the fitting parameters.

Figure 4.4(a) shows the μPL spectra of the 1QD-cavity system for the sample temperature from 8 K to 30 K. The anticrossing is observed at approximately T=19 K with a Rabi splitting of $\Omega = 79\,\mu$eV. The fitted spectral positions of uncoupled (X,C) and coupled ($M_{1\pm}$) states are shown in Fig. 4.4(b). It is also seen in Fig. 4.4(a) that the pillar contains other QDs which are weakly coupled to the cavity mode, resulting in the crossing at around T=23 K. This corresponds to the enhancement of the linewidth by the Purcell effect [31], as can be seen in Fig. 4.4(c). The exchange of the linewidth between two polariton modes is typical for the strong coupling regime.

For a 3QDs-cavity system, the three individual excitons coupled to the cavity mode gives rise to the four polariton states as shown in Fig. 4.5. At low sample temperature, the exciton states are slightly blue-shifted from the cavity modes. As the temperature increases, the exciton states are tuned through the cavity mode due to a reduction of the semiconductor band gap. The avoided crossing between the cavity mode and three exciton states (X1, X2, X3) are observed at around 13 K, 21 K and 25 K respectively. To parameterise the detuning (δ) in this system, we introduce

82
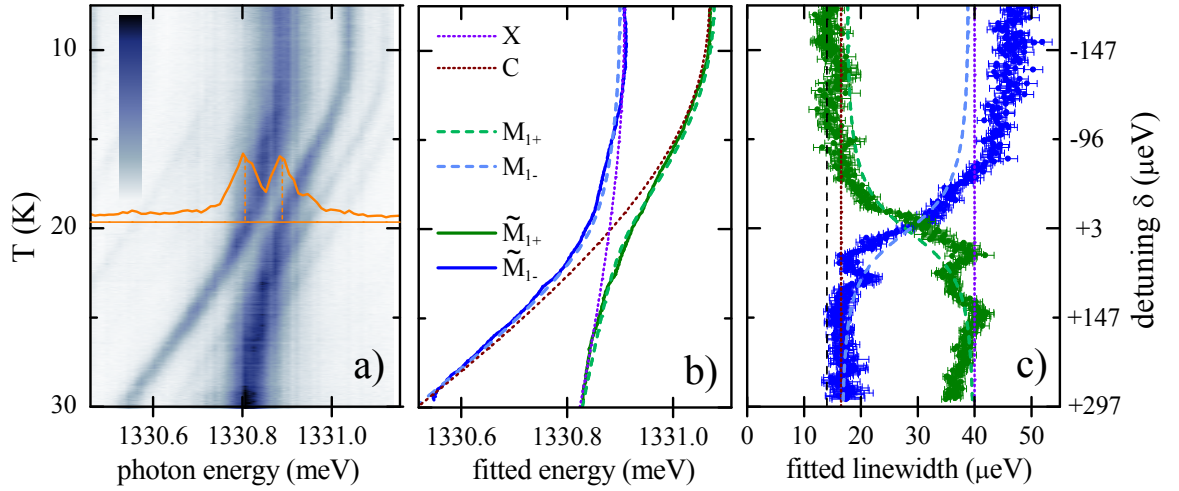
Figure 4.4: (a) The μPL spectra of a single QD-cavity system as function of the sample temperature. Spectral intensity on a linear colour scale from white (zero) to blue. An anticrossing between the cavity and exciton modes with a Rabi splitting of $\Omega = 79\,\mu$eV is observed at $T \approx 19\,$K as shown in an orange line. (b) The spectral positions of polaritons in the first rung of the JC ladder ($M_{1\pm}$) obtained from a Lorentzian line shape fit are shown as solid lines. The fitted energies of uncoupled states C, X (dotted lines) and coupled state $|M_{1+}\rangle, |M_{1-}\rangle$ (dashed lines) are calculated from Eq.(4.24). (c) The fitted linewidths of $\tilde{M}_{1+}, \tilde{M}_{1-}$ states are obtained from a Lorentzian lineshape fit (symbols). The resulting linewidths of uncoupled states (C, X) are shown as dotted lines and coupled state ($|M_{1+}\rangle, |M_{1-}\rangle$) as dashed lines.
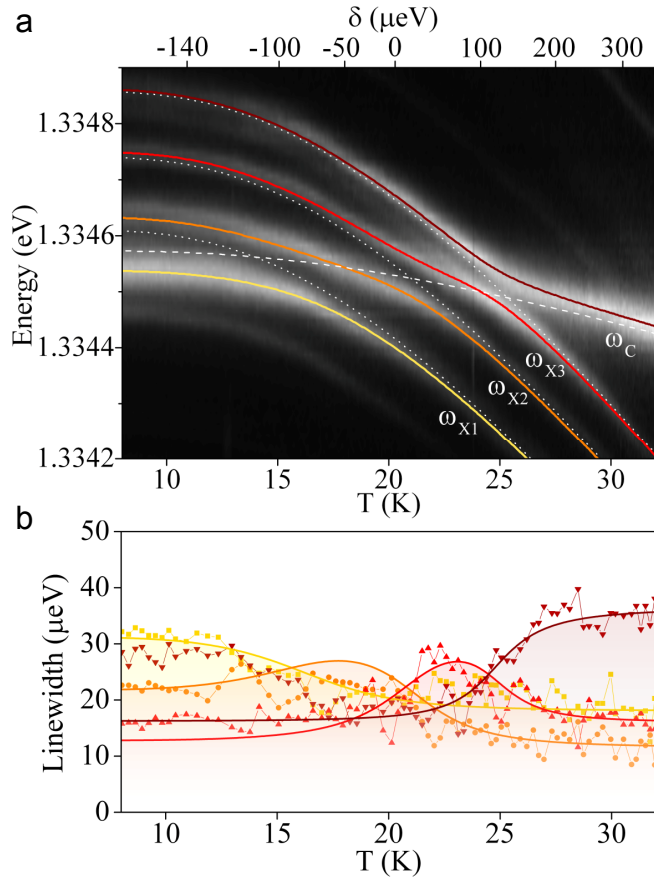
Figure 4.5: (a) The μPL spectra of a triple QDs-cavity system as function of the sample temperature. The energies of uncoupled exciton modes X1, X2, X3 (white dotted lines) and uncoupled cavity mode (white dashed line) are obtained from a Lorentzian line shape fit. The solid lines represent the fitted coupled polariton energies using Eq.(4.24). (b) The linewidths of coupled polariton states as function of the sample temperature (symbol: measured, line: modeling).

Parameter	1QD-cavity system	3QDs-cavity system	unit
ω_C	1330.909	1334.5732	meV
ω_X	1331.070	1334.6106	
		1334.7412	
		1334.8584	
g	39	43	μeV
		40	
		31.5	
γ_C	40	36.5	μeV
γ_X	16.5	18.0	μeV
		11.5	
		16.0	
α	58.05 ± 0.60	60.9 ± 0.6	μeV/K
θ	59.31 ± 0.40	58.9 ± 1.0	K
η	0.153297	0.227	

Table 4.1: Parameters of the 1QD-cavity and 3QD-cavity systems deduced from a fit to the temperature-dependent PL spectra.

the average cavity detuning as

$$\delta = \omega_C - \frac{\sum_{n=1}^{3} g_n \omega_{X_n}}{\sum_{n=1}^{3} g_n} \,, \tag{4.25}$$

corresponding to the values of -124, 16 and 124 μeV at the three anticrossings. The fitted linewidths are shown in Fig. 4.5(b). All parameters obtained from the μPL spectra fitting for the JC and TC models are summarized in Table. 4.1. The exciton and cavity linewidths include a Lorentzian spectrometer resolution of 4 μeV half width at half maximum (HWHM).

4.5 SINGLE-DOT/MICROCAVITY SYSTEM

4.5.1 SPECTRALLY AND TIME-RESOLVED FWM

To investigate the first two rungs of the JC ladder, the basis of *five* lowest states (GS, $M_{1\pm}$, $M_{2\pm}$) is used in the density matrix. This allow us to access both the GS $\leftrightarrow$ M$_{1\pm}$ and $M_{1\pm} \leftrightarrow M_{2\pm}$ transitions. The *spectrally resolved* FWM power $|P(\omega, \tau=0)|^2$ at zero detuning (δ=0) is demonstrated in Fig. 4.6. The signal after the
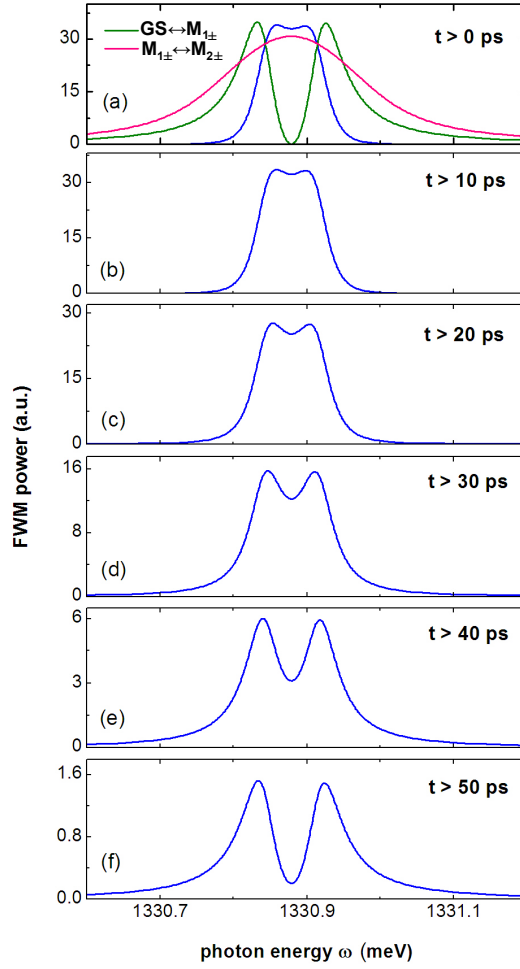
Figure 4.6: FWM power $|P(\omega, \tau)|^2$ at $\delta{=}0$ for different post-selected times t. The decomposition into GS $\leftrightarrow$ M$_{1\pm}$ (magenta line, multiplied by a factor of 0.5) and $M_{1\pm} \leftrightarrow M_{2\pm}$ (green line) transitions are shown in (a).

arriving of the second pulse [blue curve in Fig. 4.6(a)] does not show the Rabi doublet because it contains all six possible transitions. The GS $\leftrightarrow$ M$_{2\pm}$ transition does not contribute because its transition energy is large giving rise to a fast dephasing. The decomposition of the signal into GS $\leftrightarrow$ M$_{1\pm}$ (green line) and $M_{1\pm} \leftrightarrow M_{2\pm}$ (red line) transitions is also shown in Fig. 4.6(a). The GS $\leftrightarrow$ M$_{1\pm}$ transitions show the vacuum Rabi doublet, while the quadruplet of M$_{1\pm}$ $\leftrightarrow$ M$_{2\pm}$ transitions create a *spectrally* broad peak due to a faster dephasing of the second rung (about four times faster compared to the GS $\leftrightarrow$ M$_{1\pm}$ transitions). The FWM spectra after a time lag t_0 is

86
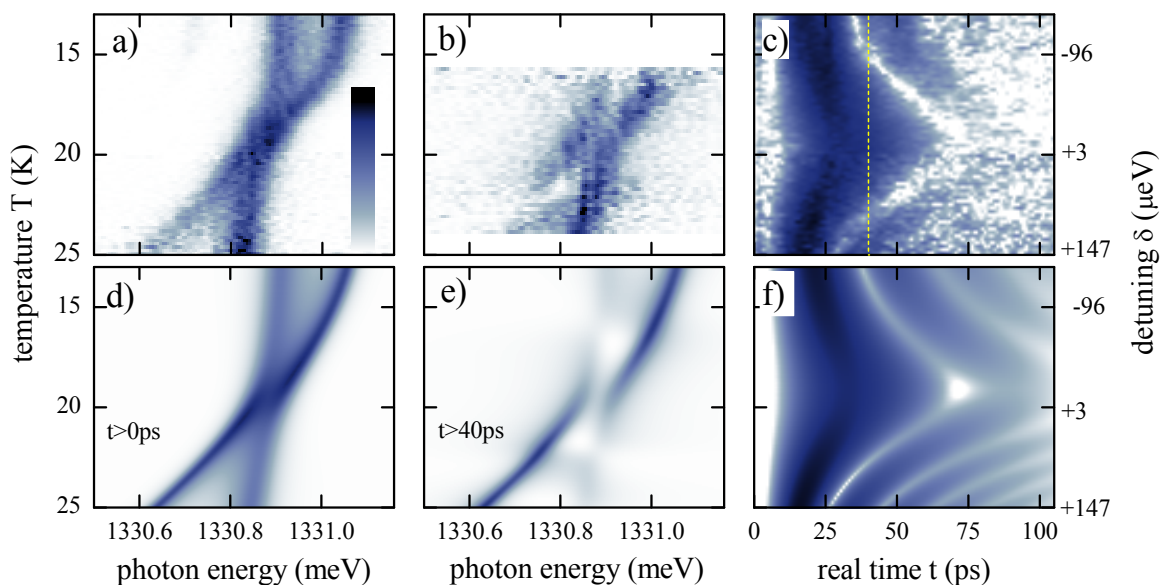
Figure 4.7: Temperature dependence of *spectrally resolved* FWM at zero-delay, $|P(\omega, \tau{=}0)|^2$, for (a) measurement, (d) prediction and post-selected at $\tau{=}40\,$ps, $|P(\omega, \tau{=}0; t{=}40\text{ps})|^2$, for (b) measurement, (e) prediction. (c) Measured and (f) predicted *time-resolved* FWM $|P(t, \tau{=}0)|$ as function of temperature. The post-selected time $t = 40\,$ps is shown in (c) as a dashed line. The detuning δ determined by Eq.(4.25) is also shown on the right axis.

calculated by

$$P(\omega, \tau; t) = \int_{t_0}^{\infty} P(t, \tau) e^{i\omega t} dt. \tag{4.26}$$

It is clearly seen in Fig. 4.6(b)-4.6(f) that the fast dephasing component can be suppressed at later time. At around $t{>}40\,$ps, we can observe the Rabi-split doublet of the GS $\leftrightarrow$ M$_{1\pm}$ transitions. The experimental and theoretical *spectrally resolved* FWM as function of temperature for $t{=}0$ and $t{=}40\,$ps are shown in Fig. 4.7, demonstrating a good agreement between the two. The result in Fig. 4.7 is the same as presented in Fig. 4.6 but for different detunings (different temperatures). As expected, the Rabi splitting can be clearly observed at $t{>}40\,$ps when the second rung transitions are suppressed. The anticrossing shows that the system is in the strong-coupling regime.

The measured and predicted *time-resolved* FWM amplitude $|P(t, \tau{=}0)|$ as function of temperature is demonstrated in Fig. 4.7(c) and 4.7(f), respectively. The real-time dynamics shows delayed rise and oscillations of the signal. This initial delayed is caused by the coupling of the excitation pulses to the cavity photon

which is free from non-linearity. Only when the corresponding initial superposition $|M_{1+}\rangle + |M_{1-}\rangle$ has evolved with time towards $|M_{1+}\rangle - |M_{1-}\rangle$ through the Rabi-oscillation, it acquires an excitonic component and then the FWM is created. Again, the time evolution exhibits the oscillations due to the interference of the six possible transitions. Therefore, it is not only given by the vacuum Rabi splitting of the first rung transitions, but also by the second rung transitions. The FWM rise-time and oscillations are the largest for $\delta=0$, corresponding to the smallest frequency splitting of the six transition in the JC ladder.

4.5.2 Quantum strong coupling regime

The coherent evolution of the GS $\leftrightarrow$ M$_{1\pm}$ and GS $\leftrightarrow$ M$_{2\pm}$ transitions can be separately probed using positive and negative delay times respectively. For a positive delay ($\tau>0$), a one-photon coherence on GS $\leftrightarrow$ M$_{1\pm}$ transitions created by the first pulse $\mathcal{E}_1$ is probed by the pulse $\mathcal{E}_2$, so that the delay-time dependence is measuring the coherent dynamics of the M$_{1\pm}$ state. For a negative delay ($\tau<0$), the FWM polarization is proportional to a two-photon coherence on GS $\leftrightarrow$ M$_{2\pm}$ which is created by the pulse $\mathcal{E}_2$ and then probed by the pulse $\mathcal{E}_1$. Therefore, the delay-time dependence is given by the coherent dynamics of the M$_{2\pm}$ state.

The delay time dependence of the FWM power for different detunings is shown in Fig. 4.8. At $\delta=0$, the calculated FWM power for positive delays shows a beat of the first rung with a period of approximately 52 ps. This corresponds to a vacuum Rabi splitting of 80 μeV which is in a good agreement with the Rabi splitting measured in μPL. The beat period for negative delays is $\sqrt{2}$ shorter than that for positive delays due to a $\sqrt{2}$ larger splitting in the M$_{2\pm}$ state. The resulting beat period is therefore around 36 ps for negative delays. This observation demonstrates the quantum strong coupling regime in the system as more than one photon participate. It is also found that the exponential decay of negative delays ($\tau<0$) is much faster than that of positive delays ($\tau>0$). This is because the $M_{2\pm}$ states have a photon content of 3/2 which is three times larger than a photon content of 1/2 in the $M_{1\pm}$ states, so that the decay rate for negative delays decreases by a factor of three. We have also
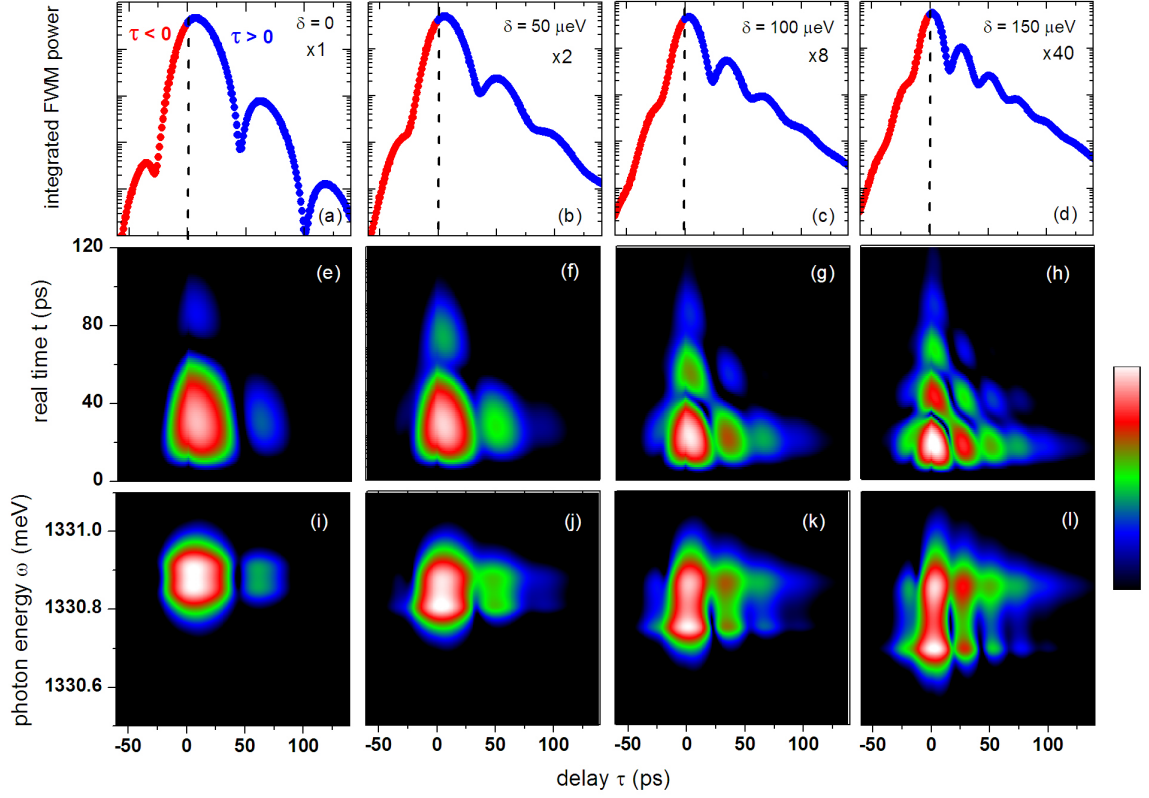
Figure 4.8: Delay-time dependence of FWM for different temperature, corresponding to the detuning $\delta = 0, 50, 100, 150\,\mathrm{ps}$. Top row: time-integrated FWM $\int |P(t,\tau)|^2\,dt$. Middle row: *time-resolved* FWM $|P(t,\tau)|^2$. Bottom row: *spectrally resolved* FWM $|P(\omega,\tau)|^2$. The calculated results for $\delta = 0, 50, 100, 150\,\mathrm{ps}$ are multiplied by a factor of 1, 5, 20, 40 respectively.
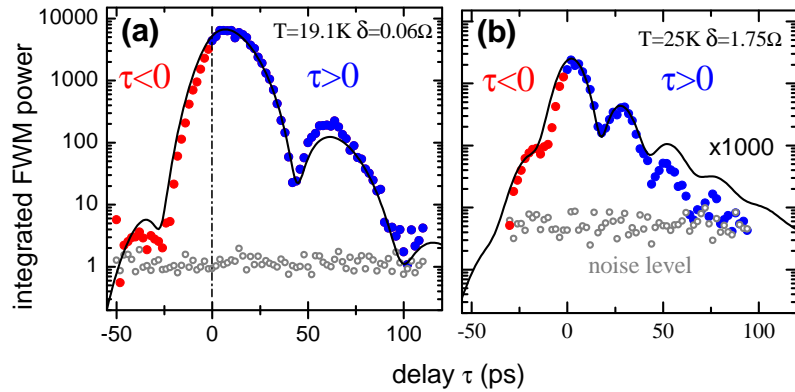
Figure 4.9: Measurement and prediction of time-integrated FWM $\int |P(t,\tau)|^2\,dt$ at (a) T=19.1 K and (b) T=25 K, on a logarithmic colour scale over 5 orders of magnitude.

calculated the time-integrated FWM for δ=50, 100 and 150 ps, as demonstrated in Fig. 4.8(b)-4.8(d) respectively. The increasing detuning causes the reduction of the photon content in the $M_{1\pm}$ and $M_{2\pm}$ states, giving rise to a longer exponential decay. The result also shows that the oscillations are faster for larger detuning. This is due to the fact that the splitting in all rungs is proportional to the detuning as $\sqrt{n\Omega^2 + \delta^2}$, so that the beat has a shorter period. The *time-resolved* and *spectrally resolved* FWM power are shown in Fig. 4.8(e)-(l). As expected, the shorter period and larger splitting are observed for larger detuning. We have also compared the calculated time-integrated FWM with the measurement observation. Figure 4.9 demonstrates a quantitative agreement between the two.

4.6   Triple-dot/microcavity system

4.6.1   Quantum beat

We have calculated the delay time dependence of FWM for different temperatures as demonstrated in Fig. 4.10 for *spectrally resolved* and Fig. 4.11 for *time-resolved* FWM. The signal changes slowly as the temperature increases. A faster beat period is observed if the cavity and exciton modes are off-resonance, corresponding to a larger polartiton splitting as discussed in the case of a single-QD system. The time-integrated FWM at four different temperatures (three X-C resonant temperatures T=13, 21, 25 K and off-resonant temperatures T=19 K) are shown in Fig. 4.12. When the cavity is tuned to one of the QD excitons, the resulting beat period is strongly dominated by the tuned exciton mode. At T=13 K [Fig. 4.12(a)] the cavity mode is in resonance with X1 and detuned by 141 μeV and 258 μeV from X2 and X3 respectively. The resulting beat has a period of around 50 ps, corresponding to a polariton splitting of approximately 83 μeV which is close to the Rabi splitting $2g_1$=86 μeV of X1. The 3 μeV difference is due to the remaining influence of the other two excitons X2 and X3. Note that the influence of X2 are larger than that of X3 because X2 has smaller detuning. The same happens at T=21 K (T=25 K) when the X2 (X3) is in resonance with the cavity mode. The beat period of about 59 ps
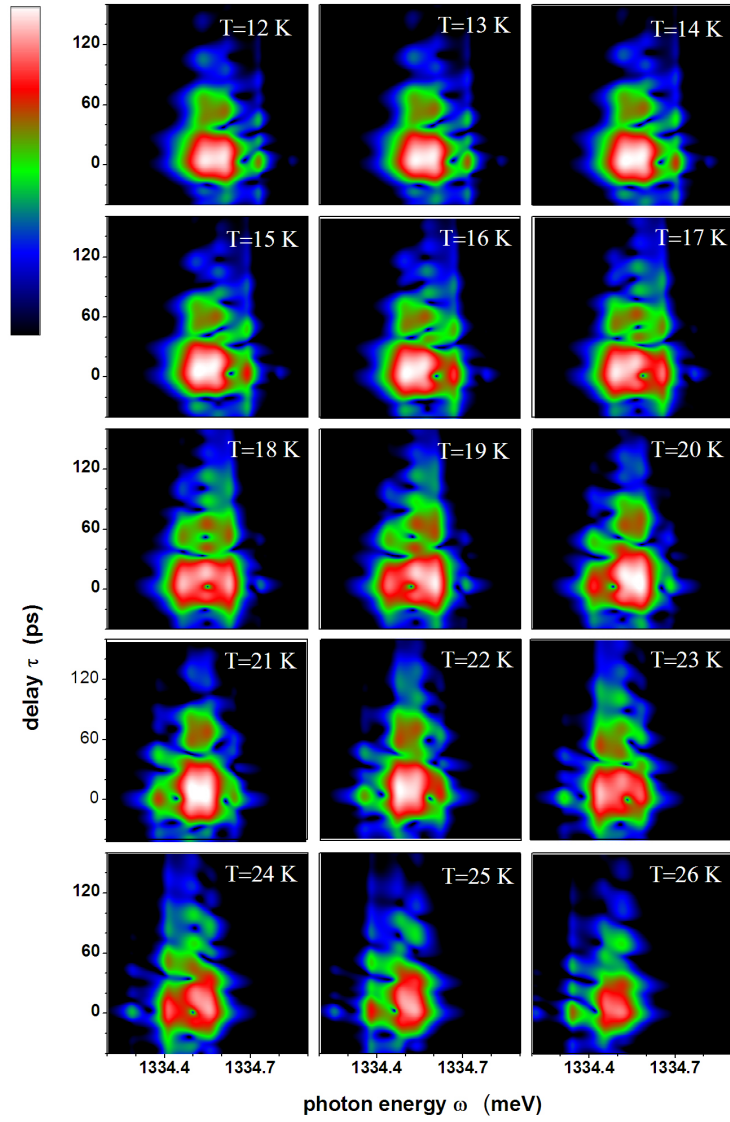
Figure 4.10: Delay-time dependence of *spectrally resolved* FWM $|P(\omega, \tau)|^2$ for different temperature, on a logarithmic colour scale over 3 orders of magnitude.
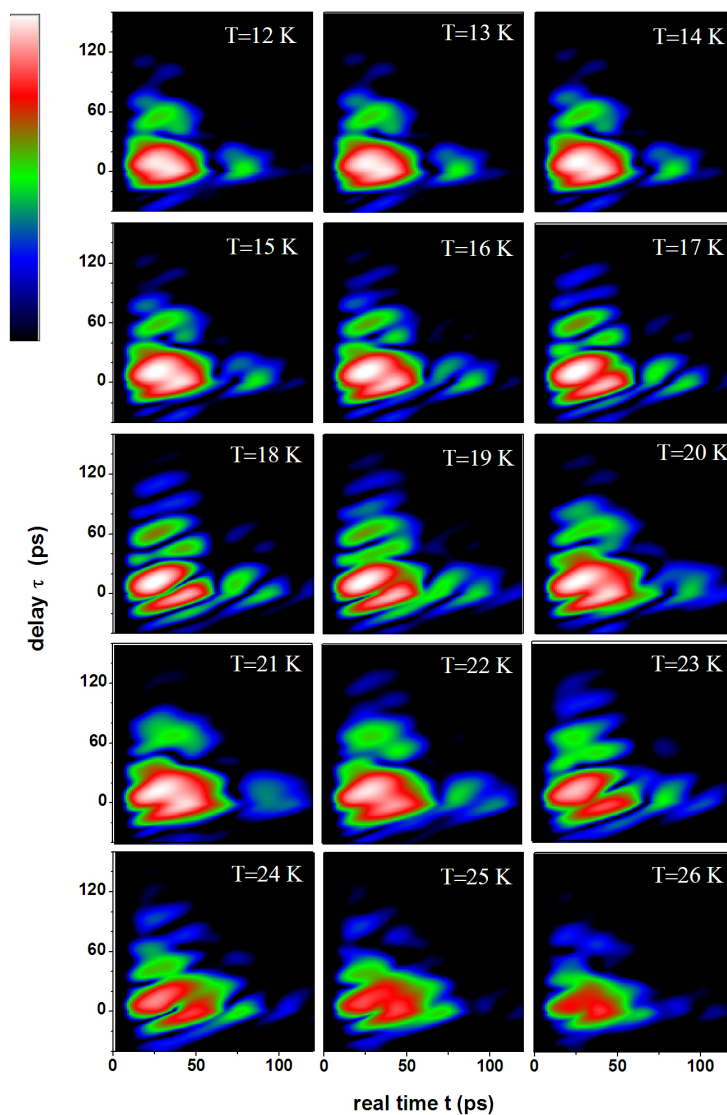
Figure 4.11: Delay-time dependence of *time-resolved* FWM $|P(t,\tau)|^2$ for different temperature, on a logarithmic colour scale over 3 orders of magnitude.
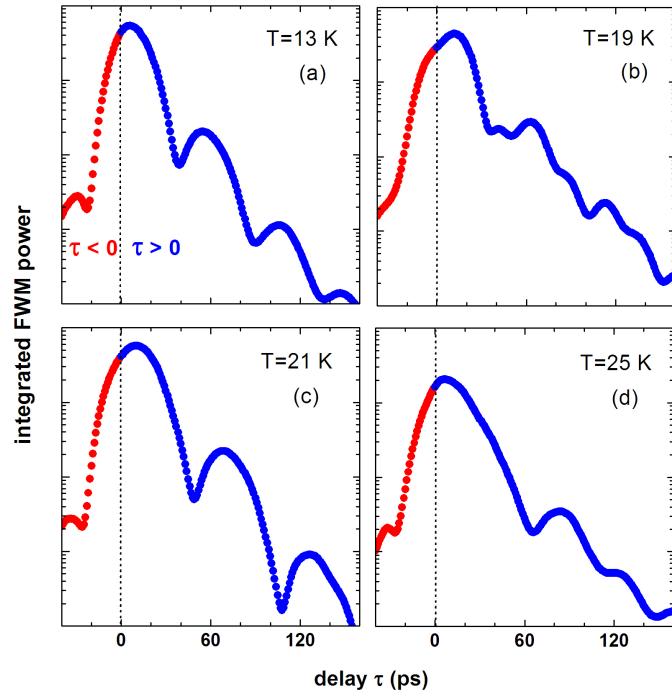
Figure 4.12: Time-integrated FWM $\int |P(t,\tau)|^2 \, dt$ for four different temperatures, on a logarithmic colour scale over 3 orders of magnitude.
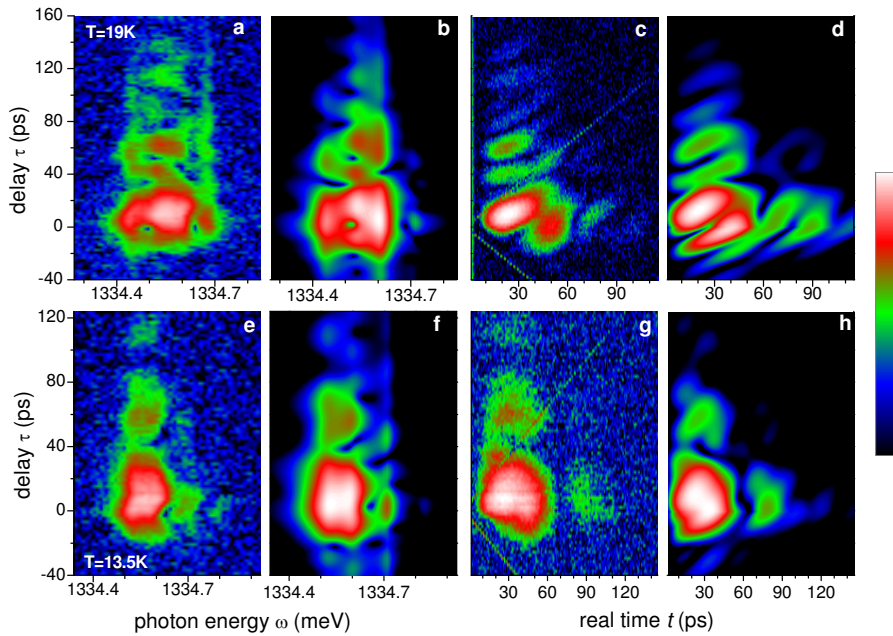
Figure 4.13: Comparison between measurement and theory of *spectrally resolved* $|P(\omega,\tau)|^2$ and *time-resolved* $|P(t,\tau)|^2$ FWM at T=19 K (a)-(d) and T=13.5 K (e)-(h), on a logarithmic colour scale over 3 orders of magnitude.

(74 ps) gives rise to the energy splitting of $70\,\mu$eV ($58\,\mu$eV). The values are $10\,\mu$eV ($5\,\mu$eV) smaller than the Rabi splitting of $2g_2{=}80\,\mu$eV ($2g_3{=}63\,\mu$eV). In the case of X2-C resonance, the 10-μeV difference is a bit larger than that of the other two resonances. This is because the cavity mode is in between X1 and X3 with nearly the same detuning ($130\,\mu$eV from X1 and $118\,\mu$eV from X3). Therefore, the influence of X1 and X3 are comparable in this case. In the off-resonant case, a faster beat is observed. The beat period is around $17\,$ps, corresponding to the polaritonic splitting of approximately $243\,\mu$eV which is much larger than the Rabi splitting of any individual exciton. This indicates that all four polaritons contribute to the coherent dynamics. The comparison of experimental and predicted results for two different temperatures is presented in Fig. 4.13, showing a quantitative agreement between them.

4.6.2 Coherent coupling and two-dimensional FWM spectroscopy

The coherent coupling phenomena is observed during and immediately following photoexcitation by a laser source. In semiconductors, the dephasing time is of order of picosecond or femtosecond. Therefore, an ultrashort laser pulse is used to study the coherent regime. To achieve the strong coherent coupling regime, the coupling between two states must exceed the decoherence rate of each state. The mechanism of the coherent coupling is investigated using the two-dimensional (2D) frequency domain representation [96]. The FWM $P(\omega, \tau)$ is Fourier-transformed from the delay time domain τ into the conjugated frequency domain ω_τ, giving rise to the 2D FWM $P(\omega, \omega_\tau)$. In this work, we use the FWM for the positive delays ($\tau{>}0$) only. Therefore, the frequency ω_τ represent the frequency of the first-order polarization created by the pulse E_1. The FWM polarization has the form

$$P(t, \tau) = \sum_{j=1}^{M} \sum_{k=1}^{N_1} a_{jk} e^{-i\tilde{\omega}_j t} e^{i\tilde{\lambda}_{1,k}^* \tau} \,. \tag{4.27}$$

Its 2D Fourier transform is calculated straightforward by solving

$$P(\omega, \omega_\tau) = \sum_{j=1}^{M} \sum_{k=1}^{N_1} \frac{a_{jk}}{(\omega - \tilde{\omega}_j + i\gamma_s)(\omega_\tau + \tilde{\lambda}_{1,k}^*)} \, , \tag{4.28}$$

where N_1=4 for states of the first rung, M=32 for all possible transitions (as discussed in the TC model section) and γ_s=4 μeV is the HWHM of the Lorentzian spectrometer resolution. The 2D FWM power is calculated for different temperatures (Fig. 4.14), showing the diagonal and off-diagonal peaks. For diagonal peaks, the signals have the same first- and third-order frequencies ($\omega_\tau = \omega$). This means that the third-order polarization is dominated by the same exciton state as the first-order polarization. When one exciton state is in resonance with the cavity mode, there are two dominant peaks in a diagonal lines indicating the two dominant polariton modes. From T=16 K to T=20 K, the 2D FWM features change slowly as the position of cavity mode moves from X1-resonance to X2-resonance. At T=18 K, the cavity mode is in between X1 and X2, it is detuned by 64 μeV from X1 and 67 μeV from X2. The three diagonal peaks (at approximately 1334.45 meV, 1334.55 meV and 1334.64 meV) represent the three frequencies of polariton states dominated by X1, X2 and C modes. The resonances created in the first-order polarization not only couple to itself in the third-order polarization ($\omega_\tau = \omega$ on diagonal line), but also couple to different resonances in the third-order polarization ($\omega \neq \omega_\tau$ corresponding to off-diagonal peak) if two states are coherently coupled to each other. As a result, a pair of coupled states can create a square-like feature in the 2D FWM. In Fig. 4.14, two squares which correspond to the X1-C coupling and X2-C coupling have equal strength due to the comparable detuning of X1-C and X2-C. The lower frequency square is less visible at T=19 K because the cavity mode is closer to X2 than to X1 (it is 84 μeV above X1 and 46 μeV below X2). It is shown that the coherent coupling can be observed for all values of the temperature.
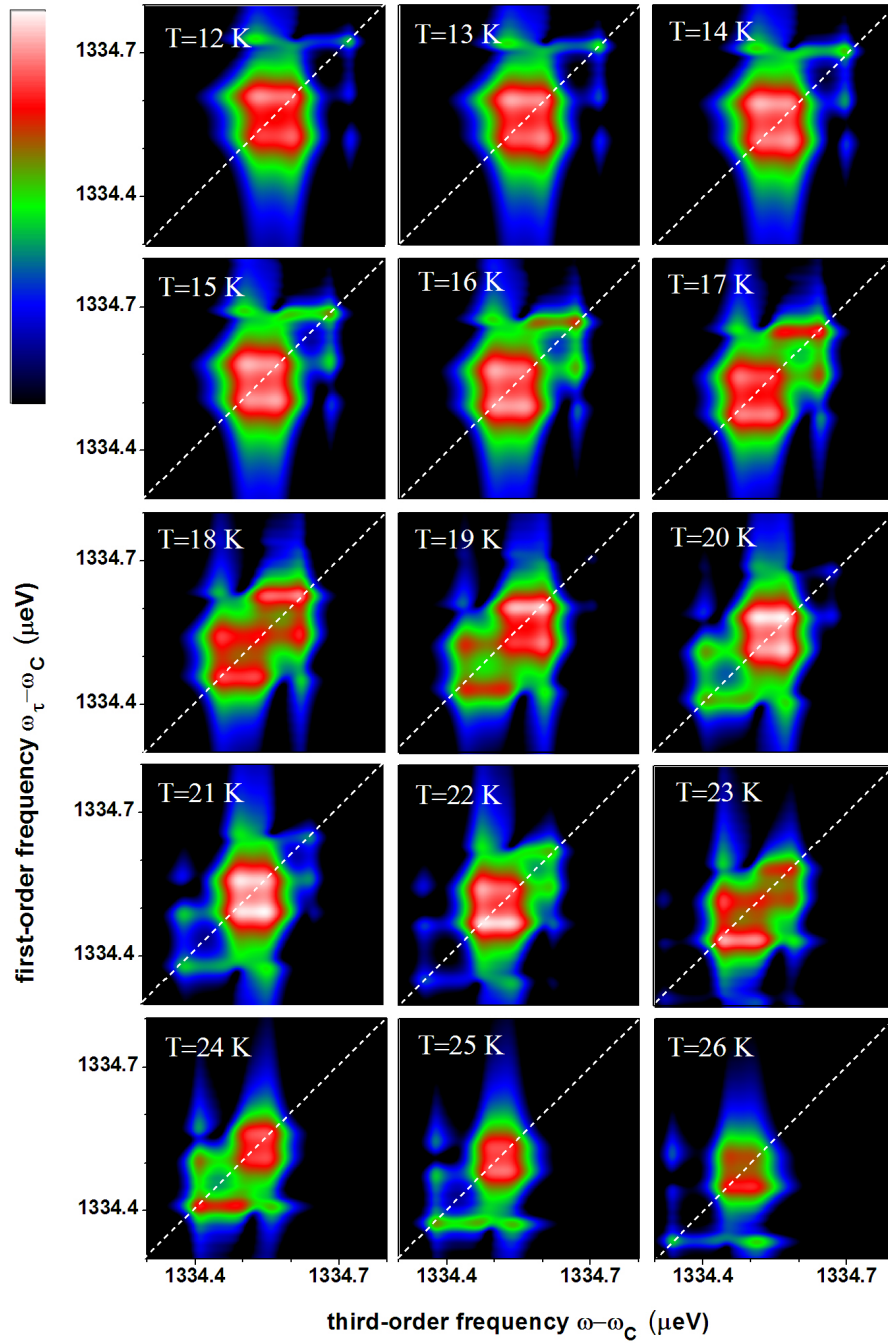
Figure 4.14: 2D FWM $|P(\omega, \omega_\tau)|^2$ for different temperature, on a logarithmic colour scale over 3 orders of magnitude.

4.6.3 PHASE CORRECTION AND COMPARISON WITH EXPERIMENTAL DATA

To compare the theoretical 2D FWM with the experimental observation, a phase correction is necessary because the phase in experiment is random, i.e. it is different for different delay time τ. We use the same phase correction as for the experiment which is given by

$$\tilde{P}_{cor}(\omega, \tau) = \tilde{P}(\omega, \tau) \exp\left\{i[\varphi + \omega'_{cor}\tau - \arg(\tilde{P}(\omega_{cor}, \tau))]\right\}, \qquad (4.29)$$

where ω'_{cor}, ω_{cor} are the corrected frequencies. The corrected polarization $\bar{P}_{cor}(\omega, \omega_\tau)$ is calculated for different φ, varying it between 0 and 2π. Then we determine the minimum phase $\varphi = \varphi_{\min}$ in such a way that the deviation (Δ_{cor}) between the corrected and uncorrected FWM at $\varphi = \varphi_{\min}$ is minimum,

$$\Delta_{cor}(\omega_{cor}, \omega'_{cor}) = \int \int \left|\bar{P}_{cor}(\omega, \omega_\tau) - \bar{P}(\omega, \omega_\tau)\right|^2 d\omega \, d\omega_\tau. \qquad (4.30)$$

We then use $\varphi = \varphi_{\min}$ for each ω_{cor} and ω'_{cor} to calculate the deviation $\Delta_{cor}(\omega_{cor}, \omega'_{cor})$ as shown in Fig. 4.15 for the full $\bar{P}_{cor}(\omega, \omega_\tau)$ and post-selected $\bar{P}_{cor}(\omega, \omega_\tau, t_s{=}42.5\text{ps})$ at $T{=}19\,\text{K}$. The deviation is slowly varying versus ω_{cor} with well defined regions of small deviation. Figure 4.16 demonstrates the 2D FWM at a fixed $\omega_{cor}{=}1334.55\,\mu\text{eV}$ for different ω'_{cor}. It is shown that changing ω'_{cor} only shifts the data in ω_τ-axis and does not change its shape. For the following calculated data, we use $\omega'_{cor}{=}1334.60\,\mu\text{eV}$ which gives the minimum deviation Δ_{cor} as shown in Fig. 4.15. The effect of ω_{cor} on the 2D FWM data is demonstrated in Fig. 4.17 for the full $\bar{P}_{cor}(\omega, \omega_\tau)$ and Fig. 4.18 for the post-selected $\bar{P}_{cor}(\omega, \omega_\tau, t_s{=}42.5\text{ps})$. The shape of 2D FWM slowly changes with changing ω_{cor}. Note that the off-diagonal peaks are observed for all values of ω_{cor} which covers the range of significant FWM signal and can not be all eliminated simultaneously. This indicates that the off-diagonal signals are due to the coherent coupling of the polariton modes, they can not be due to the uncoupled resonances. Due to the contributions of the 28 transitions of the second rung, the features of 2D FWM in the third-order polarization(ω-axis) are broadened. The second rung
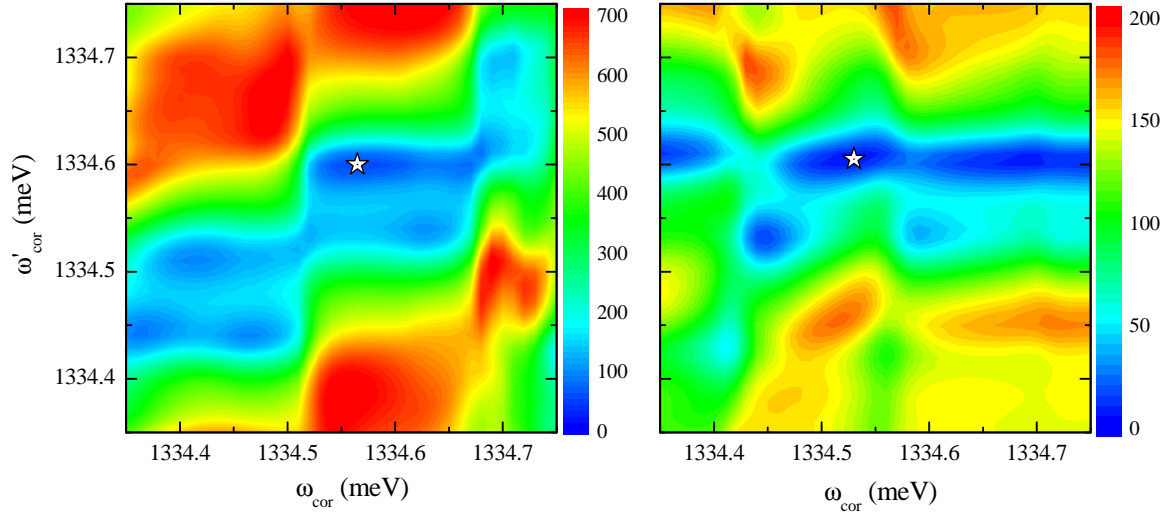
Figure 4.15: Deviation due to the phase correction given by $\Delta_{cor}(\omega_{cor}, \omega'_{cor})$ in arbitrary units, for the predicted 2D FWM at T=19 K. Left: for $\bar{P}_{cor}(\omega, \omega_\tau)$, right: $\bar{P}_{cor}(\omega, \omega_\tau; t$=42.5ps). The correction energies used for the following calculation are indicated as white stars.

transitions are suppressed in the case of the post-selected 2D FWM. The resulting $\bar{P}_{cor}(\omega, \omega_\tau, t_s = 42.5\text{ps})$ shows a clear separation between the multiple off-diagonals at the polariton frequencies as can be seen in Fig. 4.18. We also compare the corrected calculated and experimental 2D FWM data at T=19 K using the same phase correction, i.e. the same $\varphi_{\min}$ and the same correction frequencies ω_{cor} and ω'_{cor}. The comparison shows a good agreement between the theoretical result and measurement as seen in Fig. 4.19 for the FWM amplitude and Fig. 4.20 for FWM phase. The data for the amplitude (Fig. 4.19) and the phase (Fig. 4.20) are also plotted all together in a 3D representation in Fig. 4.21.
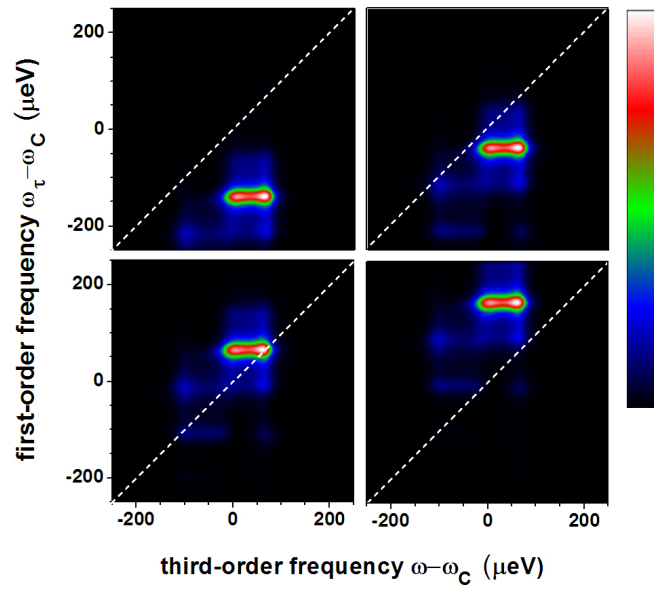
Figure 4.16: Phase corrected 2D FWM $\left|\bar{P}_{cor}\left(\omega,\omega_{\tau}\right)\right|^{2}$ for different ω'_{cor} and $\omega_{cor} = 1334.55\,\text{meV}$. Linear colour scale as given from zero (black) to the maximum amplitude (white).
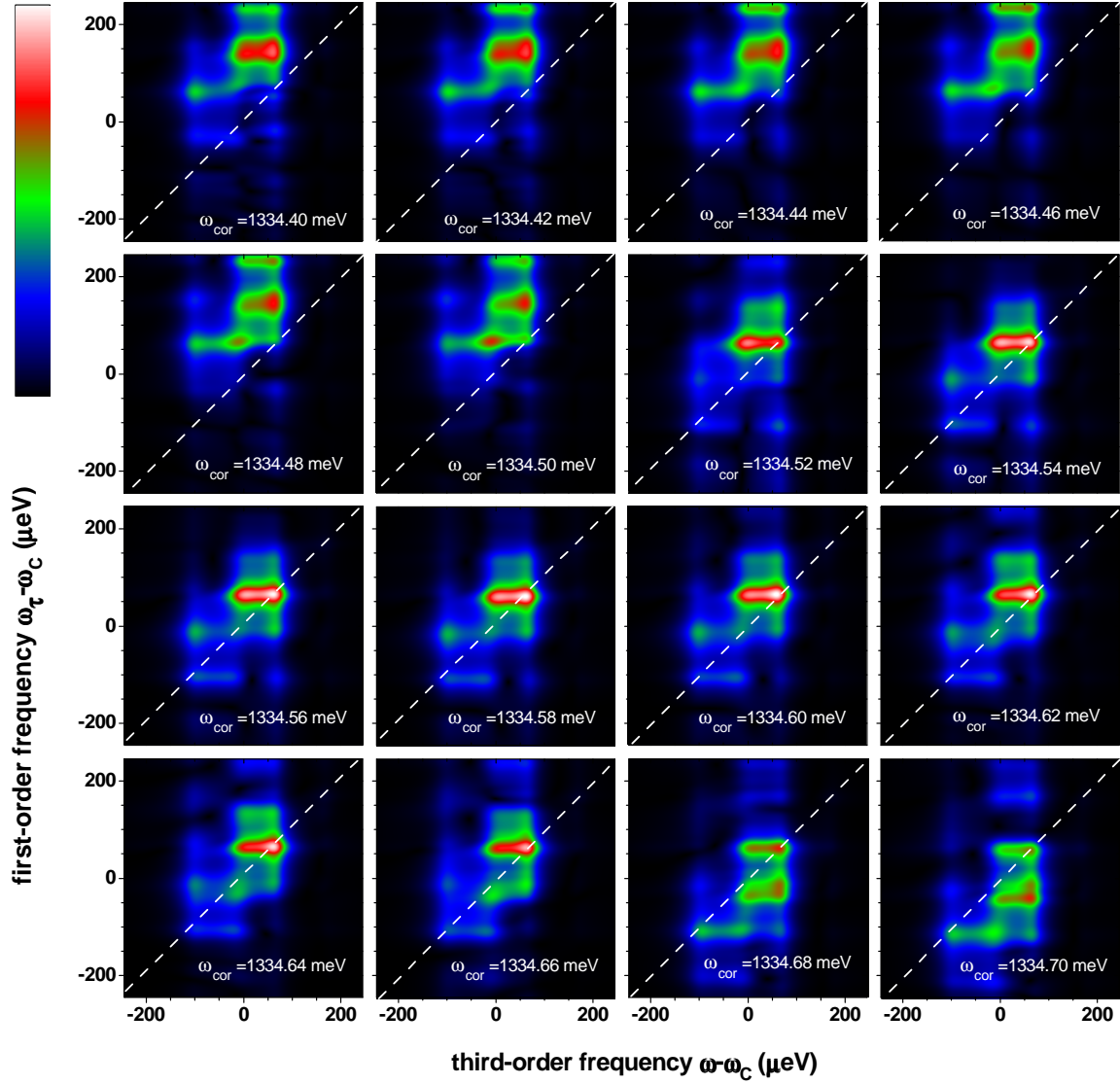
Figure 4.17: Phase corrected 2D FWM $\left|\bar{P}_{cor}(\omega,\omega_\tau;t{=}0)\right|^2$ at $T{=}19\,\mathrm{K}$ with $\omega_C = 1334.537\,\mathrm{meV}$, for different ω_{cor} and $\omega'_{cor} = 1334.60\,\mathrm{meV}$. Linear colour scale as given from zero (black) to the maximum amplitude (white).
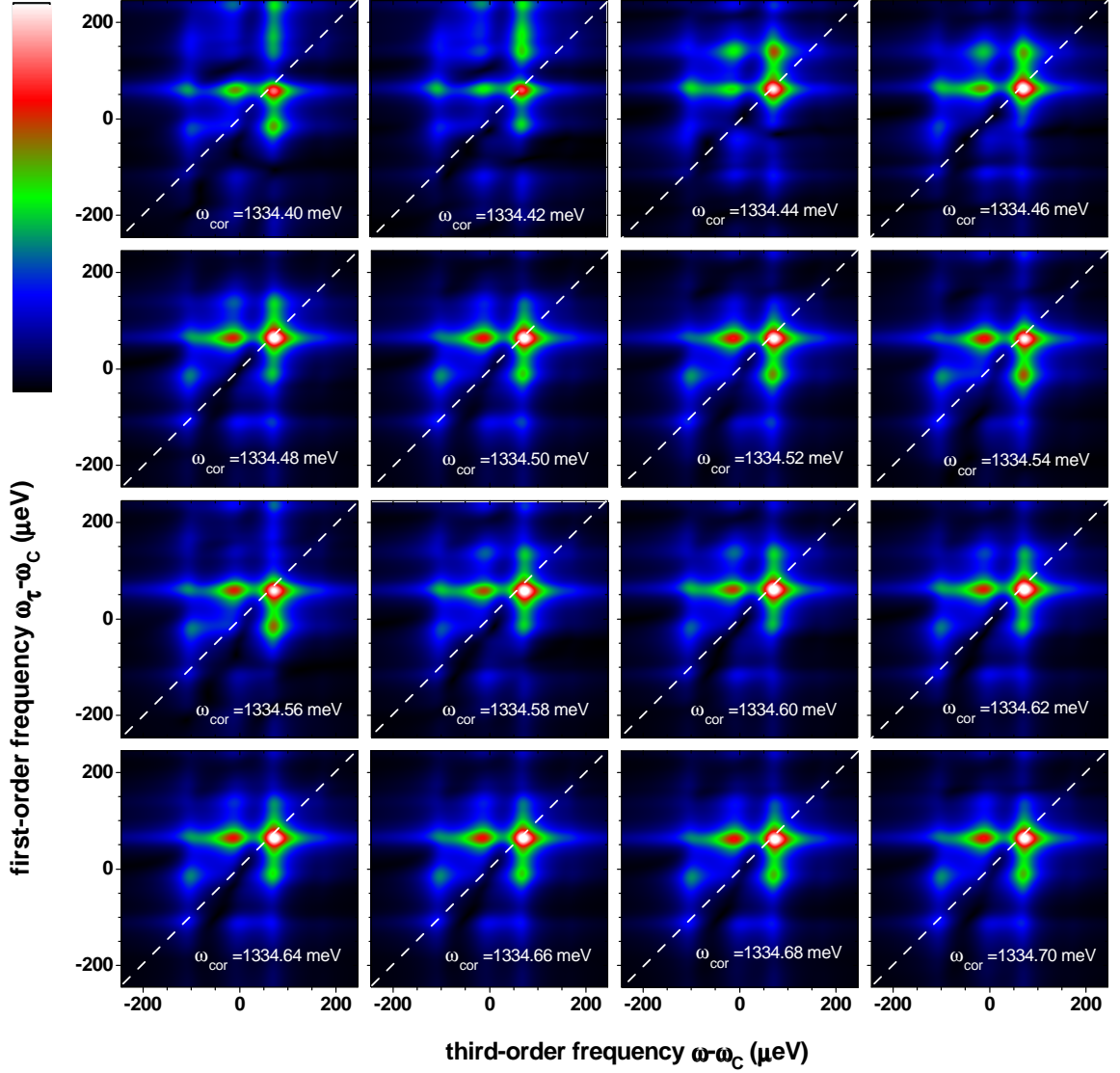
Figure 4.18: Phase corrected 2D FWM $\left|\bar{P}_{cor}(\omega, \omega_\tau; t{=}42.5\mathrm{ps})\right|^2$ at $T{=}19\,\mathrm{K}$ with $\omega_C = 1334.537\,\mathrm{meV}$, for different ω_{cor} and $\omega'_{cor} = 1334.60\,\mathrm{meV}$. Linear colour scale as given from zero (black) to the maximum amplitude (white).
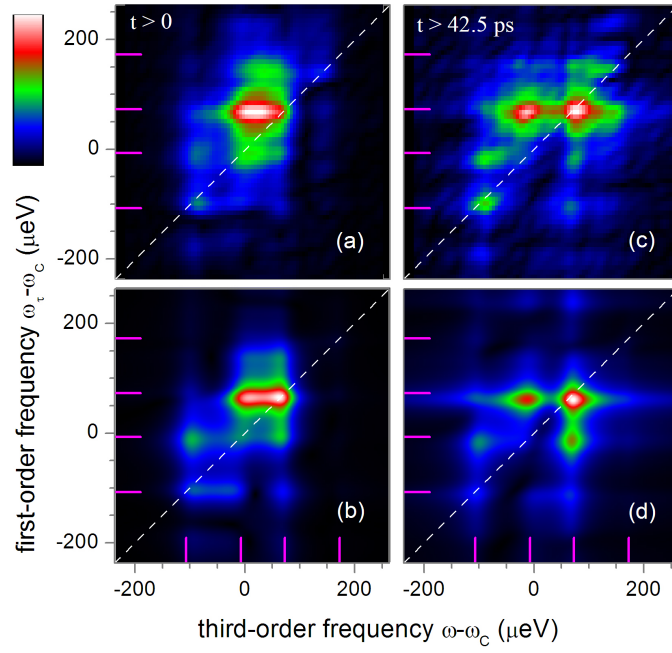
Figure 4.19: 2D FWM at $T = 19\,\text{K}$ with $\omega_C = 1334.537\,\text{meV}$, for (a) measurement, (b) prediction of $\left|\bar{P}_{cor}(\omega,\omega_\tau;t{=}0)\right|$ and (c) measurement, (d) prediction of post-selected $\left|\bar{P}_{cor}(\omega,\omega_\tau;t{=}42.5\text{ps})\right|$. Linear colour scale as given from zero (black) to the maximum amplitude (white). Magenta ticks indicate the polariton frequencies of the first rung $\lambda_{1,k}$.
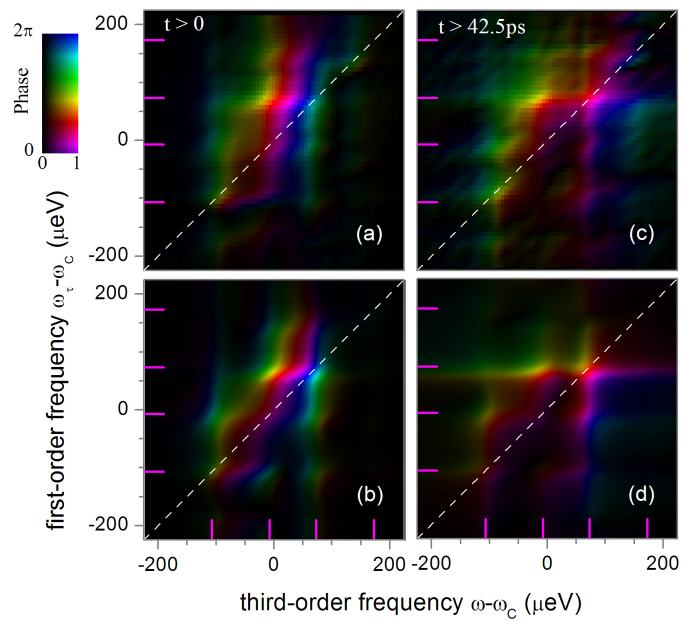
Figure 4.20: 2D FWM at $T = 19\,\mathrm{K}$ with $\omega_C = 1334.537\,\mathrm{meV}$, for (a) measurement, (b) prediction of $\left|\bar{P}_{cor}(\omega, \omega_\tau; t{=}0)\right|$ and (c) measurement, (d) prediction of post-selected $\left|\bar{P}_{cor}(\omega, \omega_\tau; t{=}42.5\mathrm{ps})\right|$. Colour scale as given, encoding the amplitude as value and the phase as hue. Magenta ticks indicate the polariton frequencies of the first rung $\lambda_{1,k}$.
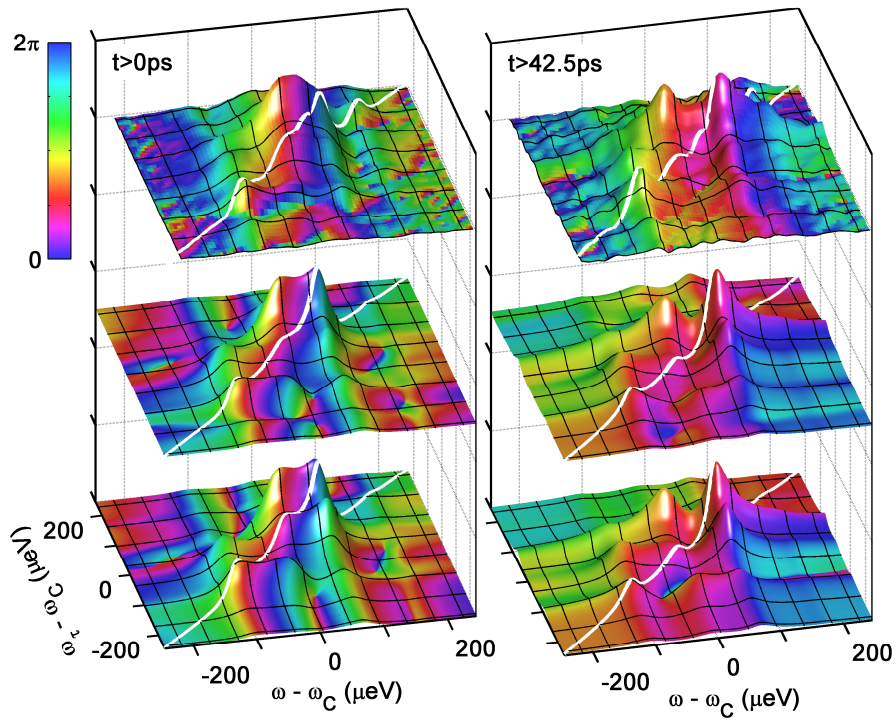
Figure 4.21: 3D FWM at $T = 19\,\mathrm{K}$ with $\omega_C = 1334.537\,\mathrm{meV}$ for measurement (top row), calculation with phase correction (middle row) and calculation without phase correction (bottom row). Colour scale indicates the phase from 0 to 2π.

4.7 SUMMARY

In this chapter, the dynamics of the strongly-coupled exciton-cavity system in a micropillar has been investigated. The JC Hamiltonian is used to described the system of a single QD coupled to a photon, while a triple QD-cavity system is modeled by TC Hamiltonian. A theory of FWM has been developed for N QDs coupled to the cavity. In both cases, only the GS, first rung $M_{1\pm}$ and second rung $M_{2\pm}$ are taken into account and used for the basis of the density matrix expansion. For the single QD-cavity system, the third-order polarization $P(\omega, \tau)$ shows the signals including the GS $\leftrightarrow M_{1\pm}$ and $M_{1\pm} \leftrightarrow M_{2\pm}$ transitions. Due to the faster decay of the $M_{2\pm}$ states, the $M_{1\pm} \leftrightarrow M_{2\pm}$ transitions can be suppressed in the FWM signal at the post-selected time $P(\omega, \tau; t > t_s)$. As a result, the vacuum Rabi splitting of GS $\leftrightarrow M_{1\pm}$ transitions are clearly seen as a doublet peak of the FWM signal. To reveal the quantum strong coupling effect, we access to the first and second rungs of the JC ladder separately. The coherent dynamics of GS $\leftrightarrow M_{1\pm}$ and GS $\leftrightarrow M_{2\pm}$ are probed using the different pulse order (positive and negative delays). The delay-time dependence for a positive (negative) delay is measuring the coherent evolution of the $M_{1\pm}$ ($M_{2\pm}$) states. It is found that the exponential decay for negative delays is faster than that for positive delays due to the larger photon content. The beat period is also shorter in the case of negative delays, corresponding to the larger polariton splitting ($\sqrt{2}g$) in the second rung of the ladder. This shows that the system is in quantum strong coupling regime.

Similar happens in the system of three exciton modes coupled to a cavity. The influence of each exciton mode depends on its detuning from the cavity. If the cavity is in resonance with one exciton, the resonant exciton has a strong contribution to the system and the other are less important. The coherent coupling is investigated by Fourier-transforming $P(\omega, \tau)$ going from the delay time (τ) domain to the conjugated frequency (ω_τ) domain, yielding $P(\omega, \omega_\tau)$. The off-diagonal peak of $|P(\omega, \omega_\tau)|$ demonstrates the coherent coupling of QDs which are isolated from each other. Finally, we compare our calculation with the measurement using a phase correction method. The comparison shows a quantitative agreement.

Chapter 5

Summary and Conclusions

5.1 DIRECT-TO-INDIRECT CROSSOVER OF QW EXCITONS IN AN ELECTRIC FIELD

An efficient method of calculation of exciton states in symmetric and asymmetric coupled quantum well (CQW) structure is presented in Chapter 2. In the model developed, the exciton wave function is expanded into a basis of uncorrelated pair which takes into account the ground and excited states of the electron and hole. The optical properties of excitonic states as function of the electric field applied in the growth direction are studied.

In the presence of the electric field, electrons and holes can tunnel through a thin barrier and form both direct and indirect excitons. The ground exciton state experiences a crossover from direct to indirect exciton at the electric field of $5\,\mathrm{kV/cm}$ which manifests itselt in decreasing binding energy and increasing exciton lifetime due to increasing spatial separation between electron and hole. The exciton lifetime consists of two components: the radiative and tunneling lifetimes. The radiative lifetime is dominant at low fields, while the tunneling channel is more significant at high fields when the tunneling rate increases because of the electric field. The calculated lifetime of the ground exciton state is in good agreement with the photoluminescence measurement. A large number of excited states is calculated, and the exciton excited

state having the maximum oscillator strength demonstrates a much weaker dependence on the electric field compared to the ground state. The exciton absorption spectra are also calculated.

The asymmetric CQW structure is also considered in this chapter. The physical picture and exciton properties are generally the same as in the case of the symmetric CQWs. However, the brightest decoupled exciton excited state observed in the symmetric case is not seen in the asymmetric one. Therefore, the studied asymmetric CQW is a good candidate for tunable light-matter interaction and various optoelectronic applications.

5.2 Light-matter coupling in CQW/microcavity systems and dipolaritons

In Chapter 3, the excitonic model developed and described in Chapter 2 is extended to include the polariton effect on the microscopic level. A large number of exciton states calculated in Chapter 2 is used there. The exciton-photon coupling is treated by solving coupled material and Maxwell's equations. For the microcavity layer containing asymmetric CQW, the excitonic susceptibility and dielectric function are calculated. The reflectivity and absorption spectra are also studied for different detunings and angles of light incidence using the scattering matrix approach. The reflectivity spectra demonstrate the clear anticrossings between two polariton states at different electric fields, indicating that the strong coupling regime is achieved. The advantage of this structure is that the on/off switching of the strong coupling can be controlled by the means of the electric field. A comparison between the calculated and experimental results is also presented, showing a good agreement.

The fractions of direct exciton, indirect exciton and cavity mode contributed to the polariton states are also studied. Dipolariton states in which all three components have comparable contributions are formed owing to exciton excited states and observed at different values of the electric field, between 10 and 15 kV/cm. At larger fields, the polariton states are mainly dominated by the indirect exciton, going to the

weak coupling regime. The polariton state containing only an indirect exciton and a photon with a vanishing contribution of direct exciton, i.e. a dark polariton, is not observed in CQW structures.

5.3 QUANTUM STRONG AND COHERENT COUPLINGS IN QD/MICROCAVITY SYSTEMS

Coherent dynamics of strongly-coupled exciton-cavity system - a quantum dot (QD) inside a micropillar cavity - is studied in Chapter 4. Theory of the four-wave mixing (FWM) in such a system is developed. The QD is treated as a two-level system and the exciton-photon interaction is described using the Jaynes-Cummings (JC) ladder. Spectrally and time-resolved FWM signals are calculated as functions of the temperature. The temperature is used to control the exciton-cavity mode detuning. To study the nonlinearities of the system, the first and second rungs of JC ladder are taken into account. They are addressed separately by using, respectively, positive and negative delays between laser pulses in the FWM. From the time-integrated FWM, it is found that the beat period of the second rung is faster than that of the first rung. This is because the energy splitting in the second rung is $\sqrt{2}$ larger than that in the first rung as zero detuning. This observation demonstrates that the system is in the quantum strong coupling regime.

In the three QDs-cavity system, coherent coupling of isolated QDs is investigated by fourier-transforming the FWM signal both in real and delay times. The diagonal and off-diagonal peaks are observed in a two dimensional frequency representation. The diagonal components are responsible for the first- and third-order polarization signal due to the same exciton. At the same time, the presence of the off-diagonal componentsin the 2D FWM spectra provides a proof of coherent coupling between different QDs which are spatially isolated and electronically decoupled.

Appendix A

Scattering Matrix method for planar systems

The scattering matrix approach was first proposed by Ko and Inkson [84], this method is developed in order to avoid the error accumulation due to exponential growing solutions dominating over exponentially small evanescent waves $e^{-i\mathrm{KL}}$ which appear in the transfer matrix T:

$$T = \begin{pmatrix} e^{i\mathrm{KL}} & 0 \\ 0 & e^{-i\mathrm{KL}} \end{pmatrix}. \tag{A.1}$$

Here K is the wavevector of light in the considered layer of width L. In the scattering matrix approach, the coefficient of the outgoing waves (A_N, B_0, see in Fig. A.1) are related to the coefficient of the incoming waves (A_0, B_N) via the scattering matrix $S_{0,N}$

$$\begin{pmatrix} \mathrm{A}_N \\ \mathrm{B}_0 \end{pmatrix} = S_{0,N} \begin{pmatrix} \mathrm{A}_0 \\ \mathrm{B}_N \end{pmatrix}. \tag{A.2}$$

To calculate the scattering matrix $S_{0,N}$, we start from the unit matrix $S_{0,0}$ for the first layer and then calculate the scattering matrices $S_{0,1}, S_{0,2}, \ldots, S_{0,N}$ iteratively. The scattering matrix $S_{0,n+1}$ is calculated from the scattering matrix $S_{0,n}$. Let us consider the interface between layer n and $n+1$ (see Fig A.1). Assuming that the
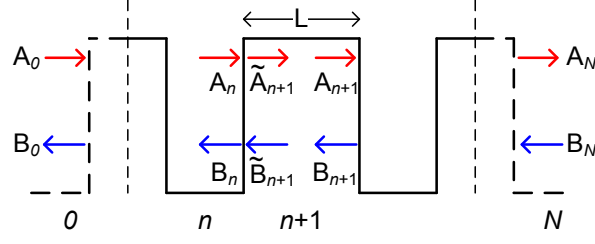
Figure A.1: Schematic diagram of an N-layer multilayer system.

scattering matrix $S_{0,n}$ is known and has a relationship as

$$\begin{pmatrix} A_n \\ B_0 \end{pmatrix} = S_{0,n} \begin{pmatrix} A_0 \\ B_n \end{pmatrix} = \begin{pmatrix} S_{11} & S_{12} \\ S_{21} & S_{22} \end{pmatrix} \begin{pmatrix} A_0 \\ B_n \end{pmatrix}. \tag{A.3}$$

At the interface, the relationship between coefficients A_n, B_n and $\tilde{A}_{n+1}, \tilde{B}_{n+1}$ obtained from the BCs which can be expressed in a matrix form as

$$\begin{pmatrix} A_n \\ B_n \end{pmatrix} = \begin{pmatrix} I_{11} & I_{12} \\ I_{21} & I_{22} \end{pmatrix} \begin{pmatrix} \tilde{A}_{n+1} \\ \tilde{B}_{n+1} \end{pmatrix}. \tag{A.4}$$

Rearranging Eq.(A.3) and Eq.(A.4), we get

$$\begin{pmatrix} \tilde{A}_{n+1} \\ B_0 \end{pmatrix} = \begin{pmatrix} DS_{11} & DE \\ S_{21} + S_{22}I_{21}DS_{11} & S_{22}I_{21}DE + S_{22}I_{22} \end{pmatrix} \begin{pmatrix} A_0 \\ \tilde{B}_{n+1} \end{pmatrix} \tag{A.5}$$

$$= \tilde{S}_{0,n+1} \begin{pmatrix} A_0 \\ \tilde{B}_{n+1} \end{pmatrix}, \tag{A.6}$$

where

$$D = (I_{11} - S_{12}I_{21})^{-1} \tag{A.7}$$

$$E = (S_{12}I_{22} - I_{12}) . \tag{A.8}$$

Similarly, the scattering matrix relationship over a distance L of layer $n+1$ is determined from Eq.(A.6) by substituting components

$$\begin{pmatrix} I_{11} & I_{12} \\ I_{21} & I_{22} \end{pmatrix} = \begin{pmatrix} e^{-i\mathrm{KL}} & 0 \\ 0 & e^{i\mathrm{KL}} \end{pmatrix}, \tag{A.9}$$

where K is the wave number of layer $n+1$. Finally, the scattering matrix $S_{0,n+1}$ is given by

$$S_{0,n+1} = \begin{pmatrix} e^{i\mathrm{KL}} & 0 \\ 0 & 1 \end{pmatrix} \tilde{S}_{0,n+1} \begin{pmatrix} 1 & 0 \\ 0 & e^{i\mathrm{KL}} \end{pmatrix}. \tag{A.10}$$

It is shown that there is no exponentially small component $e^{-i\mathrm{KL}}$ in the scattering matrix calculation, so that we can avoid the computational error problem which happens in the case of transfer matrix. In this work, the scattering matrix model is used to calculate the reflectivity and absorption spectra as presented in Chapter 3. The coefficients A and B in each layer can be calculated from the scattering matrix relationship (A.3) because the coefficients A_0 and B_0 are known.

Appendix B

Material equation for an exciton polariton

In this work, we concentrate on a planar microcavity structure with s-polarised light only. The material equation takes the form

$$\left(-\frac{\hbar^2}{2M}\nabla^2_{\mathrm{R_{xy}}} + H_{ex} + E_g - \hbar\omega - i\gamma\right)Y(\mathbf{r}, \mathbf{R}) = M(\mathbf{r})E(\mathbf{R}),\qquad\text{(B.1)}$$

where $\mathbf{r}$ and $\mathbf{R}$ are the relative and centre of mass coordinates respectively, H_{ex} is the exciton Hamiltonian, γ is the phenomenological parameter, $E(\mathbf{R})$ is the electric field, $Y(\mathbf{r}, \mathbf{R})$ is the microscopic excitonic polarization and $M(\mathbf{r}) = ed_{cv}\delta(\mathbf{r})$ is the microscopic dipole moment. This equation can be solved with the help of the Green's function satisfying

$$\left(-\frac{\hbar^2}{2M}\nabla^2_{\mathrm{R_{xy}}} + H_{ex}(z_e, z_h, \rho) + E_g - \hbar\omega - i\gamma\right)G(\mathbf{r}, \mathbf{r}', \mathbf{R}, \mathbf{R}'; \omega) = \delta(\mathbf{r}-\mathbf{r}')\delta(\mathbf{R}-\mathbf{R}').$$

$$\text{(B.2)}$$

Then,

$$Y(\mathbf{r}, \mathbf{R}) = \int\int G(\mathbf{r}, \mathbf{r}', \mathbf{R}, \mathbf{R}'; \omega)ed_{cv}\delta(\mathbf{r}')E(\mathbf{R}')d\mathbf{r}'d\mathbf{R}'.\qquad\text{(B.3)}$$

The spectral representation of Green's function has the form

$$G(\mathbf{r}, \mathbf{r}', \mathbf{R}, \mathbf{R}'; \omega) = \sum_{v}\frac{\Theta^*_v(\mathbf{r}', \mathbf{R}')\Theta_v(\mathbf{r}, \mathbf{R})}{E_\nu - \hbar\omega - i\gamma},\qquad\text{(B.4)}$$

where $\Theta_v(\mathbf{r}, \mathbf{R})$ is the eigenfunction of the Schrödinger equation

$$\left[-\frac{\hbar^2}{2M}\nabla^2_{\mathrm{R}_{\mathrm{xy}}} + H_{ex}(z_e, z_h, \rho) + E_g \right] \Theta_v(\mathbf{r}, \mathbf{R}) = E_\nu \Theta_v(\mathbf{r}, \mathbf{R}) \,. \tag{B.5}$$

The exciton Hamiltonian $H_{ex}(z_e, z_h, \rho)$ in Eq.(B.5) is solved in Chapter 2, the wave function is given by

$$\Theta_v(\mathbf{r}, \mathbf{R}) = \frac{e^{i\mathbf{Q}\cdot\mathbf{R}_{\mathrm{xy}}}}{\sqrt{\mathrm{S}}}\Psi_\nu(z_e, z_h, \rho) \,, \tag{B.6}$$

where the index $v = (\nu, \mathrm{Q})$ includes the exciton state ν and the quantum number Q, S is the QW area and the wave functions satisfy the following orthonormality relation

$$\int \Theta_v^*(\mathbf{r}, \mathbf{R})\Theta_\mu(\mathbf{r}, \mathbf{R})d\mathbf{r}d\mathbf{R} = \delta_{v\mu} \,. \tag{B.7}$$

Substituting $\Psi_v(\mathbf{r}, \mathbf{R})$ into Eq.(B.4), the Green's function takes the following form

$$G(\mathbf{r}, \mathbf{r}', \mathbf{R}, \mathbf{R}'; \omega) = \sum_{\mathrm{Q}} \frac{e^{i\mathbf{Q}\cdot(\mathbf{R}_{\mathrm{xy}} - \mathbf{R}'_{\mathrm{xy}})}}{\mathrm{S}} \sum_\nu \frac{\Psi_\nu(z_e, z_h, \rho)\Psi_\nu(z'_e, z'_h, \rho')}{E_\nu + \frac{\hbar^2 \mathrm{Q}^2}{2M} - \hbar\omega - i\gamma} \,. \tag{B.8}$$

The macroscopic polarization is given by

$$P(\mathbf{R}) = \int Y(\mathbf{r}, \mathbf{R})M(\mathbf{r})d\mathbf{r} \tag{B.9}$$

$$= \int \int \int G(\mathbf{r}, \mathbf{r}', \mathbf{R}, \mathbf{R}'; \omega)ed_{cv}\delta(\mathbf{r}')E(\mathbf{R}')ed_{cv}\delta(\mathbf{r})d\mathbf{r}'d\mathbf{R}'d\mathbf{r} \tag{B.10}$$

$$= e^2 d_{cv}^2 \int G(0, 0, \mathbf{R}, \mathbf{R}'; \omega)E(\mathbf{R}')d\mathbf{R}' \,. \tag{B.11}$$

Substituting Eq.(B.8) and assuming that the electric field has the form

$$E(\mathbf{R}) = \mathcal{E}(z)e^{i\mathbf{K}\cdot\mathbf{R}_{\mathrm{xy}}} \,, \tag{B.12}$$

where $\mathbf{K}$ is the in-plane wavevector, obtain

$$P(\mathbf{R}) = e^2 d_{cv}^2 \int \int \sum_{\mathrm{Q}} \frac{e^{i\mathbf{Q}\cdot(\mathbf{R}_{\mathrm{xy}} - \mathbf{R}'_{\mathrm{xy}})}}{\mathrm{S}}e^{i\mathbf{K}\cdot\mathbf{R}'_{\mathrm{xy}}}\mathcal{E}(z')\sum_\nu \frac{\Psi_\nu(z, z, 0)\Psi_\nu(z', z', 0)}{E_\nu + \frac{\hbar^2 \mathrm{Q}^2}{2M} - \hbar\omega - i\gamma}d\mathbf{R}'_{\mathrm{xy}}dz' \,. \tag{B.13}$$

Since $\int e^{i\mathbf{K}\cdot\mathbf{R}'_{xy}}e^{-i\mathbf{Q}\cdot\mathbf{R}'_{xy}}d\mathbf{R}'_{xy} = S\delta_{\mathbf{K},\mathbf{Q}}$,

$$P(\mathbf{R}) = e^2 d_{cv}^2 e^{i\mathbf{K}\cdot\mathbf{R}_{xy}} \int \mathcal{E}(z') \sum_\nu \frac{\Psi_\nu(z,z,0)\Psi_\nu(z',z',0)}{E_\nu + \frac{\hbar^2\mathrm{K}^2}{2M} - \hbar\omega - i\gamma}dz'. \tag{B.14}$$

From the definition of the polarization in Eq.(3.8), we can rewrite Eq.(B.14) as

$$P(\mathbf{R}) = e^{i\mathbf{K}\cdot\mathbf{R}_{xy}} \int \mathcal{E}(z')\chi(z,z';\mathrm{K},\omega)dz', \tag{B.15}$$

with

$$\chi(z,z';\mathrm{K},\omega) = e^2 d_{cv}^2 \sum_\nu \frac{\Psi_\nu(z,z,0)\Psi_\nu(z',z',0)}{E_\nu + \frac{\hbar^2\mathrm{K}^2}{2M} - \hbar\omega - i\gamma}. \tag{B.16}$$

The wave function $\psi_\nu(z,z,0)$ is zero outside the well, so that we can replace

$$\Psi_\nu(z,z,0) = A_\nu\delta(z), \tag{B.17}$$

where

$$A_\nu = \int_{-\infty}^{\infty} \Psi_\nu(z,z,0)dz. \tag{B.18}$$

and

$$\delta(z) = \begin{cases} 1/d & \text{inside the wells,} \\ 0 & \text{outside,} \end{cases} \tag{B.19}$$

and d is the well width. Therefore, a nonlocal susceptibility $\chi(z,z';\mathrm{K},\omega)$ in Eq.(B.16) is z-independent and called a local susceptibility

$$\chi(\mathrm{K},\omega) = \frac{e^2 d_{cv}^2}{d} \sum_\nu \frac{|A_\nu|^2}{E_\nu + \frac{\hbar^2\mathrm{K}^2}{2M} - \hbar\omega - i\gamma} \tag{B.20}$$

The local susceptibility is used to calculate the dielectric function which is used in the scattering matrix method to compute the reflectivity and absorption spectra. Using the local susceptibility does not make a significant difference compared to the calculation of dielectric using the nonlocal susceptibility, the difference is less than a few percent, because the CQW width is small compared to the cavity mode wavelength. The main aim of using the local susceptibility is to simplify the model. Nevertheless,

we develop both local and non-local approaches, in order to make our calculation applicable to arbitrary QW microcavity structures. The non-local approach is described in detail in Appendix C.

Appendix C

Non-local approach to the CQW/microcavity system

The Maxwell's equation for the s-polarised light has the form

$$\left(K^2 - \frac{d^2}{dz^2}\right)\mathcal{E}(z) = \frac{\omega^2}{c^2}\left[\epsilon_b(z)\mathcal{E}(z) + 4\pi\int_{-\infty}^{\infty}\chi(z,z';K,\omega)\mathcal{E}(z')dz'\right], \qquad (C.1)$$

where K is the in-plane wavevector ($K \neq 0$ for non-normal incidence of light), ω is the light frequency, ϵ_b is the background dielectric constant. The background dielectric constant inside the cavity layer containing CQWs is z-dependent, but it changes by a few percent only (3 percent for our studied structure). Therefore, we assume that $\epsilon_b(z) = \epsilon_b$ is constant everywhere in the cavity layers. The nonlocal susceptibility $\chi(z, z'; K, \omega)$ has the form

$$\chi(z, z'; K, \omega) = e^2 d_{cv}^2 \sum_\nu \frac{\Psi_\nu(z, z, 0)\Psi_\nu(z', z', 0)}{E_\nu + \frac{\hbar^2 K^2}{2M_X} - \hbar\omega - i\gamma}, \qquad (C.2)$$

where γ is a phenomenological exciton damping constant and d_{cv} is the dipole moment. The exciton wave function $\psi_\nu(z_e, z_h, \rho)$ calculated in Chapter 2 is expanded as

$$\Psi_\nu(z_e, z_h, \rho) = \sum_n \Phi_n(z_e, z_h)\phi_{n\nu}(\rho). \qquad (C.3)$$

Let's introduce

$$Q(z, z') = -4\pi \frac{\omega^2}{c^2} \chi(z, z'; K, \omega) . \tag{C.4}$$

Due to the form of the exciton wave function, $Q(z, z')$ is factorisable as

$$Q(z, z') = \sum_n \sum_m \Phi_n(z, z) \Phi_m(z', z') Q_{nm} \tag{C.5}$$

with

$$Q_{nm} = -4\pi \frac{\omega^2}{c^2} e^2 d_{cv}^2 \frac{\phi_{n\nu}(0)\phi_{m\nu}(0)}{E_\nu + \frac{\hbar^2 K^2}{2M_X} - \hbar\omega - i\gamma} \tag{C.6}$$

Maxwell's equation in Eq.(C.1) then takes the form

$$\left(\frac{d^2}{dz^2} + q^2 \right) \mathcal{E}(z) = \int_{-\infty}^{\infty} Q(z, z') \mathcal{E}(z') dz' . \tag{C.7}$$

where $q^2 = \frac{\omega^2}{c^2} \epsilon_b - K^2$. Let us solve this equation with the help of the Green's function, satisfying

$$\left(\frac{d^2}{dz^2} + q^2 \right) G(z, z') = \delta(z - z') . \tag{C.8}$$

The Green's function satisfying outgoing boundary conditions and the above equation has the form

$$G(z, z') = \frac{e^{iq|z-z'|}}{2iq} . \tag{C.9}$$

Then Eq.(C.7) is solved as follows

$$\mathcal{E}(z) = Ae^{iqz} + Be^{-iqz} + \int_{-\infty}^{\infty} \int_{-\infty}^{\infty} G(z, z') Q(z', z'') \mathcal{E}(z'') \, dz' dz'' . \tag{C.10}$$

Introducing

$$X_n = \int_{-\infty}^{\infty} \mathcal{E}(z) \Phi_n(z, z) dz \tag{C.11}$$

and

$$\tilde{\Phi}_n(q) = \int_{-\infty}^{\infty} e^{iqz} \Phi_n(z, z) dz , \tag{C.12}$$

Eq.(C.10) becomes

$$\mathcal{E}(z) = Ae^{iqz} + Be^{-iqz} + \sum_{nm} \int_{-\infty}^{\infty} G(z, z')\Phi_n(z', z)Q_{nm}X_m \, dz' \,. \tag{C.13}$$

Multiplying by $\Phi_n(z, z)$ and integrating over z, we get

$$X_n = A\tilde{\Phi}_n(q) + B\tilde{\Phi}_n(-q) + \sum_{ml} G_{nm}Q_{ml}X_l \,, \tag{C.14}$$

where

$$G_{nm} = \int_{-\infty}^{\infty} \int_{-\infty}^{\infty} G(z, z')\Phi(z, z)\Phi(z', z') \, dz \, dz' \,. \tag{C.15}$$

Then Eq.(C.14) is simplified to

$$\sum_m (\delta_{nm} - V_{nm}) X_m = A\tilde{\Phi}_n(q) + B\tilde{\Phi}_n(-q) \,, \tag{C.16}$$

by introducing a matrix V_{nm} as

$$V_{nm} = \sum_l G_{nl}Q_{lm} \,. \tag{C.17}$$

The coefficients A and B in Eq.(C.16) are calculated using the scattering matrix method (see in Apendix A). The function X_n is then found as a solution of matrix equation(C.16). It is used in the calculation of the contribution of DX, IX, and C modes in the CQW/microcavity structure described in Chapter 3.

Appendix D

Theory of the FWM in a QD/microcavity system

The dynamics of an exciton in a QD strongly coupled to a single photonic cavity mode in a micropillar is described by the Jaynes-Cumming (JC) model. The four-wave-mixing (FWM) dynamics can be calculated using the density matrix formalism. The master equation for the density matrix $\rho(t)$ has the form

$$i\frac{d\rho}{dt} = \hat{\mathcal{L}}(t)\rho\,. \tag{D.1}$$

The full time dependent Lindblad super-operator $\hat{\mathcal{L}}(t)$ can be written as

$$\hat{\mathcal{L}}(t)\rho = \hat{L}\rho + [V(t), \rho]\,, \tag{D.2}$$

$$\hat{L}\rho = [H, \rho] - i\gamma_c\left(a^\dagger a\rho + \rho a^\dagger a - 2a\rho a^\dagger\right)$$

$$-i\gamma_x\left(\left|1\right\rangle\left\langle1\right|\rho + \rho\left|1\right\rangle\left\langle1\right| - 2\left|0\right\rangle\left\langle1\right|\rho\left|1\right\rangle\left\langle0\right|\right) \tag{D.3}$$

where $\hat{L}$ is a time-independent operator, $\gamma_c(\gamma_x)$ is the cavity (exciton) linewidth of radiative decay and $V(t)$ is the coupling of the cavity mode to the external continuum of photonic states described by a classical electric field $\mathcal{E}(t)$, has the form

$$V(t) = \begin{cases} V_1\delta(t+\tau) + V_2\delta(t) & \tau > 0 \\ V_1\delta(t) + V_2\delta(t-\tau) & \tau < 0 \end{cases} \tag{D.4}$$

with

$$V_i = \mu\mathcal{E}_i a^\dagger + \mu\mathcal{E}_i^* a, \quad i = 1, 2 \tag{D.5}$$

where μ is the effective dipole moment of the cavity mode and the observation time t is measured from the time of the latest pulse. Note that the effect of the two pulses $[\mathcal{E}_1, \mathcal{E}_2]$ and the time-independent Lindblad operator in Eq.(D.3) can be calculated explicitly in the following way.

For a positive delay $[\tau > 0$, see Fig. D.1(a)], pulse $\mathcal{E}_1$ comes first, changing the density matrix according to

$$\rho^+ = -i\mu\mathcal{E}_1^*[a, \rho^-], \tag{D.6}$$

where ρ^+ and ρ^- are the density matrix before and after the pulse respectively. The time evolution of the density matrix for a delay time τ is then calculated by

$$i\frac{d\rho}{dt} = \hat{L}\rho \tag{D.7}$$

$$\rho^{(1)}(\tau) = e^{-i\hat{L}\tau}\rho^{(1)}(0), \tag{D.8}$$

where $\rho^{(1)}(\tau)$ is the first-order component of the density matrix.
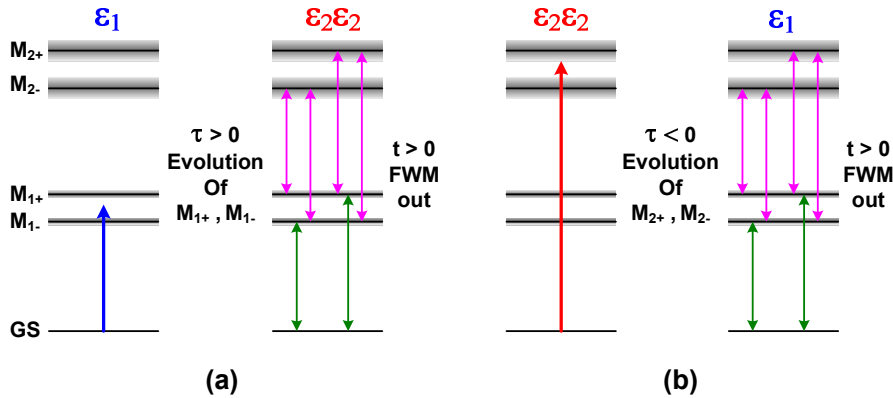
Figure D.1: FWM creation pathways of order $\mathcal{E}_1^*\mathcal{E}_2^2$ within the JC ladder for different time ordering of the excitation pulses: (a) pulse $\mathcal{E}_1^*$ arrives first for $\tau > 0$ and (b) pulse $\mathcal{E}_2^*$ arrives first for $\tau < 0$.

After a delay time τ, the arrival of pulse $\mathcal{E}_2$ results in the following change of the density matrix

$$\rho^+ = \frac{(-i)^2}{2}\mu^2\mathcal{E}_2^2[a^\dagger,[a^\dagger,\rho^-]]\,. \tag{D.9}$$

Then, the time evolution of the density matrix after the second pulse is

$$\rho^{(3)}(t) = e^{-i\hat{L}t}\rho^{(3)}(0)\,. \tag{D.10}$$

Finally, the third-order component of density matrix for the positive delay takes the form

$$\rho^{(3)}(t) = \left(\frac{(-i)^3}{2}\mu^3\mathcal{E}_1^*\mathcal{E}_2^2\right)e^{-i\hat{L}t}[a^\dagger,[a^\dagger,e^{-i\hat{L}\tau}[a,\rho^{(0)}]]]\,, \tag{D.11}$$

where $\rho^{(0)}$ is the density matrix of the system before the two pulses.

For a negative delay [$\tau < 0$, see Fig. D.1(b)], pulse $\mathcal{E}_2$ arrives first and is followed by the pulse $\mathcal{E}_1$ after a delay time τ. The third-order component of the density matrix has the form

$$\rho^{(3)}(t) = \left(\frac{(-i)^3}{2}\mu^3\mathcal{E}_1^*\mathcal{E}_2^2\right)e^{-i\hat{L}t}[a,e^{-i\hat{L}\tau}[a^\dagger,[a^\dagger,\rho^{(0)}]]]\,. \tag{D.12}$$

The FWM polarization has the form

$$P_{\text{FWM}}^{(3)}(t) = \text{Tr}\left\{\rho^{(3)}(t)a\right\}\,. \tag{D.13}$$

To calculate the density matrix in Eq.(D.11)-(D.12), we first expand all operator into a set of uncoupled exciton-photon state $|i\rangle \equiv |n_X, n_C\rangle$ $(i = 0, 1, 2, \ldots)$. The exciton occupation number n_X is 0 for unexcited exciton and 1 for excited exciton, while the photon occupation number $n_C = 0, 1, 2, \ldots$etc. We assume that the system is initially in the GS with the density matrix $\rho^{(0)} = |0\rangle\langle 0|$. In this calculation, we consider only transitions between the GS, the first rung and the second rung of the LC ladder. This is enough since we study the third-order polarization. Then the basis is reduced to five states, including the GS, two states in the first rung and two states in the second rung (Fig. D.2). The six possible transitions consists of two transitions
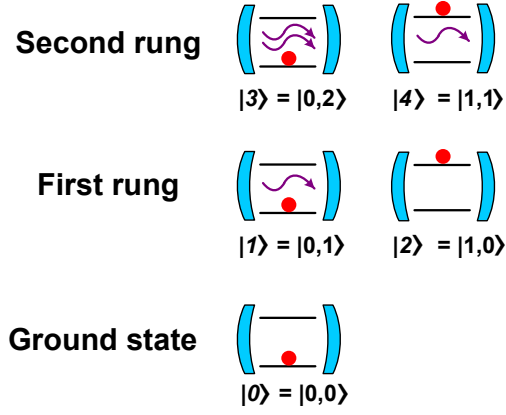
Figure D.2: The basis of five states in the JC ladder consists of GS, two states in the first rung and two states in the second rung.

of GS $\leftrightarrow$ M$_{1\pm}$, and four transitions of M$_{1\pm}$ $\leftrightarrow$ M$_{2\pm}$. The density matrix has the form

$$\rho(t) = \sum_{i,j=0}^{4} \rho_{ij}(t) \left|i\right\rangle \left\langle j\right| , \tag{D.14}$$

The solution of the master equation can be written in a matrix form

$$\rho(t) = e^{-i\hat{L}t}\rho(0) = \hat{U}e^{-i\hat{\Omega}t}\hat{V}\rho(0) , \tag{D.15}$$

where the matrix $\hat{L}$ is diagonalised as

$$\hat{L} = \hat{U}\hat{\Omega}\hat{V}, \ \hat{U}\hat{V} = 1 , \tag{D.16}$$

with $\hat{U}$ and $\hat{V}$ being matrices of right and left eigenvectors and $\hat{\Omega}$ a diagonal matrix of complex eigenfrequencies $\tilde{\omega}_j$. The FWM polarization then has the form

$$P_{\text{FWM}}^{(3)}(t,\tau) = \sum_{j=1}^{6} A_j(\tau)e^{-i\tilde{\omega}_j t} . \tag{D.17}$$

122

The complex frequency $\tilde{\omega}_j$ is given by

$$
\begin{aligned}
\tilde{\omega}_1 &= \lambda_{1+} & \tilde{\omega}_2 &= \lambda_{1-} \\
\tilde{\omega}_3 &= \lambda_{2+} - \lambda_{1+}^* & \tilde{\omega}_4 &= \lambda_{2-} - \lambda_{1-}^* \\
\tilde{\omega}_5 &= \lambda_{2+} - \lambda_{1-}^* & \tilde{\omega}_6 &= \lambda_{2-} - \lambda_{1+}^*
\end{aligned}
\tag{D.18}
$$

where

$$
\lambda_{n\pm} = \frac{(2n-1)(\omega_C - i\gamma_C) + (\omega_X - i\gamma_X)}{2} \pm \sqrt{\left(\frac{\omega_C - i\gamma_C - \omega_X + i\gamma_X}{2}\right)^2 + ng^2},
\tag{D.19}
$$

The amplitude A_j is calculated explicitly from the master equation with the super-operator $\hat{L}$ in a matrix form.

Bibliography

[1] C. C. Phillips, R. Eccleston, and S. R. Andrews, "Theoretical and experimental picosecond photoluminescence studies of the quantum-confined Stark effect in a strongly coupled double-quantum-well structure," *Phys. Rev. B*, vol. 40, p. 9760, 1989.

[2] S. C. Arapan and M. A. Liberman, "Exciton levels and optical absorption in coupled double quantum well structures," *J. Lumin.*, vol. 112, p. 216, 2005.

[3] S. Charbonneau, M. L. W. Thewalt, E. S. Koteles, and B. Elman, "Transformation of spatially direct to spatially indirect excitons in coupled couble quantum wells," *Phys. Rev. B*, vol. 38, p. 6287, 1988.

[4] J. E. Golub, K. Kash, J. P. Harbison, and L. T. Florez, "Long-lived spatially indirect excitons in coupled $GaAs/Al_xGa_{1-x}As$ quantum wells," *Phys. Rev. B*, vol. 41, p. 8564, 1990.

[5] A. Alexandrou, J. A. Kash, E. E. Mendez, M. Zachau, J. M. Hong, T. Fukuzawa, and Y. Hase, "Electric-field effects on exciton lifetimes in symmetric $GaAs/Al_{0.3}Ga_{0.7}As$ coupled double quantum wells," *Phys. Rev. B*, vol. 42, p. 9225, 1990.

[6] J. J. Hopfield, "Theory of the Contribution of Excitons to the Complex Dielectric Constant of Crystals," *Phys. Rev.*, vol. 112, p. 1555, 1958.

[7] J. J. Hopfield and D. G. Thomas, "Polariton absorption lines," *Phys. Rev. Lett.*, vol. 15, p. 22, 1965.

[8] J. J. Hopfield, "Resonant Scattering of Polaritons as Composite Particles," *Phys. Rev.*, vol. 182, p. 945, 1969.

[9] Y. Kaluzny, P. Goy, M. Gross, J. M. Raimond, and S. Haroche, "Observation of self-induced rabi oscillations in two-level atoms excited inside a resonant cavity: The ringing regime of superradiance," *Phys. Rev. Lett.*, vol. 51, p. 1175, 1983.

[10] M. S. Skolnick, T. A. Fisher, and D. M. Whittaker, "Strong coupling phenomena in quantum microcavity structures," *Semicond. Sci. Technol.*, vol. 13, p. 645, 1998.

[11] G. Khitrova, H. M. Gibbs, F. Jahnke, M. Kira, and S. W. Koch, "Nonlinear optics of normal-mode-coupling semiconductor microcavities," *Rev. Mod. Phys.*, vol. 71, p. 1591, 1999.

[12] A. Kavokin, "Exciton-polaritons in microcavities: present and future," *Appl. Phys. A*, vol. 89, p. 241, 2007.

[13] A. Kavokin, "Exciton-polaritons in microcavities: Recent discoveries and perspectives," *Phys. Status Solidi B*, vol. 247, p. 1898, 2010.

[14] H. Deng, H. Haug, and Y. Yamamoto, "Exciton-polariton Bose-Einstein condensation," *Rev. Mod. Phys.*, vol. 82, p. 1489, 2010.

[15] C. Weisbuch, M. Nishioka, A. Ishikawa, and Y. Arakawa, "Observation of the Coupled Exciton-Photon Mode Splitting in a Semiconductor Quantum Microcavity," *Phys. Rev. Lett.*, vol. 69, p. 3314, 1992.

[16] J. M. Fink, M. Göppl, M. Baur, R. Bianchetti, P. J. Leek, A. Blais, and A. Wallraff, "Climbing the Jaynes-Cummings ladder and observing its $\sqrt{n}$ nonlinearity in a cavity qed system," *Nature*, vol. 454, p. 315, 2008.

[17] R. J. Schoelkopf and S. M. Girvin, "Wiring up quantum systems," *Nature*, vol. 451, p. 81, 2008.

125

[18] E. Peter, P. Senellart, D. Martrou, A. Lemaître, J. Hours, J. M. Gérard, and J. Bloch, "Exciton-Photon Strong-Coupling Regime for a Single Quantum Dot Embedded in a Microcavity," *Phys. Rev. Lett.*, vol. 95, p. 067401, 2005.

[19] K. Hennessy, A. Badolato, M. Winger, D. Gerace, M. Atatüre, S. Gulde, S. Fält, E. L. Hu, and A. Imamoğlu, "Quantum nature of a strongly coupled single quantum dot-cavity system," *Nature*, vol. 445, p. 896, 2007.

[20] T. Yoshie, A. Scherer, J. Hendrickson, G. Khitrova, H. M. Gibbs, G. Rupper, C. Ell, O. B. Shchekin, and D. G. Deppe, "Vacuum Rabi splitting with a single quantum dot in a photonic crystal nanocavity," *Nature*, vol. 432, p. 200, 2004.

[21] G. Khitrova, H. M. Gibbs, M. Kira, S. W. Koch, and A. Scherer, "Vacuum Rabi splitting in semiconductors," *Nature Physics*, vol. 2, p. 81, 2006.

[22] J. Kasprzak, S. Reitzenstein, E. A. Muljarov, C. Kistner, C. Schneider, M. Strauß, S. Höfling, A. Forchel, and W. Langbein, "Up on the Jaynes-Cummings ladder of a quantum-dot/microcavity system," *Nature Mater.*, vol. 9, p. 304, 2010.

[23] J. P. Reithmaier, G. Sek, A. Löffler, C. Hofmann, S. Kuhn, S. Reitzenstein, L. V. Keldysh, V. D. Kulakovskii, T. L. Reinecke, and A. Forchel, "Strong coupling in a single quantum dot-semiconductor microcavity system," *Nature*, vol. 432, p. 197, 2004.

[24] L. V. Butov, A. Imamoglu, A. V. Mintsev, K. L. Campman, and A. C. Gossard, "Photoluminescence kinetics of indirect excitons in $GaAs/Al_xGa_{1-x}As$ coupled quantum wells," *Phys. Rev. B*, vol. 59, p. 1625, 1999.

[25] Y. J. Chen, E. S. Koteles, B. S. Elman, and C. A. Armiento, "Effect of electric fields on excitons in a coupled double-quantum-well structure," *Phys. Rev. B*, vol. 36, p. 4562, 1987.

[26] Y. Tokuda, K. Kanamoto, N. Tsukada, and T. Nakayama, "Distinct observation of interwell coupling effect on optical transitions in double quantum wells in an electric field," *Appl. Phys. Lett.*, vol. 54, p. 1232, 1989.

[27] S. R. Andrews, C. M. Murray, R. A. Davies, and T. M. Kerr, "Stark effect in strongly coupled quantum wells," *Phys. Rev. B*, vol. 37, p. 8198, 1988.

[28] M. H. Szymanska and P. B. Littlewood, "Excitonic binding in coupled quantum wells," *Phys. Rev. B*, vol. 67, p. 193305, 2003.

[29] J. H. Kim, T. W. Kim, and K. H. Yoo, "Interband Stark effects in $In_xGa_{1-x}As/In_yGa_{1-y}As$ coupled step quantum wells," *Appl. Surf. Sci.*, vol. 240, p. 452, 2005.

[30] C. Kittel, *Introduction to Solid State Physics*. Wiley, 1996.

[31] E. M. Purcell, "Spontaneous emission probabilities at radio frequencies," *Phys. Rev.*, vol. 69, p. 681, 1946.

[32] R. Ohta, Y. Ota, M. Nomura, N. Kumagai, S. Ishida, S. Iwamoto, and Y. Arakawa, "Strong coupling between a photonic crystal nanobeam cavity and a single quantum dot," *Appl. Phys. Lett.*, vol. 98, p. 173104, 2011.

[33] J. A. Kash, E. E. Mendez, and H. Morkoç, "Electric field induced decrease of photoluminescence lifetime in GaAs quantum wells," *Appl. Phys. Lett.*, vol. 46, p. 173, 1985.

[34] H.-J. Polland, L. Schultheis, J. Kuhl, E. O. Göbel, and C. W. Tu, "Lifetime Enhancement of Two-Dimensional Excitons by the Quantum-Confined Stark Effect," *Phys. Rev. Lett.*, vol. 55, p. 2610, 1985.

[35] E. J. Austin and M. Jaros, "Electric field induced shifts and lifetimes in GaAs-GaAlAs quantum wells," *Appl. Phys. Lett.*, vol. 47, p. 274, 1985.

[36] D. A. B. Miller, D. S. Chemla, T. C. Damen, A. C. Gossard, W. Wiegmann, T. H. Wood, and C. A. Burus, "Electric field dependence of optical absorption near the band gap of quantum-well structures," *Phys. Rev. B*, vol. 32, p. 1043, 1985.

[37] F. Borondo and J. Sánchez-Dehesa, "Electronic structure of a GaAs quantum well in an electric field," *Phys. Rev. B*, vol. 33, p. 8758, 1986.

[38] D. Ahn and S. L. Chuang, "Exact calculations of quasibound states of an isolated quantum well with uniform electric field: Quantum-well Stark resonance," *Phys. Rev. B*, vol. 34, p. 9034, 1986.

[39] D.-S. Chuu and Y.-T. Shih, "Exciton binding energy in a GaAs/Al$_x$Ga$_{1-x}$As quantum well with uniform electric field," *Phys. Rev. B*, vol. 44, p. 8054, 1991.

[40] G. Bastard, E. E. Mendez, L. L. Chang, and L. Esaki, "Exciton binding energy in quantum wells," *Phys. Rev. B*, vol. 26, p. 1974, 1982.

[41] R. L. Greene, K. K. Bajaj, and D. E. Phelps, "Energy levels of Wannier excitons in GaAs $-$ Ga$_{1-x}$Al$_x$As quantum-well structures," *Phys. Rev. B*, vol. 29, p. 1807, 1984.

[42] J. Lee, M. O. Vassell, E. S. Koteles, and B. Elman, "Excitonic spectra of asymmetric, coupled doubble quantum wells in electric fields," *Phys. Rev. B*, vol. 39, p. 10133, 1989.

[43] T. Kamizato and M. Matsuura, "Excitons in double quantum wells," *Phys. Rev. B*, vol. 40, p. 8378, 1989.

[44] M. M. Dignam and J. E. Sipe, "Exciton states in coupled double quantum wells in a static electric field," *Phys. Rev. B*, vol. 43, p. 4084, 1991.

[45] T. Westgaard, Q. X. Zhao, B. O. Fimland, K. Johannessen, and L. Johnsen, "Optical properties of excitons in GaAs/Al$_{0.3}$Ga$_{0.7}$As symmetric double quantum wells," *Phys. Rev. B*, vol. 45, p. 1784, 1992.

[46] I. Linnerud and K. A. Chao, "Exciton binding energies and oscillator strengths in a symmetric Al$_x$Ga$_{1-x}$As/GaAs double quantum well," *Phys. Rev. B*, vol. 49, p. 8487, 1994.

[47] Y. Takahashi, Y. Kato, S. S. Kano, S. Fukatsu, Y. Shiraki, and R. Ito, "The effect of electric field on the excitonic states in coupled quantum well structures," *J. Appl. Phys.*, vol. 76, p. 2299, 1994.

[48] C. Monier, A. Freundlich, and M. F. Vilela, "Oscillator strength of excitons in (In, Ga)As/GaAs quantum wells in the presence of a large electric field," *J. Appl. Phys.*, vol. 85, p. 2713, 1999.

[49] J. Soubusta, R. Grill, P. Hlídek, M. Zvára, L. Smrčka, S. Malzer, W. G. elbrecht, and G. H. Döhler, "Excitonic photoluminescence in symmetric coupled double quantum wells subject to an external electric field," *Phys. Rev. B*, vol. 60, p. 7740, 1999.

[50] S. de Leon and B. Laikhtman, "Exciton wave function, binding energy, and lifetime in InAs/GaSb coupled quantum wells," *Phys. Rev. B*, vol. 61, p. 2874, 2000.

[51] I. V. Ponomarev, L. I. Deych, V. A. Shuvayev, and A. A. Lisyansky, "Self-consistent approach for calculations of exciton binding energy in quantum wells," *Physica E*, vol. 25, p. 539, 2005.

[52] K. Sivalertporn, L. Mouchliadis, A. L. Ivanov, R. Philp, and E. A. Muljarov, "Direct and indirect excitons in semiconductor coupled quantum wells in an applied electric field," *Phys. Rev. B*, vol. 85, p. 045207, 2012.

[53] W. Trzeciakowski and M. Gurioli, "Electric-field effects in semiconductor quantum wells," *Phys. Rev. B*, vol. 44, p. 3880, 1991.

[54] D. M.-T. Kuo and Y.-C. Chang, "Intersubband electroabsorption spectra of semiconductor quantum wells," *J. Appl. Phys.*, vol. 87, p. 2936, 2000.

[55] J. H. Davies, *The Physics of Low-Dimensional Semiconductors*. Oxford University Press, 1998.

[56] I. Galbraith and G. Duggan, "Exciton binding energy and external-field-induced blue shift in double quantum wells," *Phys. Rev. B*, vol. 40, p. 5515, 1989.

[57] D. Campi and C. Alibert, "Optical blue shift in a double quantum well structure under an electric field," *Appl. Phys. Lett.*, vol. 55, p. 454, 1989.

[58] K. Sivalertporn, L. Mouchliadis, A. L. Ivanov, R. Philp, and E. A. Muljarov, "http://cqwexciton.cf.ac.uk."

[59] L. V. Butov, C. W. Lai, A. L. Ivanov, A. C. Gossard, , and D. S. Chemla, "Towards Bose-Einstein condensation of excitons in potential traps," *Nature*, vol. 417, p. 47, 2002.

[60] L. V. Butov, C. W. Lai, A. L. Ivanov, A. C. Gossard, , and D. S. Chemla, "Microscopically ordered state in an exciton system," *Nature*, vol. 418, p. 751, 2002.

[61] P. Cristofolini, G. Christmann, S. I. Tsintzos, G. Deligeorgis, G. Konstantinidis, Z. Hatzopoulos, P. G. Savvidis, and J. J. Baumberg, "Coupling Quantum Tunneling with Cavity Photons," *Science*, vol. 336, p. 704, 2012.

[62] G. Christmann, A. Askitopoulos, G. Deligeorgis, Z. Hatzopoulos, S. I. Tsintzos, P. G. Savvidis, and J. J. Baumberg, "Oriented polaritons in strongly-coupled asymmetric double quantum well microcavities," *Appl. Phys. Lett.*, vol. 98, p. 081111, 2011.

[63] G. Christmann, C. Coulson, J. J. Baumberg, N. T. Pelekanos, Z. Hatzopoulos, S. I.Tsintzos, and P. G. Savvidis, "Control of polariton scattering in resonant-tunneling double-quantum-well semiconductor microcavities," *Phys. Rev. B*, vol. 82, p. 113308, 2010.

[64] G. Christmann, R. Butté, E. Feltin, J.-F. Carlin, and N. Grandjean, "Room temperature polariton lasing in a GaN/AlGaN mutiple quantum well microcavity," *Appl. Phys. Lett.*, vol. 93, p. 051102, 2008.

[65] J. Leymarie, C. Monier, A. Vasson, A.-M. Vasson, M. Leroux, B. Courboulès, N. Grandjean, C. Deparis, and J. Massies, "Optical investigations in (In,Ga)As/GaAs quantum wells grown by metalorganic molecular-beam epitaxy," *Phys. Rev. B*, vol. 51, p. 13274, 1995.

[66] M. Levinshtein, S. Rumyantsev, and M. Shur, *Handbook series on Semiconductor Parameters*. World Scientific Publishing, 1996.

[67] L. W. Molenkamp, R. Eppenga, G. W. Hooft, P. Dawson, C. T. Foxon, and K. J. Moore, "Determination of valence-band effective-mass anisotropy in GaAs quantum wells by optical spectroscopy," *Phys. Rev. B*, vol. 38, p. 4314, 1988.

[68] H. Q. Hou, Y. Segawa, Y. Aoyagi, S. Namba, and J. M. Zhou, "Exciton binding energy in $In_xGa_{1-x}As/GaAs$ strained quantum wells," *Phys. Rev. B*, vol. 42, p. 1284, 1990.

[69] E. Rosencher and B. Vinter, *Optoelectronics*. Cambridge University Press, 2002.

[70] P. G. Eliseev, H. Li, A. Stintz, G. T. Liu, T. C. Newell, K. J. Malloy, and L. F. Lester, "Transition dipole moment of InAs/InGaAs quantum dots from experiments on ultralow-threshold laser diodes," *Appl. Phys. Lett.*, vol. 77, p. 262, 2000.

[71] M. Abramowitz and I. A. Stegun, *Handbook of Mathematical Functions (with Formulas, Graphs, and Mathematical Tables)*. Dover Publications, 1965.

[72] C. Weisbuch and B. Vinter, *Quantum semiconductor structures: funcdamentals and applications*. Academic Press, 1991.

[73] A. J. F. Siegert, "Excitonic switches operating at around 100K," *Phys. Rev.*, vol. 56, p. 750, 1939.

[74] R. M. More, "Theory of Decaying States," *Phys. Rev. A*, vol. 4, p. 1782, 1971.

[75] L. C. Andreani, *Confined electrons and photons: new physics and applications*. Plenum Press, 1995.

[76] L. C. Andreani, "Radiative lifetime of free excitons in quantum wells," *Solid State Commun.*, vol. 77, p. 641, 1991.

[77] V. Srinivas, J. Hryniewicz, Y. J. Chen, and C. E. C. Wool, "Intrinsic linewidths and radiative lifetimes of free excitons in GaAs quantum wells," *Phys. Rev. B*, vol. 46, p. 10193, 1992.

[78] R. J. Elliott, "Intensity of Optical Absorption by Excitons," *Phys. Rev.*, vol. 108, p. 1384, 1957.

[79] L. C. Andreani, G. Panzarini, A. V. Kavokin, and M. R. Vladimirova, "Effect of inhomogeneous broadening on optical properties of excitons in quantum wells," *Phys. Rev. B*, vol. 57, p. 4670, 1998.

[80] K. Sivalertporn and E. A. Muljarov, "Strong and weak light-matter coupling in microcavity-embedded double quantum wells," *ArXiv: 1305.5883*, 2013.

[81] K. Huang, "On the interaction between the radiation field and ionic crystals," *Proc. R. Soc. London, Ser. A*, vol. 208, p. 352, 1951.

[82] M. Born and K. Huang, *Dynamical theory of crystal lattices*. Clarendon Press, 1954.

[83] E. A. Muljarov and R. Zimmermann, "Exciton polariton including continuum states: Microscopic versus additonal boundary conditions," *Phys. Rev. B*, vol. 66, p. 235319, 2002.

[84] D. Y. K. Ko and J. C. Inkson, "Matrix method for tunneling in heterostructures: Resonant tunneling in multilayer systems," *Phys. Rev. B*, vol. 38, p. 9945, 1988.

[85] S. G. Tikhodeev, A. L. Yablonskii, E. A. Muljarov, N. A. Gippius, and T. Ishihara, "Qausiguided modes and optical properties of photonic crystal slabs," *Phys. Rev. B*, vol. 66, p. 045102, 2002.

[86] E. Jaynes and F. Cummings, "Comparison of quantum and semiclassical radiation theory with application to the beam maser," *Proc. IEEE*, vol. 51, p. 89, 1963.

[87] E. d. Valle, F. P. Laussy, and C. Tejedor, "Luminescence spectra of quantum dots in microcavities: II. Fermions," *Phys. Rev. B*, vol. 79, p. 235326, 2009.

[88] F. P. Laussy, M. M. Glazov, A. Kavokin, D. M. Whittaker, and G. Malpuech, "Statistics of excitons in quantum dots and their effect on the optical emission spectra of microcavities," *Phys. Rev. B*, vol. 73, p. 115343, 2006.

[89] I. Aben, W. Ubachs, G. V. D. Zwan, and W. Hogervorst, "Polarization effects in resonant four-wave-mixing processes," *Mol. Phys.*, vol. 76, p. 591, 1992.

[90] Q. Lin and G. P. Agrawal, "Vector theory of four-wave mixing: polarization effects in fiber-obtic parametric amplifiers," *J. Opt. Soc. Am. B*, vol. 21, p. 1216, 2004.

[91] W. Langbein and B. Patton, "Heterodyne spectral interferometry for multidimensional nonlinear spectroscopy of individual quantum systems," *Opt. Lett.*, vol. 31, p. 1151, 2006.

[92] M. Tavis and F. W. Cummings, "Exact solution for an n-molecule-radiation-field Hamiltonian," *Phys. Rev.*, vol. 170, p. 379, 1968.

[93] F. Albert, K. Sivalertporn, J. Kasprzak, M. Strauß, C. Schneider, S. Höfling, M. Kamp, A. Forchel, S. Reitzenstein, E. A. Muljarov, and W. Langbein, "Microcavity controlled coupling of excitonic qubits," *Nat. Commun.*, vol. 4, p. 1, 2013.

[94] F. Albert, K. Sivalertporn, J. Kasprzak, M. Strauß, C. Schneider, S. Höfling, M. Kamp, A. Forchel, S. Reitzenstein, E. A. Muljarov, and W. Langbein, "Coherence dynamics and quantum-to-classical crossover in an exciton-cavity system in the quantum strong coupling regime," *New J. Phys.*, vol. 15, p. 045013, 2013.

[95] R. Pässler, E. Griebl, H. Riepl, G. Lautner, S. Bauer, H. Preis, W. Gebhardt, B. Buda, D. J. As, D. Schikora, K. Lischka, K. Papagelis, and S. Ves, "Temperature dependence of exciton peak energies in ZnS, ZnSe, and ZnTe epitaxial films," *J. Appl. Phys.*, vol. 86, p. 4403, 1999.

[96] J. Kasprzak, B. Patton, V. Savona, and W. Langbein, "Coherent coupling between distant excitons revealed by two-dimensional nonlinear hyperspectral imaging," *Nature Photonics*, vol. 5, p. 123, 2011.